THE NATURE OF THE CRYSTAL STRUCTURES OF

SOME SULFIDE MINERALS WITH

SUBSTRUCTURES

by

Bernhardt John Wuensch

S. B., Massachusetts Institute of Technology (1955)

S. M., Massachusetts Institute of Technology (1957)

Submitted in partial fulfillment of the

requirements for the Degree of

Doctor of Philosophy

at the

Massachusetts Institute of Technology

June, 1963

Signature of Author_

Department of Geology and Geophysics,

May 10, 1963

Certified by_ _
Thesis Supervisor

Accepted by_ _
Chairman, Departmental Committee
on Graduate Students

Abstract

The Nature of the Crystal Structures of Some

Sulfide Minerals with Substructures

by

Bernhardt John Wuensch

Submitted to the Department of Geology and Geophysics on
May 10, 1963, in partial fulfillment of the requirements for the degree
of Doctor of Philosophy.

The crystallography of three transition metal sulfide minerals
has been investigated with x-ray diffraction methods. The crystal
structure of tetrahedrite, $Cu_{12}Sb_4S_{13}$, proposed in 1934 by Pauling and
Neuman, has been confirmed. Least-squares refinement reduced the
initial disagreement factor from 27.9 percent to a value of 6.7 percent.
The final weighted rms disagreement factor was 3.5 percent. The
structure contains Sb atoms which form nearly orthogonal bonds with
three S atoms. There are two types of Cu atoms. Cu(1) is bonded to
three S atoms in a planar configuration. Such coordination for a
transition metal appears to be unique to copper sulfides. Cu(2) is in
slightly distorted tetrahedral coordination. The thermal motion of the
atoms is essentially isotropic with the exception of the Cu atom in
triangular coordination. This atom has a large component of thermal
vibration normal to the plane of the group.

Above 110° C chalcocite, Cu_2S, is hexagonal. The structure was
solved with the aid of implication diagrams and partial Fourier syntheses.
S atoms are in hexagonal close-packing. The Cu atoms are disordered.
Sites of high Cu electron density occur in 2-fold coordination between
S atoms in neighboring layers, in 3-fold coordination in the S layers,
and in 4-fold coordination in all tetrahedral interstices. Use of the Cu
distribution indicated by the electron density syntheses yielded a dis-
agreement factor of 18.0 percent. The structure bears a close relation
to stromeyerite, CuAgS. The low-chalcocite substructure has Cu atoms
in only 3-fold and 4-fold coordination. The structure of covellite, CuS,
may be derived from the low-chalcocite substructure through a different
stacking sequence of low-chalcocite unit cells and by omitting the Cu
atoms in one set of tetrahedral interstices.

Pyrrhotite of composition $Fe_{.889}S$ is pseudohexagonal. Pre-
cession photographs suggest a superstructure with cell dimensions
which appear to be two and four times the $\underline{A}$ and $\underline{C}$ dimensions of a
NiAs-type substructure. Small displacements of the superstructure
reflections in the patterns indicate the presence of twinning. A pre-
viously proposed twin law explains neither the symmetry of the twin

nor the non-space group absences in the observed reflections. It is
shown that the true lattice is at least dimensionally monoclinic and
is twinned by a 2-fold rotation about [110]. The $\underline{a}$ and $\underline{b}$ translations
are twice the orthohexagonal $\underline{B}$ and $\underline{A}$ dimensions of the substructure,
respectively, and β is $91.79°$. The $\underline{c}$ translation and lattice type
remain uncertain. Patterson projections based on data obtained from
a twinned crystal suggest that there is considerable distortion of the
structure about the Fe vacancies in the NiAs-type arrangement.

A direct procedure, suitable for application to high-speed
computation, is described for the determination of x-ray absorption
corrections for the precession, equi-inclination Weissenberg and
Eulerian cradle diffraction geometries. The crystal is subdivided
into volume elements represented by an orthogonal grid. Unit vectors
are established relative to the coordinate system of the crystal, which
specify the directions of the incident and diffracted beams for each
reflection. Distances from each grid point to the surface of the crystal
are determined and summed to evaluate a transmission factor. The
method is applicable to a crystal of arbitrary shape. Re-entrant angles
are permitted. The only restriction on the shape of the crystal is that
it be representable as a combination of one or more functions which
may be expressed analytically.

Thesis supervisor: Martin J. Buerger
Title: Institute Professor

Acknowledgements

Table of Contents

List of Figures

(Page numbers refer to the figure captions. The captions
are given on the page immediately preceding the figure itself.)

List of Tables

I Preface

One of the main concerns of crystal chemistry is an understanding of the factors governing the formation of particular crystal structures. Ultimately, one would hope to be able to predict the particular structure assumed when any arbitrary collection of atoms is allowed to crystallize.

It seems doubtful whether this objective may ever be realized to its fullest degree. In certain special cases, however, great progress has been made.

(1) <u>Organic compounds</u>. Chemistry is often able to predict a probable molecular configuration, and Kitaigorodskii (1961) has proposed rules governing the packing of these molecules.

(2) <u>Ionic solids</u>. The cohesive forces between ions may be considered an electrostatic attraction between point charges. Geometrical considerations determine nearest neighbor coordination of the ions. Pauling (1960) has given general principles governing secondary coordination which often can successfully predict the general nature - if not the detailed arrangement - of the structure.

(3) <u>Metallic phases</u>. While no unified view of intermetallic phases can yet be given, the particular structures to be expected may be predicted for a great many systems. Thus "normal valence compounds", "electron compounds", "Laves phases", "Zintl phases", "beta-tungsten phases", etc., all have characteristic structures whose occurrence may be predicted with a fair degree of certainty in systems in which certain special conditions apply (Taylor, 1961).

Prediction of the more complex structures provided by nature becomes an almost impossible task when approached solely from a theoretical point of view. To accomplish this, one would often require

a detailed picture of the manner in which the electronic states of an atom are perturbed by any sort of neighboring atom. Understanding of the raison d'être of most crystal structures has evolved from experimental determination of a large number of similar structures. The recent progress in the methods of crystal-structure analysis, and the advent of high-speed electronic computers, has facilitated the determination of complex crystal structures and their refinement to a high degree of precision. This permits detailed interpretation of the bonding in the structure and often clues to the reasons for the particular structure being assumed. As a large number of such observations are built up, one ultimately hopes to establish some unifying principle for a larger group of structures of a particular sort.

With this background in mind, the writer became interested in the crystal chemistry of the group VI elements S, Se and Te. The crystal structures of compounds containing S, in particular, are interesting in that the atom has only a moderate electronegativity (2.5, as compared to 3.5 for O, 3.0 for Cl and 4.0 for F) and, furthermore, is easily polarized. Sulfide structures therefore exhibit a complete spectrum of bond types depending upon the particular element with which S combines (Wells, 1962). Ionic structures are formed with the most electropositive elements, such as the alkali metals, the alkaline earths and some transition metals. On the other hand, the high polarizability of the sulfur atoms leads a large number of other structures to be predominantly covalent in character. The ring structure of elemental sulfur, the electron-pair bonds in sphalerite, the sulfur pairs in pyrite and marcasite, and the chains and rings found in many sulfides are evidences of this property. Still other sulfides, notably those of the transition metal ions, behave as alloys, and must be regarded as intermetallic compounds. In the system Co-S, for example, phases of composition Co_9S_8, CoS, Co_3S_4 and CoS_2 occur.

It is with transition metal sulfides that this thesis is concerned. These compounds generally have very simple formulae. Their crystal

structures, however, are usually complex. Their phase diagrams frequently are also complex and incompletely understood. These sulfides also present many crystallographic challenges:

(1) Their structures are often based on close packing of sulfur atoms, with the metal atoms occupying interstices. Many structures therefore display substructures and pseudo-symmetry, which complicates their solution.

(2) Phase transformations, often of an order-disorder type, are common. These transformations occur at relatively low temperatures (90°- $350^{\circ}C$) so that these compounds are usually formed above their transformation temperatures. This situation, coupled with pseudosymmetry, causes twinning to be common. Many sulfides are invariably twinned and the twin laws are frequently complex.

(3) Many sulfides exsolve a second phase upon cooling. Since both phases usually are based on close-packed sulfur atoms, the result is usually an oriented intergrowth with some plane of close-packed sulfur atoms in common. These intergrowths make identification of the composition or structure of the phases difficult.

(4) Since these sulfides are intermetallic in nature, their composition may vary over wide ranges. Furthermore, possibility of solid solution will be determined by the bonding properties of the solute atom rather than atomic size or valence as in ionic compounds. A wide variety of atoms may therefore be substituted in these structures, and their exact formulae are often unknown. Frequently this information may be obtained only through a determination of the crystal structure.

As a result of these difficulties, the sulfides are the least understood of any major mineral group. The crystallography of many minerals is uncertain and unusual compositions have been reported which remain to be verified.

Three sulfide minerals have been studied in this thesis: tetrahedrite ($Cu_{12}Sb_4S_{13}$), chalcocite (Cu_2S), and pyrrhotite ($Fe_{1-x}S$). These structures bear no close relation to one another other than the fact that they are all sulfide minerals containing transition metal ions, and are also derivative structures containing close-packed sulfur atoms, and therefore display marked substructures. The results of these investigations are reported in Sections II, III and IV. With minor modifications, it is planned to submit each for publication as a separate article.

Most sulfide minerals have high absorption coefficients for x-rays. Furthermore, many are sectile and cannot be ground into the simple shapes for which absorption corrections for the diffracted intensity data are readily available. At present a program for determining absorption corrections exists only for the equi-inclination diffraction geometry. This program is also restricted to crystals bounded only by plane faces which form no re-entrant angles. The lack of a sufficiently general absorption correction program represents the only missing step in the series of computations required for the complete determination and refinement of a crystal structure. Section V develops a procedure, suitable for application to high-speed computation, for the determination of absorption corrections in the three principal diffraction geometries. There are no restrictions on the crystal shape other than that it be representable by a series of bounding functions which may be expressed analytically. The procedure is being programmed for the I.B.M. 7090 computer and, in fact, special versions have been employed in studying the structures described in the preceding sections of this thesis. The necessary programming, however, was done in collaboration with Dr. Charles T. Prewitt and therefore is not described as a portion of this thesis. Section V is also intended for publication as an article.

With the application of an accurate absorption correction, a set of structure factors should be obtainable which has a high degree of

overall precision. Few assessments have been made of the magnitude of the random and systematic error present in counter diffractometer data. Tetrahedrite presented an unusual opportunity to investigate these effects since the structure is isometric. Comparison of those diffracted intensities which were required by symmetry to be equivalent permitted an estimation of these errors. The results are given in Appendix I, which is intended for publication as a Note.

The remaining Appendices are not intended for publication. These describe devices and procedures not previously used in this laboratory, such as the small furnace designed for the precession camera, and use of film techniques in connection with the new Charles Supper Company integrating precession camera. It is hoped that these sections may prove useful to future members of the laboratory who may desire to use these techniques.

References

Kitaigorodskii, A.I. (1961). Organic Chemical Crystallography. (English translation, Consultants Bureau, New York) 541 pp.

Pauling, Linus (1960). The Nature of the Chemical Bond. (Cornell University Press, Ithaca, New York, Third Edition) 644 pp.

Taylor, A. (1961). X-Ray Metallography. (J. Wiley and Sons, New York, First Edition) 993 pp.

Wells, A.F. (1962). Structural Inorganic Chemistry. (Clarendon Press, Oxford, Third Edition) 1055 pp.

Section II

The Crystal Structure of Tetrahedrite, $Cu_{12}Sb_4S_{13}$.

2.1 Introduction

The tetrahedrite minerals are a commonly-occurring family of sulfosalts with general composition $X_{12}Y_4S_{13}$. As is the case with most sulfosalts, considerable substitution can occur for the metal atoms $\underline{X}$ and $\underline{Y}$. A complete series of compositions occurs between tetrahedrite ($\underline{Y}$ = Sb) and tennantite ($\underline{Y}$ = As). Fairly large amounts of Bi may also substitute for $\underline{Y}$. The metal atoms occupying $\underline{X}$ are principally Cu. More commonly than not, however, Zn, Fe, Ag, Hg, Pb, Ni or Co substitute for Cu, in amounts up to 20 %. The number of S atoms may also vary slightly. At least twenty-five different mineral names have been assigned to these compositions (Palache $\underline{et\,al.}$, 1944).

As has often been the case with sulfosalts having complicated compositions, the true nature of the chemical formula became certain only after the crystal-structure of the mineral had been investigated (Pauling and Neuman, 1934). The proposed structure, however, has several curious features and was determined at a time when many of the methods of modern crystallography had yet to be developed. The Pauling and Neuman structure determination, for reasons described in the following section, therefore merited reinvestigation. This section describes refinement of the crystal structure of tetrahedrite. The Pauling and Neuman structure has been shown to be correct, although the parameters determined in present work represent an arrangement of atoms which is more distorted than had previously been supposed. Examination of the more precise interatomic distances and angles has provided clues to the reasons for the formation of the structure.

2.2 The Status of Tetrahedrite

The general nature of the tetrahedrite structure was determined by Machatschki (1928a, 1928b). The ideal structure, however, was assumed to correspond to a formula Cu_3SbS_3. While the presence of sulfur in slight excess of this composition was noted, it was assumed that this was due to solid solution. Pauling and Neuman (1934) reappraised the reliable analyses of tetrahedrite, and concluded that a formula $Cu_{12}Sb_4S_{13}$ was in closer accord with the analyses. (The ratio S/Sb = 26/8 = 3.25 is the next highest ratio above 3/1 which is permitted by the space group of tetrahedrite.)

The structure proposed by Pauling and Neuman is a derivative of the sphalerite structure. The arrangement may be described by considering a cubic unit of sphalerite containing eight unit cells. Let t he origin be chosen at a tetrahedral site not occupied by Zn. S atoms then lie in tetrahedral coordination about the origin at $\frac{1}{4}\frac{\bar{1}}{4}\frac{1}{4}$, $\frac{\bar{1}}{4}\frac{1}{4}\frac{1}{4}$, $\frac{1}{4}\frac{1}{4}\frac{\bar{1}}{4}$, and $\frac{\bar{1}}{4}\frac{\bar{1}}{4}\frac{\bar{1}}{4}$ (or $\frac{1}{8}\frac{1}{8}\frac{1}{8}$, etc., in the supercell). Let three of these S atoms be removed, and the remaining atom be displaced to $\bar{0}00$. A similar operation is performed at 111 (or $\frac{1}{2}\frac{1}{2}\frac{1}{2}$ in the supercell) so that the final supercell is body centered. The Sb or As atom is substituted for the Zn atom at $\frac{1}{2}\frac{\bar{1}}{2}\frac{1}{2}$ ($\frac{1}{4}\frac{\bar{1}}{4}\frac{1}{4}$ in the supercell) which would have been coordinated with a missing S atom.

Several features of the structure determination suggested that the Pauling and Neuman structure might possibly be incorrect, or, at any rate, require major parameter adjustments upon refinement:

(1) The structure was guessed from a large number of possible arrangements permitted by the probable tetrahedrite space group.

(2) No electron density maps were prepared.

(3) The final atomic parameters were determined by trial and error adjustments.

(4) The structure was determined from only 18 intensities, of which 7 were not detectable. Furthermore, all were zero level reflections, so that the structure was essentially solved in projection.

(5) The curious arrangement of copper in 6-fold coordination
about sulfur and the ordering of the As atoms will be primarily reflected
in the weak superstructure intensities. Two-thirds of the superstructure
reflections investigated by Pauling and Neuman were not detectable!

2.3 Selection of Material

The specimen of tetrahedrite employed by Pauling and Neuman
was a variety known as binnite. This mineral is an intermediate member
of the tetrahedrite-tennantite series but, as with most members of the
family, is closer to the tennanite end of the series. The difference in
scattering power between As ($\underline{Z}$ = 33) and Cu ($\underline{Z}$ = 29) is only 4 electrons.
This slight difference in atomic number would result in relatively small
contribution to the superstructure intensities. In confirming the ordered
substitution of As or Sb in Cu positions of the sphalerite structure, it
is desirable for this arrangement to have an optimum effect on the
superstructure intensities. The situation is much more favorable
near the tetrahedrite end of the series, since the difference in scattering
power between Sb ($\underline{Z}$ = 51) and Cu is 22 electrons. By the same token,
if a careful refinement of the structure is to be accomplished, the ratio
of Sb to As should be precisely known because of the large difference
in scattering power of these elements (18 electrons.) It would also
be desirable to employ a crystal in which $\underline{X}$ was almost entirely copper.
The effect of this type of substitution on a structure determination is
less serious, however, since it occurs only to a limited degree, and
usually involves atoms with scattering powers differing from copper by
only one or two electrons.

Tetrahedrite from Horhausen, Westerwald, Germany, was
selected for this study. Analyses of this material have been given by
Prior and Spencer (1899) and Kretschmer (1911). These results are
given in Table 2.1. The composition of these crystals is very unusual
in that $\underline{Y}$ is almost entirely Sb, and $\underline{X}$ almost entirely Cu. Specimens

Table 2.1

Chemical Analyses of Horhausen Tetrahedrite

Weight Percent

	Prior and Spencer (1899)	Kretschmer (1911)	Ideal $Cu_{12}Sb_4S_{13}$
Cu	41.55	37.75	45.77
Zn	2.63	6.51	-
Fe	1.02	1.10	-
Pb	.62	.71	-
Ag	-	.11	-
Sb	28.32	28.66	29.22
Bi	.83	.53	-
S	24.33	24.61	25.01
Σ	99.30	99.98	100.00
Density (g/cm^3)	4.969	5.079	$\approx$4.99

suitable for x-ray analysis were obtained from a tetrahedral crystal[1] with excellently developed forms, and a shiny metallic luster. Preliminary x-ray examination showed that many fragments displayed lineage structure. Eventually a fragment free from this effect was obtained. This specimen was ground into several spheres using a method similar to that described by Bond (1951). The crystal selected for final study and for the subsequent collection of intensities had a radius of 0.114 mm and was spherical to within ± 1.7 %. ($\mu_1 r = 7.39$ for Cu$\underline{K}\alpha$ radiation[2]).

2.4 X-ray Examination and Unit-cell Contents

The spherical specimen described above was examined with Mo$\underline{K}\alpha$ radiation using the precession method. A zero-level photograph is reproduced in Fig. 2.1$\underline{a}$. This pattern clearly indicates the presence of the marked sphalerite-like substructure reflections. The superstructure reflections require that $\underline{a}$ be equal to twice the cell dimensions of the sphalerite substructure. Figure 2.1$\underline{b}$ presents a first-level photograph which displays only the relatively weak superstructure reflections.

The patterns displayed symmetry $\underline{m}3\underline{m}$. This symmetry was confirmed with cone-axis photographs taken about each of the three cubic axes. The only systematic obsence of reflections which was observed was for reflections with $\underline{h} + \underline{k} + \underline{l} \neq 2\underline{n}$. This requires that the lattice be body-centered. (The relative intensity of the substructure reflections indicated that the substructure was face-centered.) The diffraction symbol for tetrahedrite is therefore $\underline{m}3\underline{m}I - - -$. This permits I$\underline{m}3\underline{m}$, I43, and I$\bar{4}3\underline{m}$ as possible space groups. The tetrahedron is the most common form displayed by tetrahedrite (and is the

---

[1] Harvard Catalogue Number 82560

[2] The value used for μ_1 is an average of the two values which were obtained by using the exact compositions reported by Kretschmer, and Prior and Spencer.

Figure 2.1

Precession photographs of tetrahedrite, a_2^* horizontal, a_3^* vertical, MoKα radiation.

     a. (above) zero-level, $\bar{\mu} = 25°$, 46 hour exposure.

     b. (below) first-level, $\bar{\mu} = 20°$, 72 hour exposure.
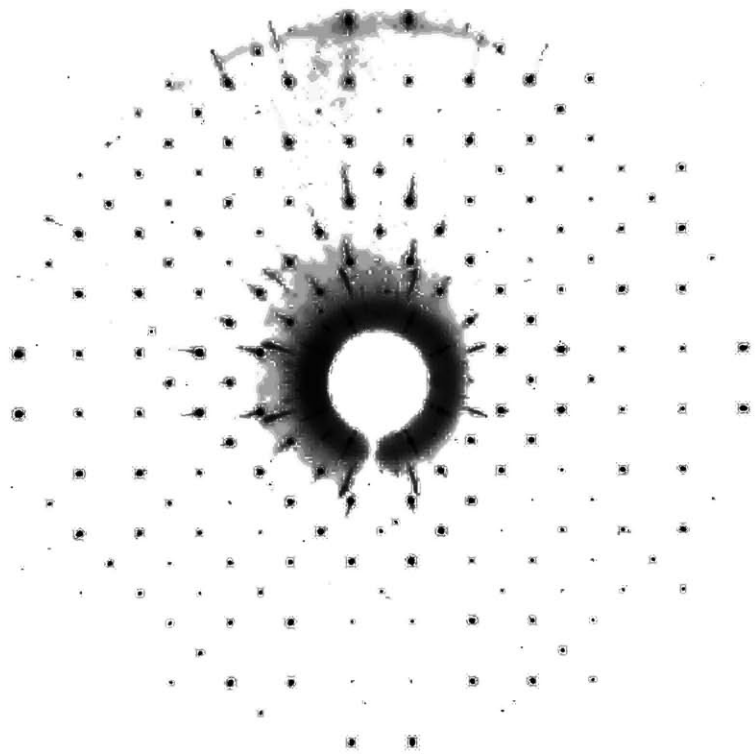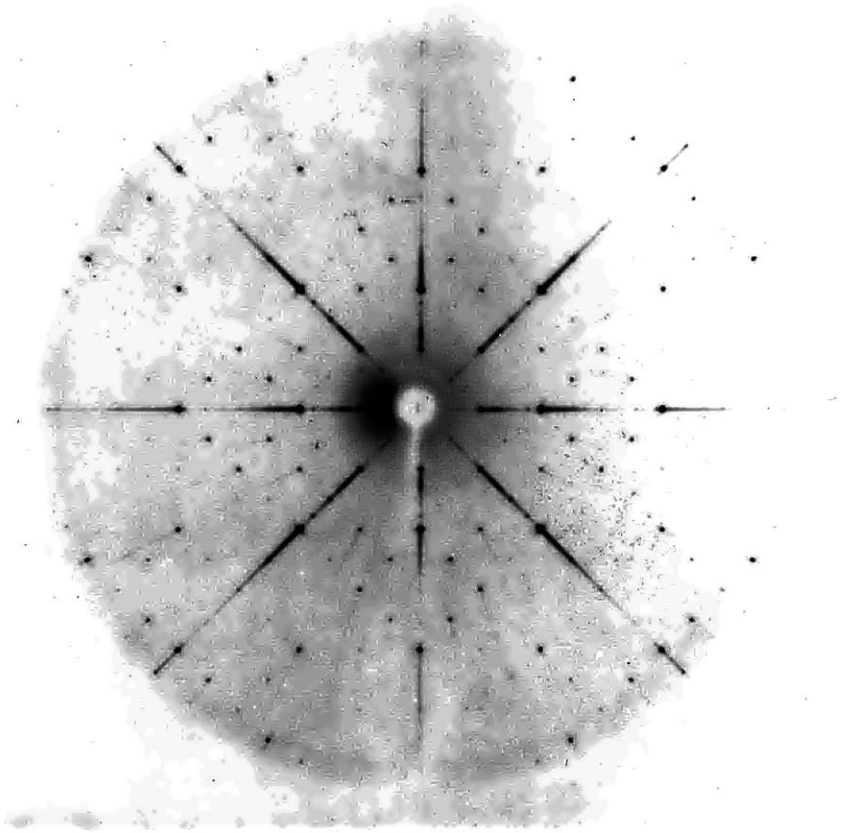
feature from which the name of the mineral is derived). The morphology of the crystal thus requires $I\bar{4}3m$ as the correct space group. This result is in accord with previous investigations.

Final unit cell dimensions were obtained from precision back-reflection Weissenberg photographs, using $CuK\alpha$ radiation (Buerger, 1942). The extrapolated value for $\underline{a}$ was determined with the aid of the least-squares program LCLSQ, written for the IBM 7090 computer by C. W. Burnham (1961), and was found to be $10.3908 \pm .0006$ Å. Using the analyses and densities listed in Table 2.1, the unit-cell contents were found to be

$$2 \left| \begin{array}{l} Cu_{10.59} \\ Zn_{0.67} \\ Fe_{0.31} \\ Pb_{0.05} \\ \hline 11.59 \end{array} \right. \quad \left| \begin{array}{l} Sb_{3.94} \\ Bi_{0.07} \\ \hline 4.01 \end{array} \right. \quad S_{12.83}$$

$$2 \left| \begin{array}{l} Cu_{10.19} \\ Zn_{1.17} \\ Fe_{0.34} \\ Pb_{0.06} \\ \hline 12.32 \end{array} \right. \quad \left| \begin{array}{l} Sb_{4.04} \\ Bi_{0.04} \\ \hline 4.08 \end{array} \right. \quad S_{13.17}$$

using the Prior and Spencer and Kretschmer analyses, respectively. These results neatly bracket the ideal composition $Cu_{12}Sb_4S_{13}$.

2.5 Collection of Intensities

An equi-inclination counter diffractometer was used to record the intensities. A Kr-filled proportional counter was used as a detector. The associated electronics were standard Norelco equipment and

included pulse height analysis circuitry. Care was taken to align the
diffractometer so that the incident beam exhibited constant intensity
over a distance exceeding the diameter of the spherical crystal. The
beam profile was determined with the aid of a lead plate in which a fine
hole had been drilled. With the counter in position to receive the direct
beam, this plate was mounted in a standard goniometer head and placed
before the counter. The spindle translation, which is normally used
to center the crystal, and one of the goniometer arc translating screws
were then used to scan the beam in horizontal and vertical directions,
respectively. The instrument, when in final adjustment, displayed
intensity constant to within ± 2% over a region of .71 mm, or three
times the diameter of the crystal.

Since tetrahedrite has Laue symmetry $\frac{4}{m}\,3\,\frac{2}{m}$, the independent
reflections are contained within $\frac{1}{48}$ of reciprocal space ($i.e.\ h \geq k \geq l$).
Values for the instrumental settings ϕ and Υ were computed for these
reflections with the IBM 7090 program DFSET (Prewitt, 1960). Integrated
intensities were determined by recording the background intensity at
3 degrees ϕ from the diffraction peak, the total number of counts as
the crystal was rotated through 6 degrees ϕ, and, again recording
background intensity at 3 degrees ϕ on the other side of the diffraction
peak. Assuming that the background varies linearly between the two
ϕ positions at which background was recorded, the integrated intensity
I is given by

$$I = E - \left(\frac{B}{t_B} + \frac{B'}{t'_B}\right)\frac{t_E}{2}$$

where E is the number of counts accumulated as the crystal is rotated
through the position for which diffraction occurs, t_E is the time during
which these counts are accumulated , B is the number of background
counts accumulated in time t_B at the first position of the crystal for
which background intensity is determined, and B' and t'_B are the cor-
responding quantities for the second position of the crystal. High

counting rates were encountered with some of the substructure reflections. In these instances absorbing foils were inserted before the counter so that the linearity range of the detector would not be exceeded. The maximum peak height recorded was limited to 2000 counts per second in this fashion. The data was corrected for Lorentz and polarization factors, and appropriate spherical absorption factors (Bond, 1959) with the aid of the IBM 7090 data reduction programs DTRDA and DTRDB (Burnham, 1961).

Of 154 independent reflections contained within the $CuK\alpha$ sphere, 137 were accessible with the instrument used. Of these, 2 were undetectable and were assigned values equal to $\underline{E}_{min} - \underline{B}$ (Burnham, 1961). Sixteen of the reflections recorded were substructure reflections. Appendix I describes reproducibility checks which were performed on a representative collection of equivalent reflections. These results indicate that the overall reliability of the set of structure factors which was obtained was about 3 %.

2.6 Refinement of the Structure

The structure proposed by Pauling and Neuman contains five atoms per asymmetric unit. The parameters reported for these atoms[1] are given in Table 2.2. Structure factor calculations were performed for this model using the full-matrix least-squares program SFLSQ3 (Prewitt, 1962). The disagreement factor, $R = \Sigma | |F_o| - |F_c| | / \Sigma |F_o|$, for these parameters was 27.9% for the complete three-dimensional collection of structure factors, and 26.1% for the zero-level reflections

---

[1] It should be noted that Pauling and Neuman determined the structure of a mineral which was essentially tennantite, while the present study is concerned with tetrahedrite. Using Machatschki's work, however, Pauling and Neuman also proposed parameters for tetrahedrite. These parameters, which are given in Table 2.2, were considered highly reliable.

Table 2.2

Positional Parameters and Isotropic Temperature factors for Tetrahedrite

Atom	Equipoint	Parameter	Pauling and Neuman (1934)	distortion from sphalerite arrangement	Present study[1]	distortion from sphalerite arrangement
Cu 1	$12d\bar{4}$	x	$\frac{1}{4}$	0	$\frac{1}{4}$	0
	$\frac{1}{4}\frac{1}{2}0$	y	$\frac{1}{2}$	0	$\frac{1}{2}$	0
		z	0	0	0	0
		B	1.0	-	1.300	-
Cu 2	12e m m	x	.225	-.025	.212(7)±.0008	-.037
	x00	y	0	0	0	0
		z	0	0	0	0
		B	1.0	-	3.808	-
S 1	24 g m	x	.122	-.003	.115(3)±.0007	-.010
	xxz	y	.122	-.003	.115(3)±.0007	-.010
		z	.363	-.012	.360(3)±.0009	-.015
		B	1.0	-	.697	-

[1] See footnote 2 on next page

Table 2.2 (continued)

Positional Parameters and Isotropic Temperature factors for Tetrahedrite

Atom	Equipoint	Parameter	Pauling and Neuman (1934)		Present study[2]	
				distor. from sphal. arr.		distor. from sphal. arr.
S 2	$2a\bar{4}3m$	x	0	-	0	-
	000	y	0	-	0	-
		z	0	-	0	-
		B	1.0	-	1.576	-
Sb	8c3m	x	.278	+.028	.2682±.0002	+.0182
	xxx	y	.278	+.028	.2682±.0002	+.0182
		z	.278	+.028	.2682±.0002	+.0182
		B	1.0	-	.674	-
$R = \Sigma \mid \mid F_o \mid - \mid F_c \mid \mid / \Sigma \mid F_o \mid$			27.9 %[1]		9.0 %[2]	
Weighted $R = \dfrac{\Sigma w(\mid F_o \mid - \mid F_c \mid)^2}{\Sigma w F_o^2}^{\frac{1}{2}}$			-		6.5 %[2]	

[1] R = 26.1% for the zero reflections measured by Pauling and Neuman.

[2] R decreased to 6.7% when anisotropic temperature factors were employed. The positional parameters remained unchanged, although their estimated standard deviations decreased. The standard deviations listed here are those for the final parameters.

corresponding to those measured by Pauling and Neuman.

This relatively low value for $\underline{R}$ indicated that the structure was probably correct and that refinement of the Pauling and Neuman structure would probably improve the agreement between F_{obs} and F_{cal}.

The refinement was carried out in four stages. The difference between the stages was the type of weighting scheme used. In each stage scale factor[1] and atomic positions were refined until the parameters had converged. Then atomic temperature factors were refined until they had converged. Refinement of scale factor and atomic positions was then repeated, and so on, until no further variation of parameters occurred.

The results of a least-squares refinement depend strongly on the weighting scheme applied to the data. At present no well-established weighting scheme exists for counter-diffractometer data. The weighting scheme adopted for this work is an extension of ideas first presented by Cruickshank et al. (1961). Following each stage of refinement, the value of $\underline{R}$ was computed as a function of F_{obs}. The weighting scheme adopted was one for which the product of weight times $\underline{R}$ remained constant for all values of F_{obs}.

The course of the refinement procedure is given in Table 2.3. (The number of cycles of refinement listed in column three of this table refers to the number of cycles required to attain convergence, and not the number of cycles actually performed.) During stage 1, in which equal weights were applied to all reflections, $\underline{R}$ was reduced from 28.9% to 10.4%. The variation of $\underline{R}$ with F_{obs} at this point suggested the weighting scheme listed in Table 2.3 for stage 2. This stage reduced $\underline{R}$ to 9.3% and the weighted rms $\underline{R}$ to 7.8%. Further

---

[1] Only one scale factor was used. The study of the reliability of the structure factors, described in Appendix I, indicated that there was no systematic variation of structure factors from level to level. Introduction of separate scale factors for each level was therefore considered unjustified.

Table 2.3

Stages in the Refinement of the Crystal Structure of Tetrahedrite

Stage	Weighting scheme	Parameters varied	R	Weighted R
		Parameters of Pauling and Neuman structure, all isotropic B's arbitrarily set equal to 0.7	28.9	27.1
1	Equal weights	Scale factor and positions, 4 cycles	17.1	15.2
		Isotropic temperature factors 3 cycles	11.4	10.8
		Scale factors and positions 1 cycle	10.4	9.7
2	$F_o > 70$ $w = 1$ $F_o < 70$ $w = \dfrac{13.6}{54.4-.593\,F_o}$	Scale factor and positions 1 cycle	10.5	8.9
		Isotropic temperature factors 1 cycle	9.8	8.3
		Scale factor and positions 1 cycle	9.3	7.8
3	$F_o > 225$ $w = 1$ $225 > F_o > 160$ $w = \dfrac{6}{36-.125\,F_o}$ $160 > F_o > 110$ $w = \dfrac{6}{.16\,F_o-11.6}$ $110 > F_o > 75$ $w = 1$ $75 > F_o > 0$ $w = \dfrac{6}{80-F_o}$	Isotropic temperature factors 2 cycles	9.1	6.7
		Scale factor and positions 1 cycle	9.0	6.5
		Isotropic temperature factors 1 cycle	9.0	6.5
		Anisotropic temperature factors 2 cycles	6.8	5.3

Table 2.3 (continued)

Stages in the Refinement of the Crystal Structure of Tetrahedrite

Stage	Weighting scheme	Paremeters varied	R	Weighted R
4	$F_o > 256$ $w = 1$	Scale factor and positions 2 cycles	6.7	3.5
	$256 > F_o > 151$ $w = \dfrac{1.5}{24.2 - .088\,F_o}$	Anisotropic temperature factors 1 cycle	6.7	3.5
	$151 > F_o > 52$ $w = \dfrac{1.5}{4.9 + .003(106 - F_o)^2}$	Scale factor and positions 1 cycle	6.7	3.5
	$52 > F_o > 0$ $w = \dfrac{1.5}{52 - .72\,F_o}$			

modification of the weighting scheme and the refinement of stage 3 reduced $\underline{R}$ by only 0.3%. Parameters at this stage of refinement are listed in Table 2.2. As the final step in stage 3, anisotropic temperature factors were employed. $\underline{R}$ decreased to 6.8%, and the weighted $\underline{R}$ to 5.3%. A final modification of the weighting scheme was made for stage 4. Further refinement left $\underline{R}$ and all parameters essentially unchanged, although the weighted $\underline{R}$ decreased to 3.5%.

The final values for the anisotropic temperature factor coefficients are presented in Table 2.4. The final value for $\underline{R}$ with these parameters was 6.7% and, for the weighted rms $\underline{R}$, 3.5%. The positional parameters at this level of agreement remained unchanged from those given in Table 2.2. The values of the "equivalent" isotropic temperature factor which corresponds to each anisotropic temperature factor coefficient was computed according to the relation

$$B = \frac{4}{3} \pi \sum_i \sum_j \beta_{i_j} (\underset{\sim}{a}_i \cdot \underset{\sim}{a}_j)$$

(Hamilton, 1959). This relation provides the isotropic temperature factor which corresponds to the same mean square thermal displacement as that predicted by the anisotropic coefficients. The values obtained are also listed in Table 2.4 and are in excellent agreement with the isotropic temperature factors listed in Table 2.2. Observed and calculated structure factors are compared in Table 2.5.

2.7 Discussion of the Structure

Table 2.2, in which the parameters of the Pauling and Neuman structure are compared with the present study, also lists the displacement of the atoms from the positions of an ideal sphalerite-like arrangement. It may be seen that appreciable displacements exist. The present structure differs from that of Pauling and Neuman in that the Sb atom is less displaced than had been proposed, while the Cu(2) and S(1) atoms have undergone greater displacements. The positional

Table 2.4

Anisotropic Temperature-factor Coefficients for Tetrahedrite

Atom	Symmetry restrictions	Independent values of β_{i_j}	Equivalent isotropic temperature factor
Cu 1	$\beta_{22} = \beta_{33}$ $\beta_{12} = \beta_{23} = \beta_{31} = 0$	$\beta_{11} = .0033 \pm .0008$ $\beta_{22} = .0030 \pm .0008$	1.345
Cu 2	$\beta_{22} = \beta_{33}$ $\beta_{12} = \beta_{13} = 0$	$\beta_{11} = .0028 \pm .0010$ $\beta_{22} = .0126 \pm .0007$ $\beta_{23} = -.0048 \pm .0013$	4.022
S 1	$\beta_{11} = \beta_{22}$ $\beta_{31} = \beta_{23}$	$\beta_{11} = .0016 \pm .0005$ $\beta_{33} = .0017 \pm .0009$ $\beta_{12} = .0000(3) \pm .0008$ $\beta_{31} = .0001 \pm .0005$	0.700
S 2	$\beta_{11} = \beta_{22} = \beta_{33}$ $\beta_{12} = \beta_{23} = \beta_{31} = 0$	$\beta_{11} = .0030 \pm .0013$	1.276
Sb	$\beta_{11} = \beta_{22} = \beta_{33}$ $\beta_{12} = \beta_{23} = \beta_{31}$	$\beta_{11} = .0018 \pm .0001$ $\beta_{12} = -.0001 \pm .0002$	0.770

Table 2.5

Comparison of Observed and Calculated Structure Factors

for Tetrahedrite (R = 6.7%)

h	k	l	F_{obs}	F_{cal}	h	k	l	F_{obs}	F_{cal}
2	0	0	157.2	116.2	2	1	1	62.8	61.1
4	0	0	530.9	541.1	4	1	1	197.7	173.2
6	0	0	62.4	45.7	6	1	1	252.0	248.5
8	0	0	519.2	515.6	8	1	1	131.4	141.4
10	0	0	54.4	46.0	10	1	1	140.5	144.2
12	0	0	40.1	37.5	12	1	1	172.3	188.3
1	1	0	47.6	34.1	3	2	1	129.8	107.4
3	1	0	48.6	20.6	5	2	1	165.3	163.6
5	1	0	118.3	117.7	7	2	1	19.6	19.4
7	1	0	129.9	126.2	9	2	1	52.1	56.0
9	1	0	58.3	58.7	11	2	1	41.1	39.0
11	1	0	26.2	19.6	4	3	1	159.2	136.2
2	2	0	223.3	178.5	6	3	1	121.6	114.4
4	2	0	138.2	113.1	8	3	1	217.8	204.1
6	2	0	154.4	143.0	10	3	1	204.1	201.3
8	2	0	73.7	77.9	12	3	1	112.8	118.3
10	2	0	65.1	70.3	5	4	1	90.2	80.2
12	2	0	21.9	23.2	7	4	1	116.8	104.6
3	3	0	110.9	119.9	9	4	1	63.9	61.0
5	3	0	63.9	56.7	11	4	1	78.6	76.6
7	3	0	27.6	4.4	6	5	1	108.9	111.1
9	3	0	31.8	28.8	8	5	1	156.4	155.7
11	3	0	11.8	16.4	10	5	1	178.1	196.0
4	4	0	811.1	809.8	7	6	1	113.5	109.5
6	4	0	41.9	30.6	9	6	1	122.5	126.0
8	4	0	162.9	172.2	11	6	1	31.4	33.7
10	4	0	13.5	10.1	8	7	1	120.0	112.7
12	4	0	161.9	183.4	10	7	1	69.3	78.9
5	5	0	177.3	162.0	9	8	1	37.5	41.3
7	5	0	68.0	65.2	2	2	2	854.0	867.0
9	5	0	89.4	85.8	4	2	2	145.2	118.6
11	5	0	122.3	126.1	6	2	2	509.3	497.8
6	6	0	95.9	92.4	8	2	2	39.1	30.6
8	6	0	29.3	37.3	10	2	2	209.2	220.5
10	6	0	63.0	69.0	12	2	2	23.5	29.0
7	7	0	13.6	4.2	3	3	2	109.0	109.4
9	7	0	123.3	130.7	5	3	2	109.5	95.0
8	8	0	265.0	271.5	7	3	2	83.4	79.2
10	8	0	27.1	20.0	9	3	2	139.6	135.1
9	9	0	137.0	148.2	11	3	2	51.6	54.3

Table 2.5 (continued)

Comparison of Observed and Calculated Structure Factors

for Tetrahedrite   (R = 6.7%)

h	k	l	F_{obs}	F_{cal}	h	k	l	F_{obs}	F_{cal}
4	4	2	118.8	97.8	9	6	3	72.6	69.7
6	4	2	101.1	94.6	8	7	3	135.3	131.8
8	4	2	69.5	72.5	10	7	3	76.4	96.9
10	4	2	54.0	62.4	9	8	3	65.2	78.0
12	4	2	3.5	16.9	4	4	4	320.6	313.1
5	5	2	40.6	48.9	6	4	4	53.8	52.6
7	5	2	124.2	122.4	8	4	4	373.4	372.8
9	5	2	39.6	50.1	10	4	4	27.3	32.8
11	5	2	85.8	92.4	5	5	4	139.9	129.5
6	6	2	352.6	347.1	7	5	4	132.8	130.1
8	6	2	36.8	33.9	9	5	4	113.4	112.1
10	6	2	136.5	143.4	11	5	4	52.8	63.3
7	7	2	119.6	120.0	6	6	4	91.2	92.8
9	7	2	120.1	120.5	8	6	4	6.1	31.6
8	8	2	39.1	37.6	10	6	4	30.3	40.5
4	3	3	172.3	151.8	7	7	4	80.1	75.5
6	3	3	142.3	140.5	9	7	4	65.7	76.8
8	3	3	137.3	148.7	8	8	4	85.1	88.7
10	3	3	116.5	121.8	6	5	5	156.5	162.5
12	3	3	153.0	171.1	8	5	5	85.3	80.8
5	4	3	104.3	99.7	10	5	5	80.6	81.1
7	4	3	80.6	88.5	7	6	5	74.2	75.6
9	4	3	63.5	62.2	9	6	5	30.4	28.8
11	4	3	49.5	49.3	8	7	5	96.4	109.8
6	5	3	204.7	193.7	6	6	6	198.2	201.7
8	5	3	112.7	107.8	8	6	6	32.8	47.4
10	5	3	95.3	96.7	7	7	6	60.3	57.3
7	6	3	103.0	97.5	7	6	7	60.3	57.3
					8	7	7	27.7	41.0

parameters proposed by Pauling and Neuman have changed by as much as .12 $\overset{o}{A}$. Otherwise the structure as originally proposed is essentially correct.

Figure 2.2 presents electron density sections at $\underline{z} = 0$, $\frac{1}{8}$ and $\frac{1}{4}$. All atoms in the asymmetric unit lie in or near one of these sections. One half of the unit cell is shown for each section. The remainder of the cell is related to the portion shown by diagonal mirror planes and a 2-fold axis at $\frac{1}{2}$ $\frac{1}{2}$. F_{000} was included in these syntheses. The zero contour is dotted, other contours are drawn at equal but arbitrary intervals. No negative regions were present which were below zero by an amount equal to the contour interval shown. Small peaks surround each of the peaks which represent an atom location. These peaks are due to series termination effects as evidenced by the fact that they occur at the same distance from each atom location, and also by the fact that they did not appear in difference syntheses.

A subcell given by $|a_1'| = |a_2'| = \frac{1}{4}|a_1|$ or $\frac{1}{8}|a_1|$, as required, has been given in these maps. All atoms in an ideal sphalerite-like arrangement would lie exactly in the sections and would occur at one of the lattice points of the subcell. The displacements, $\Delta \underline{z}$, of each atom from the plane of the section, and the position of the peak relative to the neighboring grid point provide a picture of the magnitude of the distortion from the sphalerite-like arrangement. The position of the S atom required to complete the sphalerite arrangement is at $(\frac{7}{8} \frac{1}{8})$ in the section $\underline{z} = \frac{1}{8}$. There is no evidence for electron density in this site as had been proposed by Machatschki (1928b) and Pauling and Neuman to explain variations in S content of the mineral.

The arrangement of atoms in the structure is visualized most easily in terms of the linkage of the polyhedra formed by the metal atoms about the sulfur atoms. Figure 2.3 illustrates this arrangement for one-half of a unit cell. Cu(2) is in octahedral coordination about S(2). These octahedra are located at the origin and the body-centered position of the unit cell. A distorted tetrahedron of 3 Cu and 1 Sb shares

Figure 2.2

Electron density sections of tetrahedrite

a) $z = 0$

b) $z = \frac{1}{8}$

c) $z = \frac{1}{4}$

All atoms in the asymmetric unit lie close to these sections. Atoms in an undistorted sphalerite arrangement lie exactly in these sections and on the subnets given by $a_1' = \frac{1}{8}a_1$, $a_2' = \frac{1}{8}a_2$.
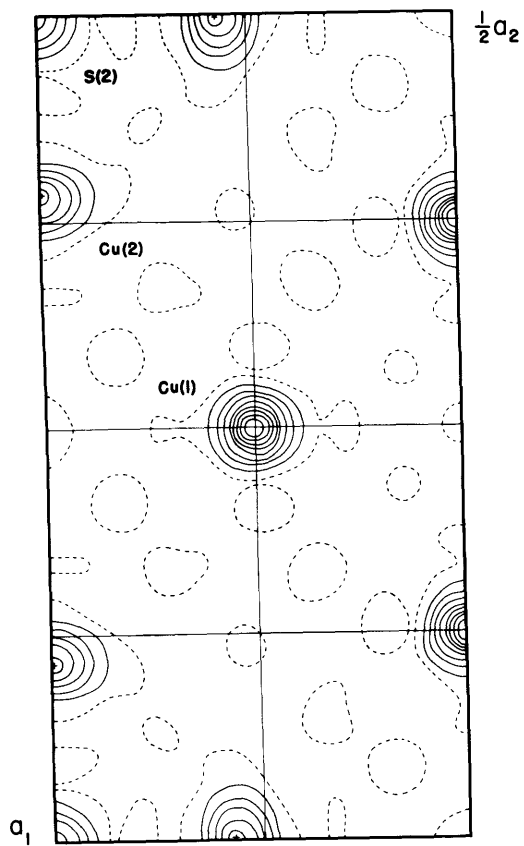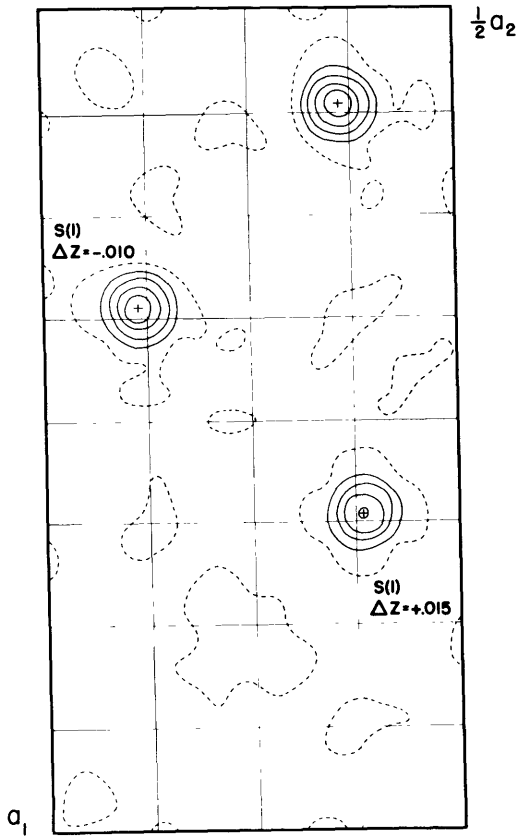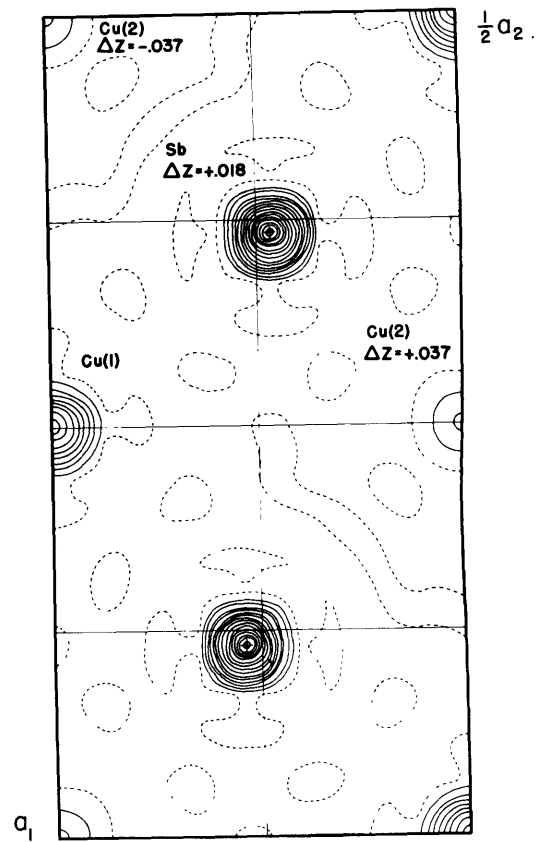
(a) z = 0   (b) z = $\frac{1}{8}$ (c) z = $\frac{1}{4}$

Figure 2. 3

Arrangement of metal atom polyhedra in one half of a unit cell of tetrahedrite. Sb locations are indicated by small circles. All other vertices of the polyhedra represent Cu locations.
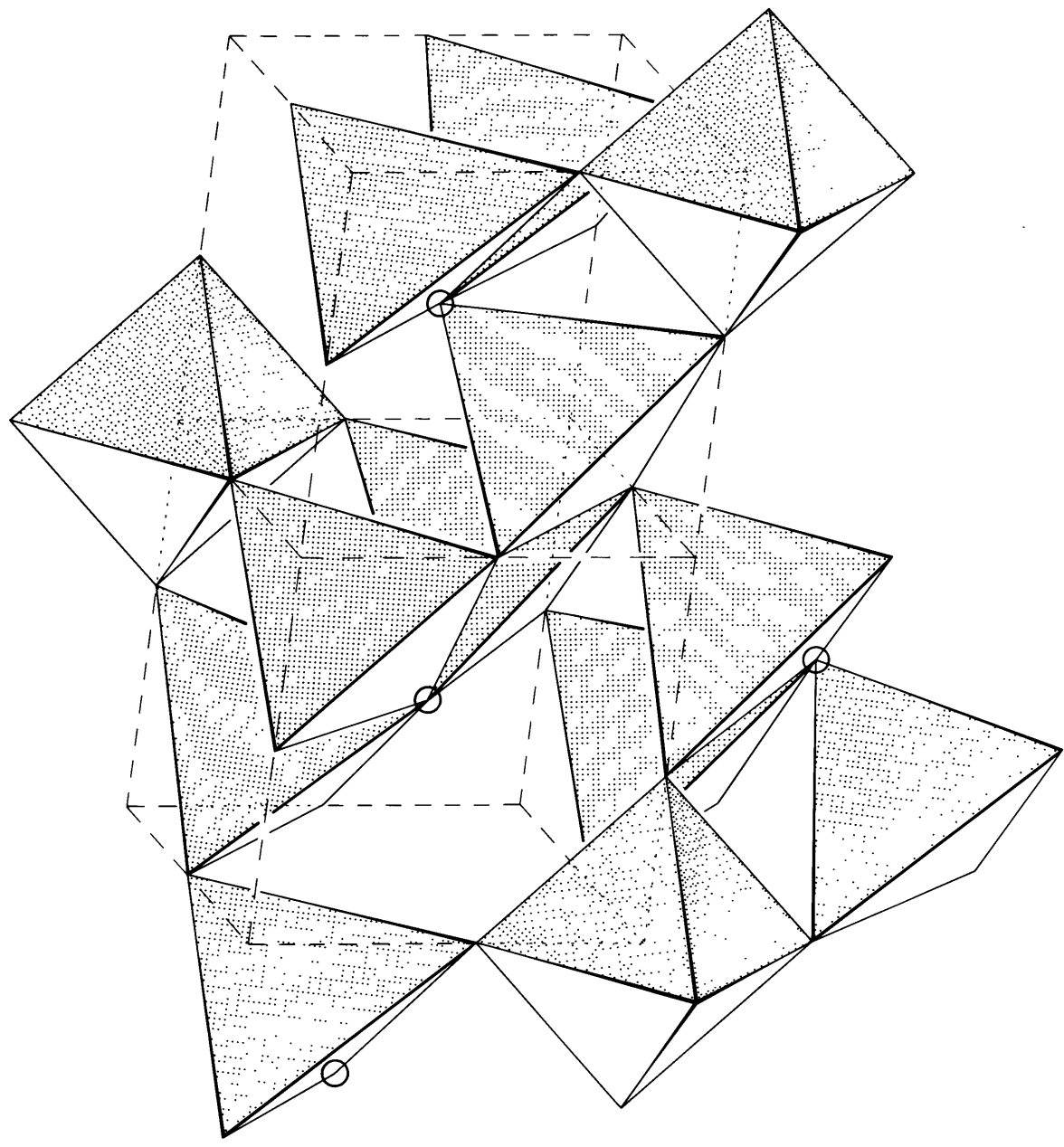
one corner with this tetrahedron. The remaining three corners of the tetrahedron are each joined to corners of a second tetrahedron in a sphalerite-like arrangement. These second tetrahedra are each linked in turn to another octahedron. The locations of the Sb atoms, indicated in Fig. 2.3 by small circles, are located at those corners of the tetrahedra which are closest to the octahedra. A large hole exists in the structure where the S atom is missing from the completed sphalerite arrangement. This is apparent in Fig. 2.3 at the left-hand corner of the cell.

Interatomic distances and bond angles for the structure are given in Tables 2.6 and 2.7, respectively. There are two types of sulfur atoms in the structure. S(2) is surrounded by six Cu (2) atoms at 2.210 $\mathring{A}$ which form a regular octahedron. S (1) is tetrahedrally coordinated by two Cu (1) at 2.343 $\mathring{A}$, one Cu (2) at 2.292 $\mathring{A}$ and one Sb at 2.436 $\mathring{A}$. The bond angles in the tetrahedron, Fig. 2.4, range from $101°1'$ to $117°15'$. This is an appreciable distortion from the angle of $109°28'$ which would be found in a regular tetrahedron.

Consideration of the arrangement of the polyhedra of metal atoms about S facilitates visualization of the structure and its relation to sphalerite. This representation, however, obscures the reason for this curious arrangement of atoms. Figure 2.5 illustrates the arrangement of sulfur atoms about the metal atoms of the structure. Cu (1) is tetrahedrally coordinated by S (1). The bond angles of this tetrahedron are all equal to $110°47'$, which represents a very slight distortion from a regular tetrahedron. Cu (2) is trigonally coordinated by two S (1) at 2.292 $\mathring{A}$ and one S (2) atom at 2.210 $\mathring{A}$. The group lies in a symmetry plane and thus is required to be planar. The Sb atom is also in 3-fold coordination. Three S (1) atoms are located about a 3-fold axis at 2.436 $\mathring{A}$ from Sb. The S-Sb-S bond angle, Fig. 2.5, is $90°32'$.

The interatomic distances are in good agreement with those found in other copper sulfides. The unusual copper atom in three-fold coordination has also been found in stromeyerite, CuAgS (Frueh, 1955).

Table 2.6

Interatomic Distances in Tetrahedrite

	Atom	Number and type of neighbor	Distance (Å)
S atoms	S(1)	2 Cu(1)	2.343
		1 Cu(2)	2.292
		1 Sb	2.436
	S(2)	6 Cu(2)	2.210
Metal atoms	Cu(1)	4 S(1)	2.343
	Cu(2)	2 S(1)	2.292
		1 S(2)	2.210
	Sb	3 S(1)	2.436

Table 2.7

Bond Angles in Tetrahedrite

	Central atom	Bonds	Angle
S atoms	S (1)	Cu (1)-S (1)-Sb	101° 1'
		Cu (1)-S (1)-Cu(1)	103° 17'
		Cu (2)-S (1)-Sb	114° 33'
		Cu (1)-S(1)-Cu (2)	117° 15'
Metal atoms	Cu (1)	S (1)-Cu (1)-S (1)	110° 47'
	Cu (2)	S (1)-Cu (2)-S (2)	132°8'
		S (1)-Cu (2)-S (1)	92° 45'
	Sb	S (1)-Sb-S (1)	90° 32'

Figure 2.4

Bond lengths and angles of metal atom coordination about the sulfur atoms in tetrahedrite.

Cu2

Cu2

Cu2   S2

Cu2   2.210Å   Cu2

Cu2

Cu2

Cu1
2.343Å   Sb
2.436Å

101°1'

103°17'   S1   114°33'

Cu1
2.343Å   117°15'

Cu2
2.292Å
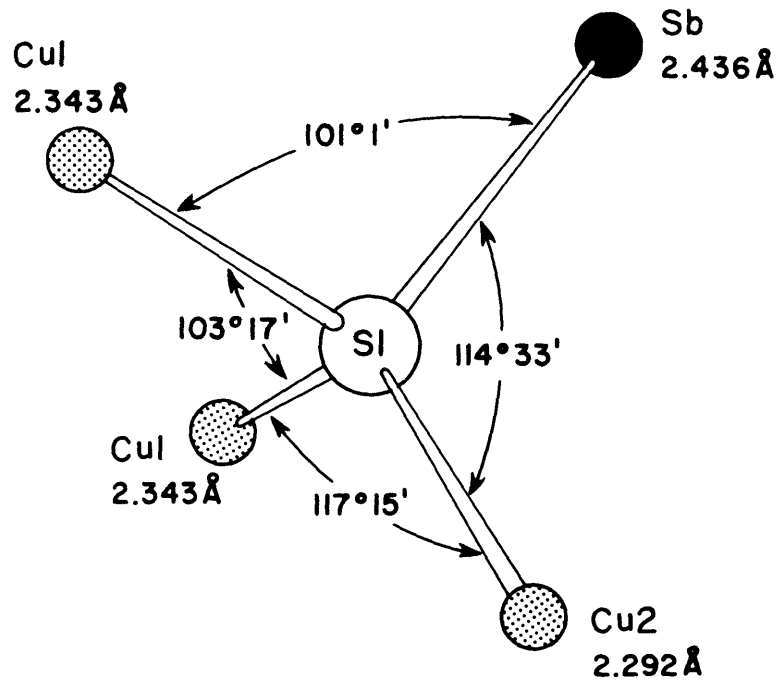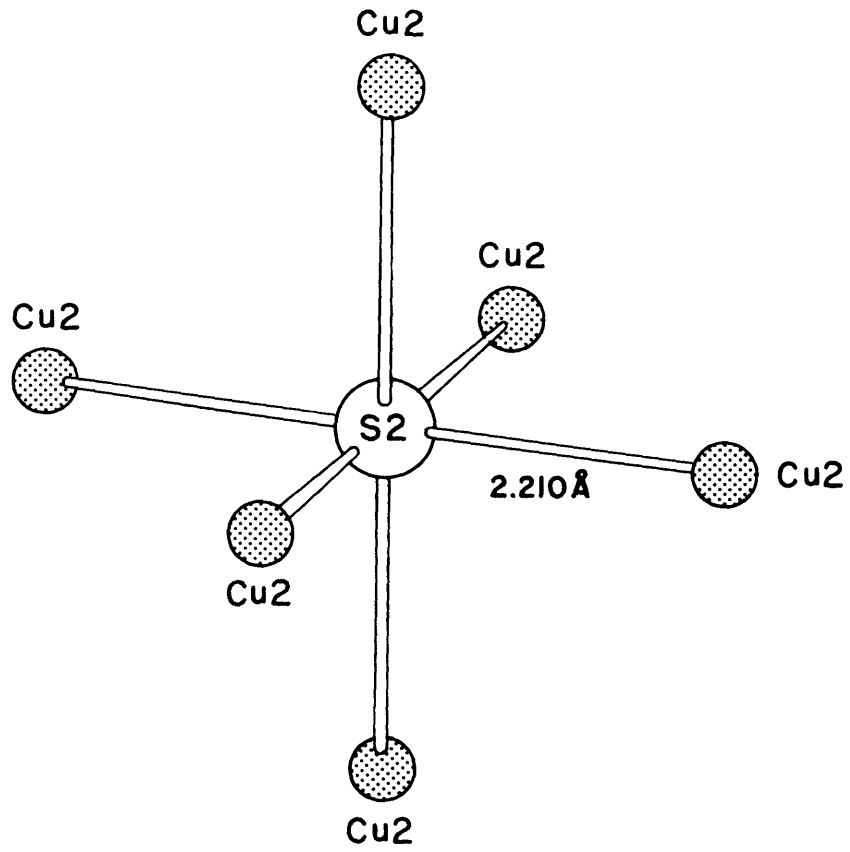
Figure 2.5

Bond lengths and angles of sulfur atom coordination about the metal atoms in tetrahedrite.

90°32'

Sb

SI

2.436Å

SI

SI

SI
2.292Å

95°45'

132°8'

Cu2

S2
2.210Å

SI
2.292Å

132°8'

SI

110°47'

SI

2.343Å

Cul

SI

SI
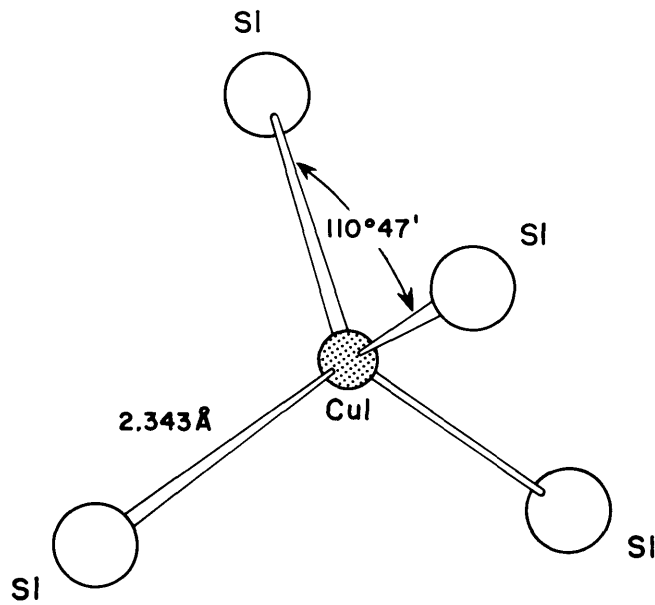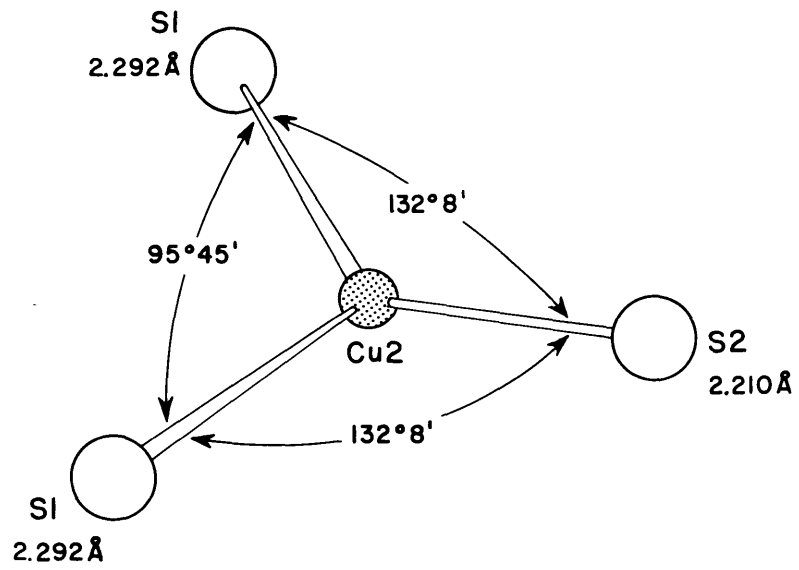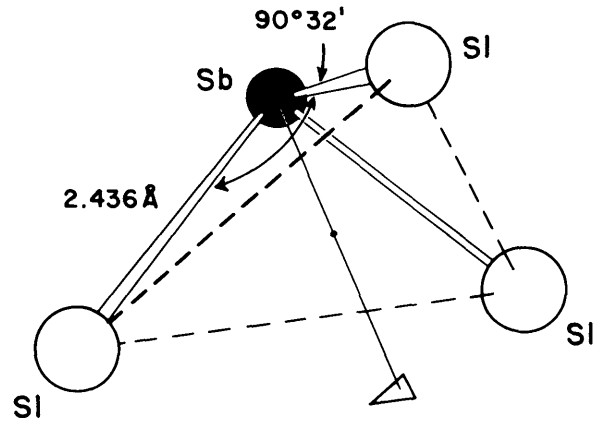
This group also displays one short and two long bonds of 2.26 and 2.29 $\overset{\circ}{A}$ respectively. Regular trigonal groups are found in covellite, CuS (Berry, 1954) and chalcocite, Section III, with bond-lengths of 2.19 and 2.28 $\overset{\circ}{A}$ respectively. The bond length 2.343 $\overset{\circ}{A}$ in the nearly-regular Cu (1)-S (1) tetrahedron is in agreement with the distances 2.34 and 2.30 $\overset{\circ}{A}$ found for the tetrahedral Cu in covellite.

The Sb-S (1) coordination is quite interesting. The structures of several sulfide minerals which contain Sb have been determined. The Sb atom in most of these structures has three nearest S neighbors, but the distances to these atoms are quite irregular. Berthierite, $FeSb_2S_4$ (Buerger and Hahn, 1955), livingstonite, $HgSb_4S_8$ (Niizeki and Buerger, 1957a), jamesonite, $FePb_4Sb_6S_{14}$ (Niizeki and Buerger, 1957b) and stibnite, Sb_2S_3 (Scavnicar, 1960) all display Sb-S nearest-neighbor distances which range between a minimum distance of between 2.44 and 2.49 $\overset{\circ}{A}$ (for one neighbor only) to large distances of 3.6 and 3.7 $\overset{\circ}{A}$. The three Sb-S bonds in tetrahedrite are in excellent agreement with the shortest bond length found in these structures. The length and orthogonal arrangement of these bonds therefore suggests a strong covalent bond involving the p^3 electrons of Sb. This explains why the fourth sulfur atom is missing from the sphalerite-like arrangement and why Sb does not merely substitute for Cu to form a completed sphalerite-like derivative structure similar , for example, to chalcopyrite. It is misleading to state that Sb substitutes for a tetrahedral Cu in tetrahedrite. The SbS_3 group is really a different type of coordination polyhedron.

One final aspect of the structure deserves discussion. A disturbing feature of the final isotropic temperature factors listed in Table 2.2 was the large temperature factor obtained for Cu (2). When anisotropic temperature factors were employed, however, it was found that this was due to a large component of thermal displacement normal to the triangular CuS_3 group. This motion is reasonable for an atom in planar coordination. Furthermore, the temperature motion for the other atoms remained isotropic within the limits of the standard deviations.

It is therefore felt that the anisotropic temperature factor coefficients presented in Table 2.4 give a realistic description of the thermal motion of the atoms.

2.8 References

Berry, L.G. (1954). The crystal structure of covellite, CuS and klockmannite, CuSe. Am.Mineral.39, 504-509.

Bond, W.L. (1951). Making small spheres. Rev.Sci.Instr.22, 344-345.

Bond, W.L. (1959). Sphere of radius R, bathed in a uniform incident x-ray beam. Section 5.3.6, International Tables for X-ray Crystallography, Vol. 2 (Kynoch Press, Birmingham) 302-305.

Buerger, M.J. (1942). X-ray crystallography. (John Wiley and Sons, New York) 435-453.

Buerger, M.J. and Hahn, Theodor (1955). The crystal structure of berthierite, $FeSb_2S_4$. Am.Mineral.40, 226-238.

Burnham, Charles W. (1961). The structures and crystal chemistry of the aluminum-silicate minerals, Ph.D. thesis, Department of Geology and Geophysics, Massachusetts Institute of Technology.

Cruickshank, D.W.J.; Pilling, Diana E.; Bujosa, A; Lovell, F.M.; and Truter, Mary E. (1961). Crystallographic calculations on the Ferranti Pegasus and Mark I computers, in Computing Methods and the Phase Problem in X-ray Crystal Analysis. (Ray Pepinsky, J.M.Robertson, and J.C.Speakman, ed., Pergamon Press, New York), 46.

Frueh, Alfred J. (1955). The crystal structure of stromeyerite, AgCuS: A possible defect structure. Zeit.Krist.106, 299-307.

Hamilton, W.C. (1959). On the isotropic temperature factor equivalent to a given anisotropic temperature factor. Acta Cryst. 12, 609-610.

Kretschmer, A. (1911). Analyse und Chemische Zusammensetzung der Fahlerze. Zeit.Krist. 48, 484-513.

Levy, Henri A. (1956). Symmetry relations among coefficients of the anisotropic temperature factor. Acta Cryst. 9, 679 (Only).

Machatschki, Felix (1928a) Formel und Kristall-struktur des Tetraedrites. Norsk.Geol.Tidsskr. 10, 23.

Machatschki, Felix (1928b). Präzisionsmessungen der Gitter-konstanten verchiedener Fahlerze. Formel und Struktur derselben. Zeit.Krist. 68, 204-222.

Niizeki, N. and Buerger, M.J. (1957a). The crystal structure of livingstonite, $HgSb_4S_8$. Zeit.Krist. 109, 129-157.

Niizeki, N. and Buerger, M.J. (1957b). The crystal structure of jamesonite, $FePb_4Sb_6S_{14}$. Zeit.Krist. 109, 161-183.

Palache, Charles; Berman, Harry, and Frondel, Clifford (1944). The System of Mineralogy, Vol. I. Elements, Sulfides, Sulfosalts, Oxides. (John Wiley and Sons, New York, Seventh edition) 374-384.

Pauling, Linus and Neuman, E.W. (1934). The crystal structure of binnite $(Cu, Fe)_{12}As_4S_{13}$, and the chemical composition and structure of minerals of the tetrahedrite group. Zeit.Krist. 88, 54-62.

Prewitt, Charles T. (1960). The parameters Υ and ϕ for equi-inclination, with application to the single-crystal counter diffractometer. Zeit.Krist. 114, 355-360.

Prewitt, Charles T. (1962). Structures and crystal chemistry of wollastonite and pectolite. Ph.D.thesis, Department of Geology and Geophysics, Massachusetts Institute of Technology.

Prior, G.T. and Spencer, L.J. (1899). The identity of binnite with tennantite; and the chemical composition of Fahlerz. Min.Mag. 12, 184-213.

Scavnicar, S. (1960). The crystal structure of stibnite. A redetermination of atomic positions. Zeit.Krist. 114, 85-97.

Section III

The Crystal Structure of Chalcocite, Cu_2S.

3.1 Introduction

Until about twenty years ago, it was believed that chalcocite, Cu_2S, was dimorphous and existed in orthorhombic and isometric modifications. N.W.Buerger (1941), however, showed that while chalcocite was indeed orthorhombic below about $110^\circ C$, stoichiometric Cu_2S actually transformed to a hexagonal phase. Compositions deficient in copper, on the other hand, transformed into this hexagonal phase plus an isometric phase. The isometric structure had composition near Cu_9S_5 and was shown to be identical with what had been called isometric chalcocite (N.W.Buerger, 1942). The name digenite was proposed for this cubic modification. Electrical conductivity measurements (Hirahara, 1947) indicated a further phase transition in Cu_2S at $450^\circ C$. Ueda (1949) found that this new phase was similar to digenite. In a careful re-examination of the phase relations in the system, Djurle (1958a) confirmed this transformation, but, in addition, discovered two new phases at composition $Cu_{1.96}S$. At room temperature crystals of this composition had an unidentifiable structure of low symmetry. This phase has subsequently been found in nature and has been given the name djurleite (Roseboom, 1962; Morimoto, 1962). At higher temperatures, $Cu_{1.96}S$ formed a relatively simple metastable tetragonal structure. It was found that all compositions between Cu_2S and $Cu_{1.8}S$ transformed into a digenite-like phase at a sufficiently high temperature. Digenite may therefore be described as $Cu_{2-x}S$ with x between 0 and at least 0.2.

The nomenclature "low-chalcocite" and "high-chalcocite" will be preserved in this paper for the orthorhombic and hexagonal modifications, respectively, of stoichiometric Cu_2S. The two phases are related by a reversible transformation. The high temperature form cannot be quenched. M.J.Buerger and N.W.Buerger (1944) showed

that an interesting substructure-superstructure relation exists between the unit cells of the two structures. The diffraction patterns of low-chalcocite contained weak reflections in addition to those displayed by the hexagonal form. These additional reflections indicated that the axes of the low-chalcocite unit cell were multiples of 3, 4 and 2 of the cell edges of the orthohexagonal cell of high-chalcocite in the $\underline{a}$, $\underline{b}$ and $\underline{c}$ directions respectively. This relation is illustrated in Fig. 3.1, in which the lattice points of the A-centered low-chalcocite cell are given by solid points, and the lattice points of the hexagonal high-chalcocite cell by open points. The diffraction symbol for high-chalcocite permitted $P6_3\underline{mc}$, $P\bar{6}2\underline{c}$ and $P6_3/\underline{mmc}$ as possible space groups; low-chalcocite had $A\underline{bmm}$, $A\underline{b}2\underline{m}$ and $A\underline{bm}2$ as possible space groups. By assuming that the space group of low-chalcocite was derived from that of high-chalcocite through the suppression of certain symmetry elements, it was possible to assign space group $A\underline{b}2\underline{m}$ (C_{2v}^{15}) to low-chalcocite, and space group $P6_3/\underline{mmc}$ (D_{6h}^4) to high-chalcocite. The acentric ortho-rhombic structure contains 96 Cu_2S per cell, and is quite complex. The hexagonal cell of high-chalcocite, on the other hand, contains only 2 Cu_2S per cell.

An attempt to solve the relatively simple high-chalcocite structure from powder data (Klubock and Buerger, 1945, unpublished) was unsuccessful. Belov and Butuzov (1946), however, considered the several reasonable structures permitted by the high-chalcocite space group. They proposed as a structure that model which gave the best fit with a set of intensities estimated from the high-chalcocite Weissenberg photograph published by Buerger and Buerger (1944). The agreement was rather unsatisfactory. Ueda (1949) attempted a structure determination on the basis of visual estimation of intensities from powder patterns. None of the likely structures permitted by the space group yielded a satisfactory set of calculated structure factors. Calculations were also made for arrangements of sulfur atoms alone. Curiously, it was found that a hexagonal close-packed arrangement

Figure 3. 1

The relation between the A-centered orthorhombic unit-cell of
low-chalcocite, the C-centered ortho-hexagonal unit-cell of high-chalcocite,
and the hexagonal unit-cell of high-chalcocite. Note that the 6-fold and
3-fold axes in high-chalcocite lie in the section (0yz) of the ortho-
hexagonal cell.

C LOW

C HIGH

b HIGH

a HIGH

a LOW

b LOW
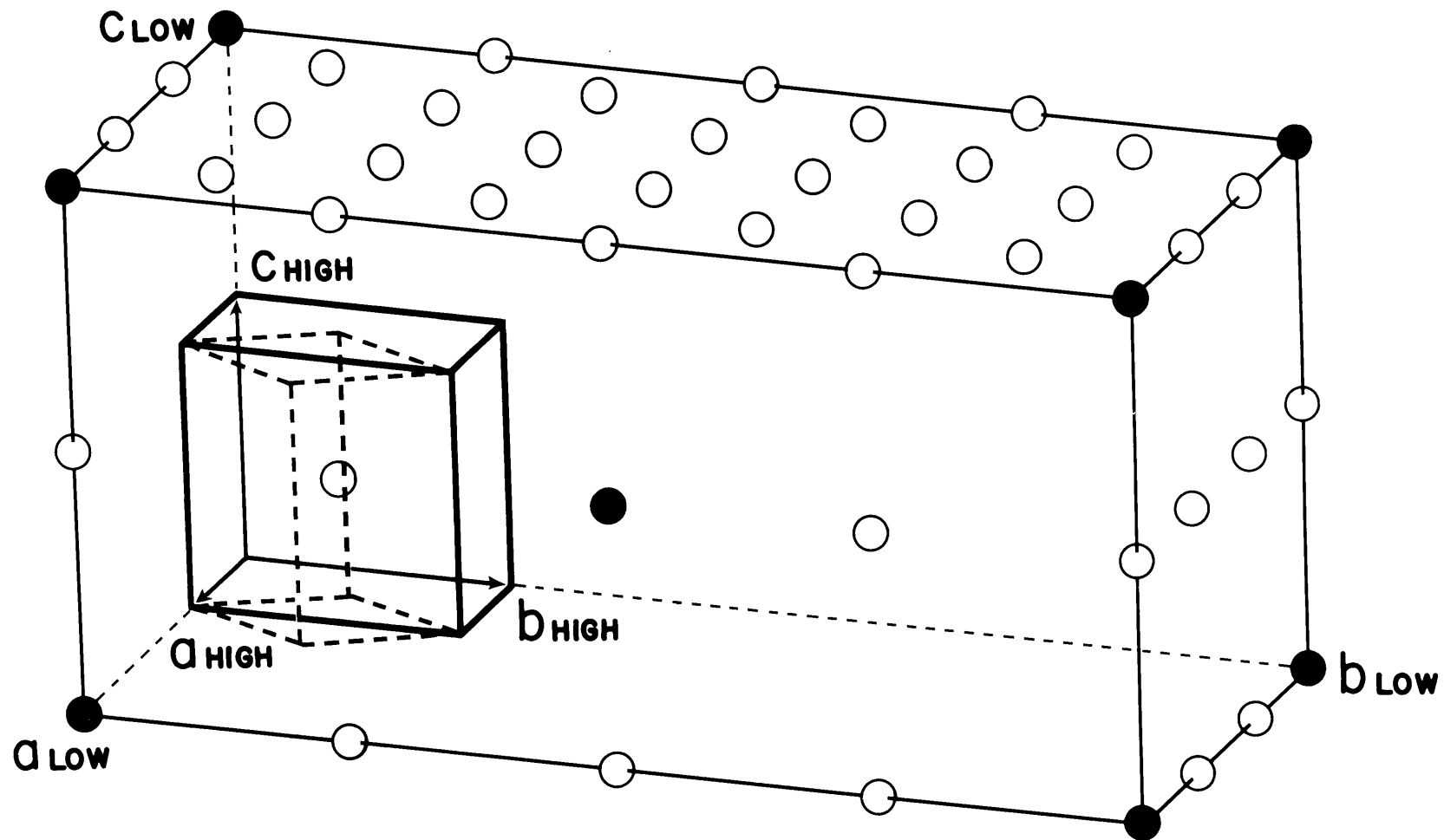
gave structure factors in reasonable agreement with those observed. From this Ueda concluded that the copper atoms were in "complete disorder".

This section describes a single-crystal investigation of the structure of high-chalcocite and the low-chalcocite substructure.

3.2 Equipoint Restrictions and Nature of the Patterson function for High-Chalcocite

The unit cell of high-chalcocite contains only 2 Cu_2S. This requires that both the Cu and S atoms occupy special positions in an ordered structure. Table 3.1 lists possible equipoints for the probable high-chalcocite space group $P6_3/mmc$. It is interesting to note that examination of the other two possible space groups $P\bar{6}2c$ and $P6_3mc$ shows that the former has special positions identical with those listed, and that the latter has but two possibilities which are included in the list. The S atoms may be accommodated in only one equipoint of rank 2. The Cu atoms may be accommodated in either two equipoints of rank 2, or a single equipoint of rank 4. A total of 20 arrangements of atoms in these equipoints is possible. Three possibilities, however, result in c being half that actually observed and may be discarded. Of the remaining arrangements, only 9 combinations are distinct.

Solution of a three-dimensional Patterson function involving atoms in these equipoints may be considerably simplified by noting that these special positions lie on the 3-fold and 6-fold axes in the hexagonal cell. These axes all lie on a (11·0) plane through the hexagonal cell. Figure 3.1 shows that this plane is equivalent to the section 0yz in the orthohexagonal cell. Analysis of three-dimensional Patterson maps may therefore be reduced to a two-dimensional problem, since only this special section need be considered. Equipoint coordinates in this section are also given in Table 3.1.

Table 3.1

Special positions lying on the 6-fold and 3-fold axes in space groups

$P6_3/\underline{mmc}$ and $P\bar{6}2\underline{c}$

Equipoint	Coordinates in hexagonal cell		Corresponding coordinates in 2-dimensional representation	
$\underline{2a}$	$0\,0\,0$	$0\,0\,\frac{1}{2}$	$0\,0$	$0\,\frac{1}{2}$
$\underline{2b}$	$0\,0\,\frac{1}{4}$	$0\,0\,\frac{3}{4}$	$0\,\frac{1}{4}$	$0\,\frac{3}{4}$
$\underline{2c}$	$\frac{1}{3}\,\frac{2}{3}\,\frac{1}{4}$	$\frac{2}{3}\,\frac{1}{3}\,\frac{3}{4}$	$\frac{2}{3}\,\frac{1}{4}$	$\frac{1}{3}\,\frac{3}{4}$
$\underline{2d}$	$\frac{1}{3}\,\frac{2}{3}\,\frac{3}{4}$	$\frac{2}{3}\,\frac{1}{3}\,\frac{1}{4}$	$\frac{2}{3}\,\frac{3}{4}$	$\frac{1}{3}\,\frac{1}{4}$
$\underline{4e}$	$0\,0\,\underline{z}$	$0\,0\,\underline{\bar{z}}$	$0\,\underline{z}$	$0\,\underline{\bar{z}}$
	$0\,0\,\frac{1}{2}+\underline{z}$	$0\,0\,\frac{1}{2}-\underline{z}$	$0\,\frac{1}{2}+\underline{z}$	$0\,\frac{1}{2}-\underline{z}$
$\underline{4f}$	$\frac{1}{3}\,\frac{2}{3}\,\underline{z}$	$\frac{2}{3}\,\frac{1}{3}\,\underline{\bar{z}}$	$\frac{2}{3}\,\underline{z}$	$\frac{1}{3}\,\underline{\bar{z}}$
	$\frac{2}{3}\,\frac{1}{3}\,\frac{1}{2}+\underline{z}$	$\frac{1}{3}\,\frac{2}{3}\,\frac{1}{2}-\underline{z}$	$\frac{1}{3}\,\frac{1}{2}+\underline{z}$	$\frac{2}{3}\,\frac{1}{2}-\underline{z}$

3.3 Preliminary Investigation of the Low-Chalcocite Structure

An attempt was first made to directly determine the crystal structure of low-chalcocite. A suitable single-crystal fragment was obtained from a coarse crystal of Bristol, Connecticut, chalcocite. Chalcocite from this locality is quite stoichiometric. Posnjak et al. (1915) report a ratio of Cu : S of 2.007 : 1. Also, the inversion of this material to the hexagonal high-chalcocite structure was later confirmed. Djurle's (1958a) study of the phase relations near Cu_2S would therefore require any Cu deficiency to be less than that corresponding to a composition $Cu_{1.96}S$.

Using an equi-inclination Geiger-counter diffractometer, all of the accessible independent reflections in a $MoK\alpha$ sphere were investigated. The superstructure reflections were generally quite weak and a large number were not detectable. A total of 584 independent intensities were collected. Of these, 76, or 13%, were substructure reflections. Appropriate corrections were made for Lorentz and polarization factors. Absorption was not too serious, and no correction for this effect was made.

A set of three-dimensional Patterson maps were synthesized. As might be expected, these were completely dominated by the marked substructure and proved to be uninterpretable. It was then hoped that analysis of the substructure alone might indicate both the structure of high-chalcocite and yield some clue to the nature of the distortions responsible for the low-chalcocite superstructure.

Accordingly, three-dimensional Patterson maps were synthesized using only squares of structure factors obtained from the substructure reflections. The program ERFR2, written by Sly, Shoemaker and Van den Hende (unpublished) for the IBM 7090 computer, was employed. The substructure reflections had marked pseudo-hexagonal symmetry. The departures from this symmetry were significant enough, however, to warrent treatment of the data as

orthorhombic.

It was found that all peaks in the Patterson function lay in the section 0yz of the orthorhombic cell. The coordinate y assumed values only of 0, $\frac{1}{3}$ or $\frac{2}{3}$. Therefore all electron density in the substructure is located at positions corresponding to special positions on the 3-fold and 6-fold axes in the hexagonal high-chalcocite cell.

The problem could then be treated as a two-dimensional one, as outlined in Section 3.2. The Patterson section P(0yz) is given in Fig. 3.2a. None of the nine possible high-chalcocite structures yielded Patterson maps which compared favorably with this section. In fact, it is readily seen that this map contains contradictory features: the peaks having coordin ates of roughly (0, .3) and ($\frac{1}{3}$, .2) would require Cu in the 4-fold position having a variable parameter, z. On the other hand, the strong peak at ($\frac{1}{3}$, 0) requires Cu in a position having the same z parameter as S, that is, in a symmetry-fixed 2-fold position. This map therefore could not be interpreted in terms of Cu located in positions corresponding to an ordered arrangement of atoms in the high-chalcocite space group. This made it advisable to defer interpretation of this map until a direct determination of the high-chalcocite structure had been made.

3.4 Investigation of the High-Chalcocite Structure

3.4.1 Selection of Material.

Well-crystallized chalcocite from Bristol, Connecticut, was also used for this investigation. An attempt was made to grind spheres from this material with an apparatus similar to that described by Bond (1951). It was found that irregular fragments rapidly assumed the form of oblate ellipsoids but, upon further grinding, became misshapen pellets. The specimen finally selected was untwinned, and had the form of an oblate ellipsoid of revolution with dimensions .505 × .505 × .251 mm. ($\mu_1 r_{max}$ = 6.26, $\mu_1 r_{min}$ = 3.11 for MoKα radiation). It was felt that this regular shape, for which exact absorption corrections could be made, was to be preferred to an irregular pellet

Figure 3.2

(a) Low-chalcocite substructure Patterson section P(0yz) (above).
The lines at $\frac{1}{3}y$ and $\frac{2}{3}y$ correspond to the location of the 3-fold axes in
high-chalcocite. (b) High-chalcocite orthohexagonal Patterson section
P(0yz) (below). The lines at $\frac{1}{3}y$ and $\frac{2}{3}y$ are 3-fold axes in the plane of
the map. F_{000} omitted; contours at equal but arbitrary intervals.
Negative contours dotted, zero contour dashed, positive contours solid
lines.
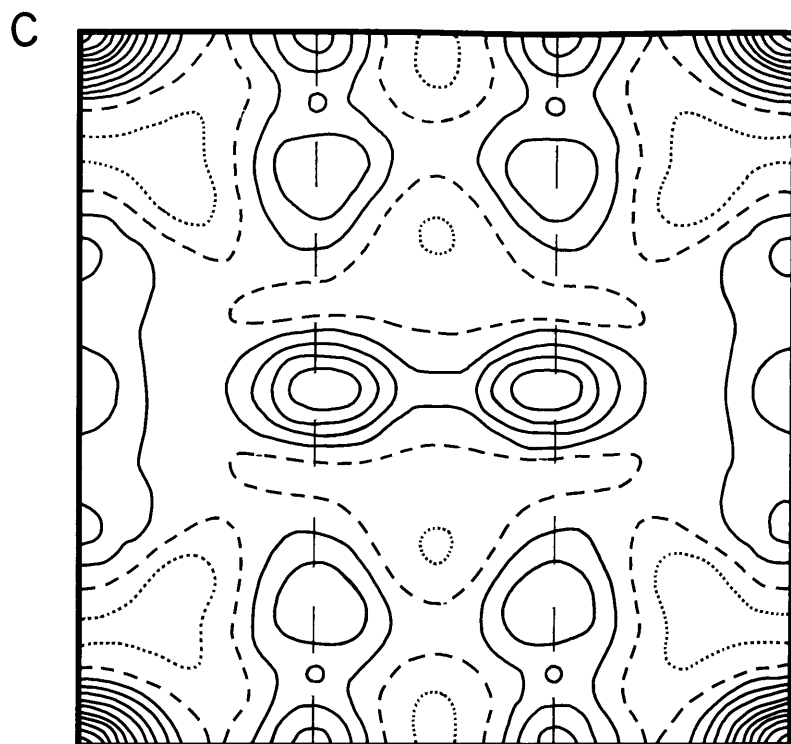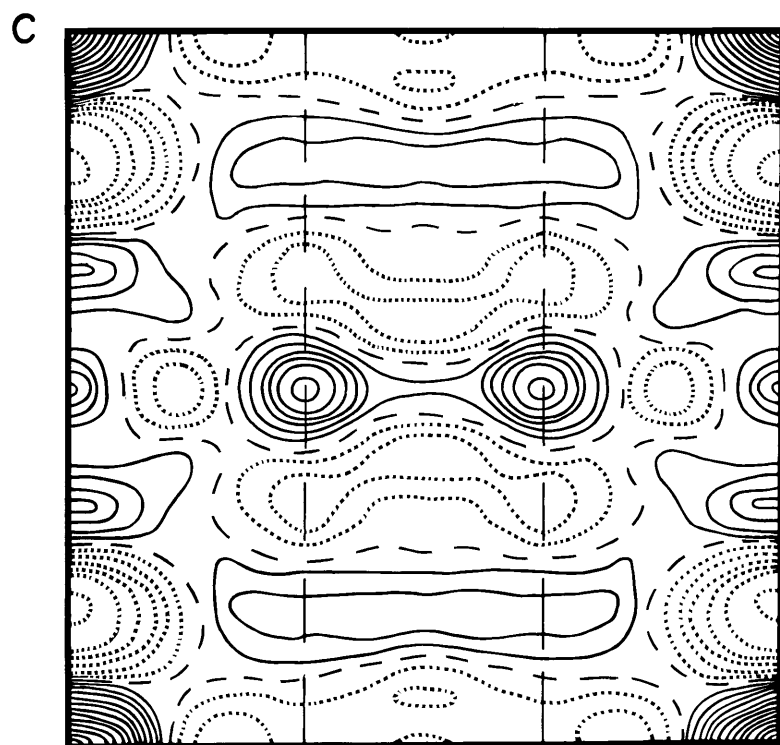
which would require a smaller but less exact correction. Furthermore, the specimen had to be held at an elevated temperature while the intensities were collected. Chalcocite gradually deteriorates when heated in air. The larger regular shape thus had the additional advantage of having a higher volume to surface ratio, which makes this effect less serious.

3.4.2 X-ray Investigation and Collection of Intensities.

A photographic technique was used to record intensities. All reflections on a given level were therefore equally affected by any slight deterioration of the crystal. The method also had the advantage of providing a continuous record of all reflections in a given level during the course of the exposure. Any drop of temperature below the inversion temperature due to malfunction of the heating unit would therefore have been detectable through the appearance of superstructure reflections on the films. Detection of a phase transition would have been more difficult if a counter diffractometer had been used, because of a strong similarity between the high-chalcocite intensities and the low-chalcocite substructure intensities.

The intensities were recorded with the aid of an integrating precession camera. The crystal was maintained at $125^{\circ} \pm 5^{\circ}$ C (15° C above the transformation temperature) with a small radiant heater. This device was similar to one designed by Morimoto and England (1960) and is described in detail in Appendix II. Unit-cell dimensions were determined at this temperature using precession photographs taken with MOK$\underline{\alpha}$ radiation. The values for $\underline{a}$ and $\underline{c}$ are in good agreement with those determined by Buerger and Buerger (1944) and Djurle (1955), as shown in Table 3.2. The precession patterns exhibited symmetry $6/\underline{mmm}$. The only extinction rule observed was $\underline{l} \neq 2\underline{n}$ for reflections of the class hh·l . This confirms the diffraction symbol $6/\underline{mmm}$ P-/--$\underline{c}$ previously given by Buerger and Buerger (1944).

A disadvantage of recording intensities by the precession method is that a blind region obscures certain reflections in the center of upper level films. The radius of this region becomes larger as $\underline{d}^{*}$ increases.

Table 3.2

Unit Cell Dimensions of High-Chalcocite

Temperature	Buerger and Buerger (1944) 112°	Present study[1] 125°	Djurle (1958) 152°	300°	460°
$\underline{c}$ (Å)	6.68	6.75	6.722	6.761	6.806
$\underline{a}$ (Å)	3.89	3.95	3.961	3.981	4.005
$\underline{c/a}$	1.717	1.710	1.697	1.698	1.699

[1] Precision 0.3%, accuracy about 1%.

This usually requires use of several settings of the spindle axis if all attainable reflections are to be recorded (Azaroff, 1954; Buerger, 1960). Fortunately, this problem did not occur in recording the high-chalcocite intensities. Since high-chalcocite is hexagonal, all independent reflections are contained in a $30°$ wedge of reciprocal space bounded by the planes containing $\underset{\sim}{c}^*$ and $\underset{\sim}{a}_1^*$, and containing $\underset{\sim}{c}^*$ and $\underset{\sim}{a}_1^* + \underset{\sim}{a}_2^*$. With the crystal oriented such that $\underline{c}$ was along the spindle axis, and with $\underline{a}$ taken as the precession axis, the first row of independent reflections parallel to $\underline{c}^*$ occurred at a distance $d^*/\tan 30°$ from the film origin. This distance exceeded the radius of the blind spot on all levels. It was therefore possible to record all intensities with but one setting of the spindle axis. Several exposure times were used to insure that the linearity range of the film was not exceeded.

All films were developed simultaneously. Intensities were determined with a Joyce-Loebl Company double-beam recording micro-densitometer. (Details of the film development, and nature of the integrated precession films are given in Appendix III.) A total of 106 reflections were measured. Of 37 independent reflections, 7 were undetectable and were assigned half the minimum observable value. These reflections are equivalent to a complete $CuK\underline{\alpha}$ sphere of data.

3.4.3 Data Reduction. Each spot on a precession film is composed of two reflections. One reflection is generated as the reciprocal lattice point enters the sphere of reflection, the second as it emerges. These two reflections have different Lorentz factors and, unless the crystal is spherical, different transmission factors. The correction which must be applied to an integrated intensity, $\underline{I}$, in order to obtain the square of the structure factor, $\underline{F}$, is therefore

$$\underline{F}^2 \sim (I_1/p\, L_1 T_1) + (I_2/p\, L_2 T_2) = I/p\,(L_1 T_1 + L_2 T_2)$$

in which $\underline{T}$ is the transmission factor, $\underline{L}$ the Lorentz factor and $\underline{p}$ the polarization factor. The subscripts refer to the two reflections which

contribute to the spot. The standard charts from which Lorentz and polarization corrections are usually obtained present normalized values of $1/p(L_1 + L_2)$. Since a correction of the form $F^2 \sim \underline{I}/p(T_1 + T_2)(L_1 + L_2)$ is not equivalent to the proper correction, these charts are useless if a non-spherical absorption correction is to be applied. A special routine was therefore written for the IBM 7090 computer to evaluate individual Lorentz factors for each reflection of the pair composing each spot. Transmission factors for each reflection of the pair were evaluated by means of a special version of the general absorption correction program described in Section V. The ellipsoidal crystal was subdivided into an array of $14 \times 14 \times 14$ volume elements for these computations. After applying these corrections, the rms deviation from the mean of equivalent F^2's was 9.5%.

3.5 Solution of the High-Chalcocite Structure

A three-dimensional Patterson function was synthesized using the set of F^2's obtained. The Patterson section $P(0\underline{y}\underline{z})$ of the ortho-hexagonal cell is presented in Fig. 3.2b for comparison with the corresponding section for the low-chalcocite substructure. It may be noted that the two Patterson sections are quite similar, except that in the high-chalcocite map the contradictory peak at $(0\ \frac{1}{3})$ has diminished. The maxima with variable parameter, $\underline{z}$, however, are no longer discrete peaks, but are instead smeared out over a considerable region of the cell. Figure 3.3, for example, gives Patterson section $P(\underline{x},\underline{y},1/6)$. The distribution of the maximum is practically uniform except for very slight peaks in three symmetric locations about the 3-fold axis. This suggests that the copper atoms are disordered. The map again did not agree favorably with any of the 9 theoretical Patterson maps derived in Section 3.2.

An attempt was made to apply image-seeking methods to the solution of the structure. These results were ambiguous since all

Figure 3.3

High-chalcocite Patterson section $P(xy\frac{1}{6})$. Both the hexagonal

and ortho-hexagonal cell are indicated. Negative contours dotted, zero

contour dashed, positive contours solid lines at half the interval of

Fig. 3.2b.
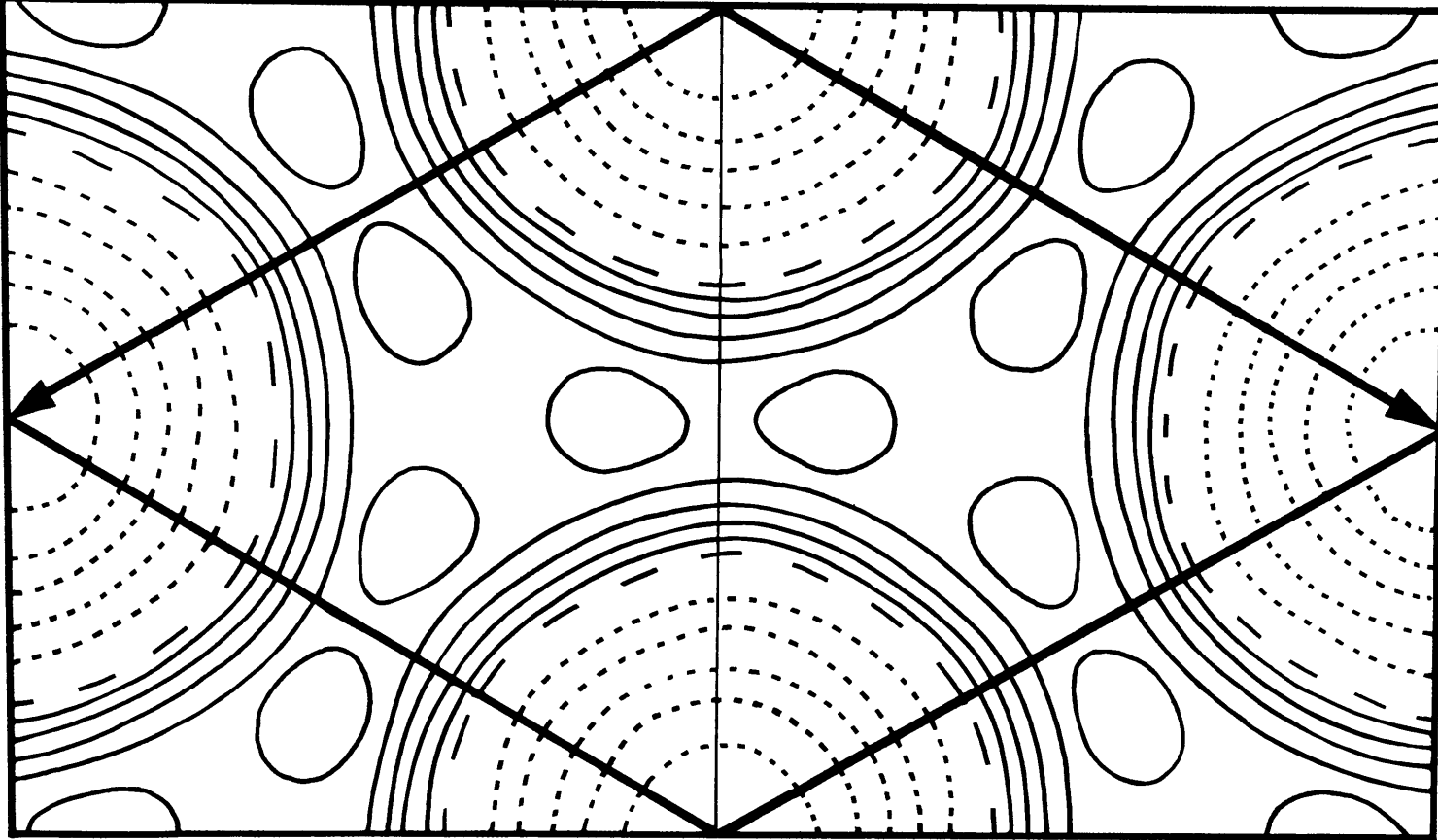
candidate inversion peaks which were investigated proved to be multiple peaks. (In retrospect, the difficulty in interpreting the high-chalcocite Patterson function arose because of the fact that, instead of containing 6 atoms per unit cell, the structure contains 14 positions of high electron density. The Patterson cell therefore contains $14^2 - 14 = 182$ peaks instead of the $6^2 - 6 = 30$ peaks which would occur for an ordered structure. In a given volume, Patterson space therefore contains over six times the number of peaks usually encountered in structure determinations! As a result, most of the peaks are unresolved.)

The structure was solved with the aid of implication theory (Buerger, 1959) and partial Fourier syntheses. In implication theory, the implication diagram $I_n(\underline{xyz})$ for an n-fold axis of symmetry is formed by rotating an appropriate Patterson section an amount $\frac{\pi}{2} - \frac{\pi}{\underline{n}}$, and shrinking the scale of the section by a factor $1/2 \sin (\pi/\underline{n})$. For space groups containing a 6_3 axis, implication diagrams $I_{-6}(\underline{xy}\frac{1}{2})$, based on the operation 6_3, and $I_3(\underline{xy}0)$, based on the operation $6_3{}^2 = 3$ may be prepared. The shrinkage factor for I_{-6} is $1/2 \sin\frac{\pi}{6} = 1$, and the rotation factor is $\frac{\pi}{2} - \frac{\pi}{6} = \frac{\pi}{3} \equiv 0$. The Patterson section $P(\underline{xy}\frac{1}{2})$ therefore is equivalent to $I_{-6}(\underline{xy}\frac{1}{2})$ without change of scale or rotation. The implication diagram $I_{-6}(\underline{xy}\frac{1}{2})$ is a projection of the structure parallel to $\underline{c}$, but with additional "satellite peaks" occurring at distances from the origin which are equal to twice the atomic coordinates. Construction of the implication diagram $I_{-3}(xy0)$ requires shrinkage of the Patterson section $P(\underline{xy}0)$ by a factor $1/2 \sin\frac{\pi}{3} = 1/\sqrt{3}$, and rotation $\frac{\pi}{2} - \frac{\pi}{3} = \frac{\pi}{6}$. This diagram represents a projection of the structure parallel to $\underline{c}$ but with a 3-fold ambiguity, i.e. the projected structure is duplicated about both the 6-fold and the two 3-fold axes of the cell. An additional 2-fold ambiguity of orientation occurs in this diagram because the Patterson function is centrosymmetric. A false center of symmetry is introduced which causes any implication diagram based on a 3-fold axis to display 6-fold symmetry.

Figure 3.4 presents the implication diagrams $I_6(xy\frac{1}{2})$ and $I_3(xy0)$
prepared for high-chalcocite.[1] Both maps indicate that the main portion
of the electron density is confined to locations on the 6_3 and 3-fold axes
of the cell. Some electron density, however, is in a position of higher
rank. High-chalcocite is therefore disordered. The implication diagram
$I_6(xy\frac{1}{2})$ suggests two possible locations for this electron density. The
departure of the peak at $(\frac{1}{3}\frac{2}{3})$ from a circular shape suggests that this
density might occur at positions slightly displaced from the 3-fold axes
at approximately $(x, y) = (.8, .4)$. This location, however, would require
satellite peaks at $(1.6, .8) = (.6, .8)$, modulo Γ. This location is the
deepest minimum occurring on the map, and the suggested position for
the electron density must accordingly be discarded. The second location
suggested by the maps is $(x, y) = (0, \frac{1}{2})$. This location requires a satellite
peak at $(0, 1) = (0, 0)$, modulo Γ. A peak occurs at this location in the
implication map $I_6(xy\frac{1}{2})$, so that $(0, \frac{1}{2})$ is an acceptable location for the
electron density. This location must be verifiable with the implication
map $I_3(xy0)$. This map is dominated by the strong origin peak which
occurs in three locations corresponding to the 3-fold ambiguity of this
map, as described above. There are, however, weak "bridges" between
origin peaks which are compatible with electron density at $(x, y) = (0, \frac{1}{2})$.
In space group $P6_3/mmc$ these parameters correspond to special position
$6g$ $0\frac{1}{2}0$, so that the z parameter is fixed by symmetry.

It was assumed that, as in other disordered sulfides, the metal
atoms were disarranged and the sulfur atoms remained ordered. (This
assumption was later proved correct.) Partial Fourier syntheses and
difference maps were accordingly prepared with S atoms in either simple

---

[1] These maps, especially $I_3(xy0)$, show slight deviations from true
hexagonal symmetry. This occurred because use of the Fourier program
ERFR2 requires treatment of Fourier summations for tetragonal, hexago-
nal and isometric space groups as orthorhombic or monoclinic. The
Patterson functions for high-chalcocite were treated in the orthorhombic
sub-group $Cmcm$. Round-off errors in the summation result in the slight
deviations from hexagonal symmetry which may be noted in the maps.

Figure 3.4

Implication diagrams $I_6(xy\frac{1}{2}) = P(xy\frac{1}{2})$ and $I_3(xy0)$ for high-chalcocite.
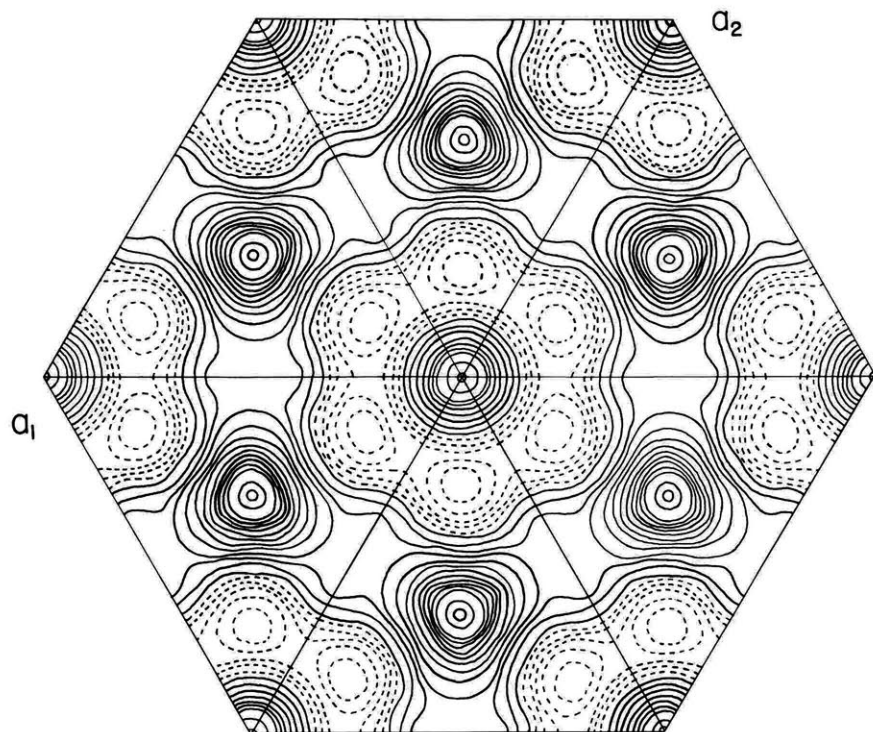
$$I_6(xy\tfrac{1}{2})=P(xy\tfrac{1}{2})$$
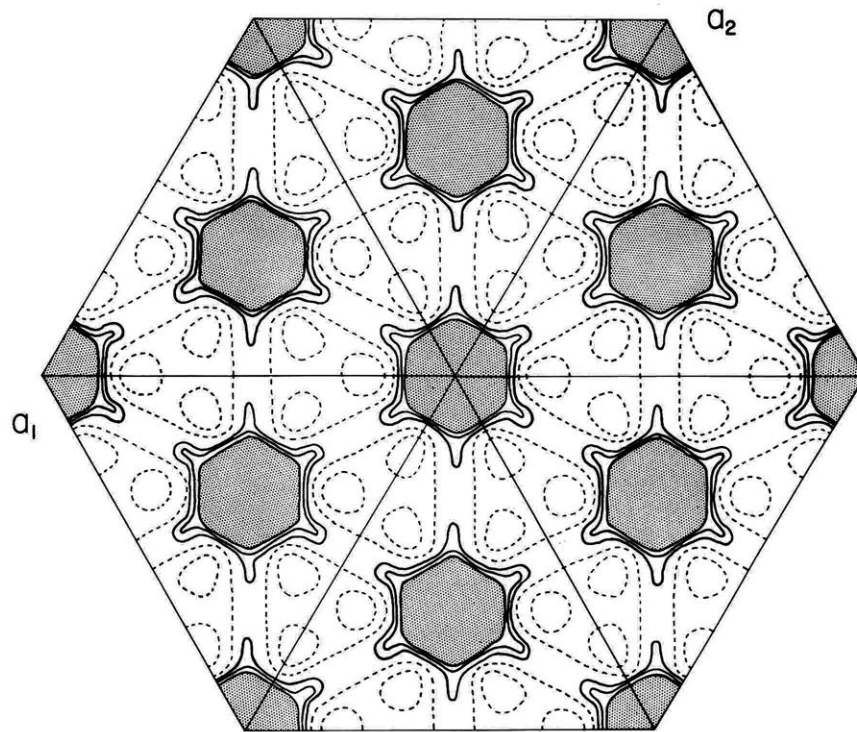
$$I_3(xyo)$$

hexagonal packing (equipoint 2b $00\frac{1}{4}$) or hexagonal close-packing (equipoint 2c $\frac{1}{3}\frac{2}{3}\frac{1}{4}$), and various amounts of Cu in $(0\frac{1}{2}0)$. These syntheses indicated regions of high electron density in positions $(00\frac{1}{4})$ and $(\frac{1}{3}\frac{2}{3}z)$, with $z \approx 0.6$. This arrangement of electron density was meaningful only if S was assigned to $(\frac{1}{3}\frac{2}{3}\frac{1}{4})$, which left $(00\frac{1}{4})$, $(0\frac{1}{2}0)$ and $(\frac{1}{3}\frac{2}{3}z)$ as sites of high Cu density. Subsequent partial Fourier syntheses and difference maps in which Cu was placed in either one or two of these locations invariably indicated electron density in the remaining sites. This arrangement was therefore assumed to be the correct structure.

At this stage, however, the structure was regarded as slightly suspect because of its unorthodox nature. It was felt that a reasonably good agreement between a set of observed and calculated structure factors might possibly be obtained for an incorrect structure if a sufficient number of "disordered" atoms were placed in all the regions of high electron density indicated by Fourier syntheses. To discount this possibility for high-chalcocite, some thirty possible model-structures were tested with Fourier and difference maps. Sulfur atoms in both simple hexagonal packing and hexagonal close-packing were tested. Copper atoms were successively placed in all likely positions. Arrangements in the two acentric space groups permitted by the high-chalcocite diffraction symbol were also tested.

All the models tested yielded high disagreement factors (50 to 65%) which would not decrease upon least-squares refinement. Figure 3.5 presents a typical ortho-hexagonal electron-density section $\rho(0yz)$ and the corresponding difference synthesis section for a model in the acentric space group $P6_3mc$.

The disagreement factor for this arrangement converged to 47%. These maps display two types of anomalies which were commonly encountered in the models which were tested: (1) a peak appears at the end of a vector $-\frac{1}{3}b$ from the heaviest atom in the structure. This is the relative arrangement of S and the greatest fraction of Cu in the structure obtained by implication theory. (2) a deep negative trough

Figure 3.5

Example of anomalies encountered in electron density and difference maps based on an incorrect structure. (Space group $P6_3mc$, S in 2b $\frac{1}{3}\frac{2}{3}\frac{1}{4}$, 1 Cu in 2b $\frac{1}{3}\frac{2}{3}$ .588, $\frac{1}{3}$Cu in 6c .15, .30, .875.) Negative troughs appear in the electron density map which are carried over into the differency synthesis. Also, an anomalous peak occurs at the end of a vector $\frac{1}{3}b$ from the heaviest atom in the structure.

$\rho(oyz)$

$\triangle\rho(oyz)$
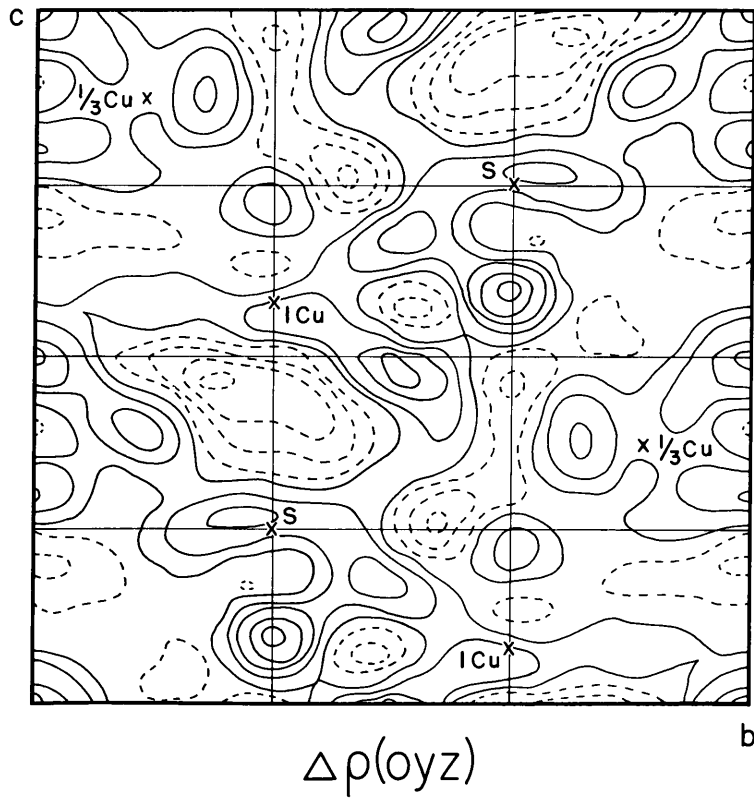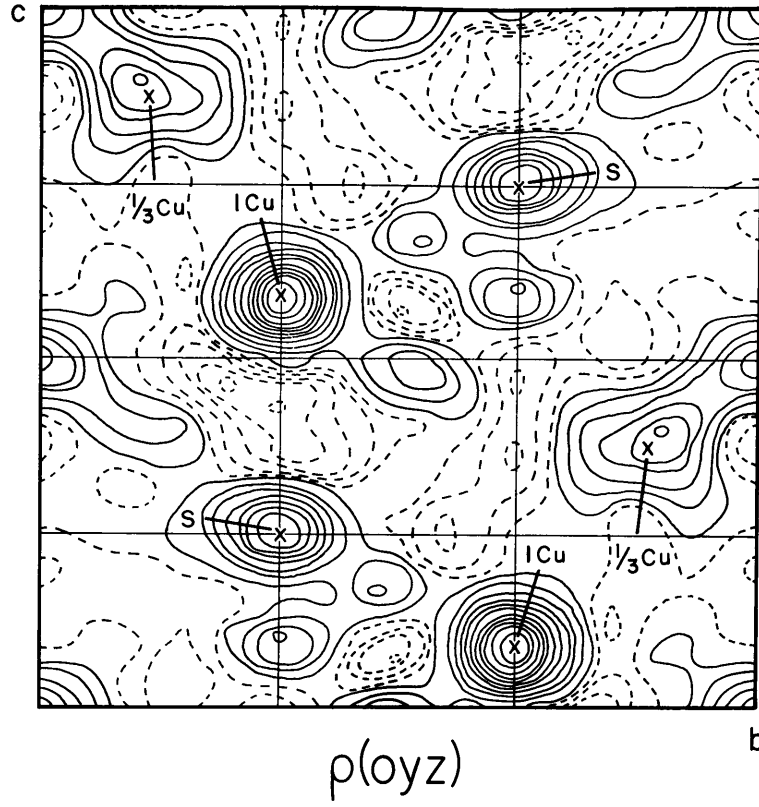
appears in the electron density map. (These regions are not as pronounced in Fig. 3.5 as in most of the maps which were prepared.) This trough is carried over into the difference synthesis. Ordinarily, this would indicate an atom in an incorrect position. No atom, however, was placed in these locations. This uninterpretable anomaly can suggest only that an attempt was being made to fit the observed set of structure factors to an incorrect model.

The disordered structure derived from implication theory was the only model which yielded a relatively low disagreement factor, and no anomalous troughs or spurious Fourier peaks. Accordingly, it was accepted as the correct approximation to the structure.

3.6 Refinement of the High-Chalcocite Structure

Refinement of the disordered high-chalcocite structure was first attempted by least-squares methods. The full-matrix program SFLSQ3 (Prewitt, 1962), written for the IBM 7090 computer, was employed. Copper atom weights for the three types of sites were estimated from the implication diagram I_6 $(\underline{x}\,\underline{y}\,\tfrac{1}{2})$. The initial disagreement factor was 45%. Upon refinement of scale factor, the $\underline{z}$ parameter of the copper atom in $\tfrac{1}{3}\,\tfrac{2}{3}\,\underline{z}$, and the weights of the Cu atoms in the various sites, R decreased to 37%.

Up to this point, no restraint was placed on the weights of the Cu atoms. It was found that there was an extremely large interaction between the scale factor and Cu weights. In some cycles of least-squares refinement, the sum of the distributed copper atoms was as low as three, instead of four per unit cell. In other trials the sum of the copper atoms exceeded four. The discrepancy in Cu weights was balanced by the scale factor. To eliminate this problem, the least squares program was modified so that the shifts in Cu weights during refinement were normalized to keep the sum of the copper weights equal to four copper atoms.

In further cycles of refinement it was noted that the weight of the Cu atom at $00\frac{1}{2}$ tended to increase beyond a weight corresponding to one Cu atom. This does not represent a physically realizable situation. The least-squares program was therefore further modified to keep all Cu weights less than one.

A number of further trials reduced $\underline{R}$ to 32%. The results of these cycles showed, however, that there was a very large interaction between the weights of the Cu atoms and their isotropic temperature factors. The effect of any distribution of Cu atoms in the three sites, within certain limits, was balanced by the least-squares procedure with suitable adjustment of the temperature factor. For variations of Cu weights up to 30%, for example, temperature factors were obtained between -2 and +14. Surprisingly, these wide variations in parameter influenced the disagreement factor by only one or two percent. Continued refinement in which only models with reasonable positive temperature were considered led to the distribution of copper atoms presented in Table 3.3. The disagreement factor for this model is 33.2%.

It was noted that the signs of all structure factors remained unchanged during the cycles of refinement for the models with R below 35%. The electron density maps obtained therefore represented the actual structure. It remained, therefore, to demonstrate this conclusively by improving still further the agreement between the observed and calculated structure factors. The disagreement factor of 33.2% which was obtained for the model given in Table 3.3 could have been improved by employing anisotropic temperature factors. It was apparent from the electron density maps, however, that the distribution of Cu atoms was continuous. That is, "bridges" of appreciable electron density extended between the three types of Cu sites. The large temperature factors assumed by the model of Table 3.3 therefore reflect the fact that Cu distribution is "smeared".

It was clear that any model employing discreet atoms would still represent a crude approximation to the actual structure. Therefore a

Table 3.3

Coordinates, Weights and Temperature factors

for the Discreet Atom Approximation

to the

Disordered High Chalcocite Structure

Atom	Equipoint	Coordinates	Temperature factor
1S	2c	$\frac{1}{3}$ $\frac{2}{3}$ $\frac{1}{4}$	.50
.991 Cu'	2b	0 0 $\frac{1}{4}$	1.19
.404 Cu''	4f	$\frac{1}{3}$ $\frac{2}{3}$ .578	4.09
.067 Cu'''	6g	0 $\frac{1}{2}$ 0	5.51

map of the electron density was synthesized using the set of converged signs. The asymmetric unit was partitioned into 688 volume elements which were represented by a grid given by

$$\underset{\sim}{x}_1 = \frac{1}{30} (\underset{\sim}{a}_1 + \underset{\sim}{a}_2)$$

$$\underset{\sim}{x}_2 = \frac{1}{30} (-\underset{\sim}{a}_1 + \underset{\sim}{a}_2)$$

$$\underset{\sim}{x}_3 = \frac{1}{30} \underset{\sim}{c}$$

A number of electrons proportional to the weight on the electron density map was assigned to each volume element. Of the 688 elements in the asymmetric unit, 350 contained electron density. Structure factor calculations based on this distribution of electrons in the cell were followed by synthesis of electron density and difference maps. Slight reapportionment of the electron density distribution was made on the basis of the difference map. The final disagreement factor was 21.5% based on all data, and 18.0% when unobserved reflections and the 11·0 reflection[1] were excluded. Observed and calculated structure factors are compared in Table 3.4. The orthohexagonal section ($0\underline{y}\underline{z}$), which contains all the maxima in the electron density distribution, is given in Fig. 3.6.

3.7 Description of the High-Chalcocite Structure

The disordered high-chalcocite structure contains sulfur atoms in hexagonal close-packing, and a continuous statistical distribution of copper atoms. There are maxima in the Cu distribution in three

---

[1] This structure factor was too small by a factor of about 2 in all structure factor calculations. While one of the strongest reflections observed on the films, this reflection occurred just at the edge of the blind spot on the first-level photograph. The Lorentz factor consequently was over ten times the value required for the other reflections. A slight misorientation of the crystal could easily account for a 50% error in this structure factor.

Table 3.4

Comparison of Observed and Calculated Structure Factors

for Continuous Electron Density Distribution

(R = 18.0 %)

h k l	F_{obs}	F_{cal}		h k l	F_{obs}	F_{cal}
00.4	11.56	12.12		30.0	6.06	5.39
00.6	9.86	-5.76		30.1	0.83*	-1.10
00.8	3.24	4.21		30.2	6.37	-6.14
10.1	2.06	2.71		30.3	1.89	-0.48
10.2	10.81	-9.49		30.4	3.67	2.23
10.3	14.95	14.87		11.0	5.60	11.55
10.4	2.68	-2.92		11.2	8.48	-9.86
10.5	2.05	0.48		11.4	6.83	5.91
10.6	0.99*	0.49		11.6	6.01	-8.06
10.7	3.40	-3.04		21.0	4.01	-3.51
20.0	2.93	4.29		21.1	3.02	2.29
20.1	5.11	-5.42		21.2	1.79	-1.88
20.2	5.12	4.26		21.3	3.33	-4.14
20.3	5.11	5.58		21.4	0.84*	-0.97
20.4	6.73	8.18		21.5	1.09*	1.91
20.5	1.87	-0.89		21.6	1.00*	0.47
20.6	7.40	6.92		31.0	1.88	-1.16
				31.1	2.60	-1.90
* one-half minimum				31.2	1.26*	0.82
observable value				31.3	0.73*	1.15

Figure 3.6

Orthohexagonal electron density section ρ (0$\underline{yz}$) for high-

chalcocite. F_{000} included, zero contour given as first contour.

All maxima in the Cu distribution lie in this section.
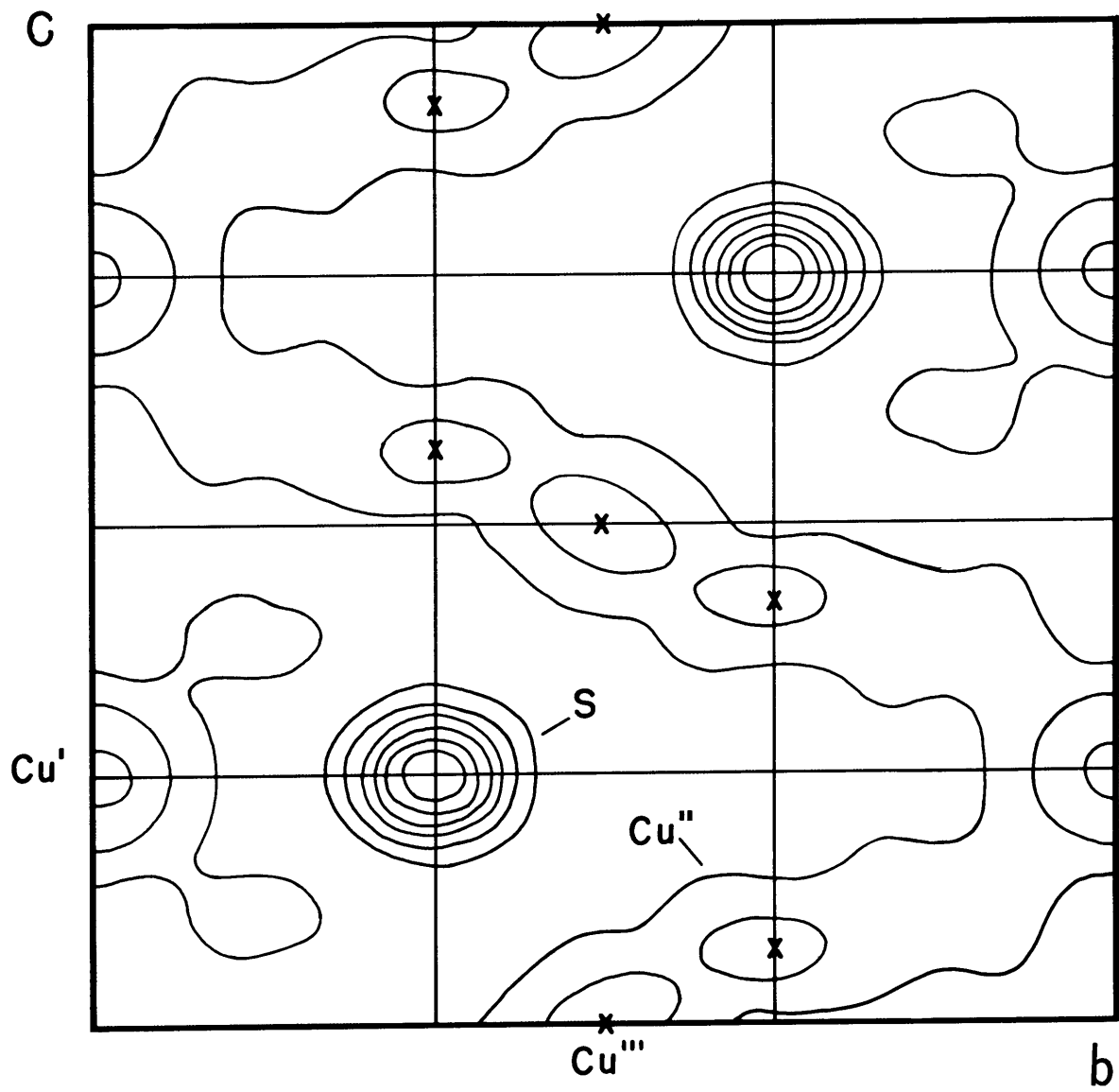
types of sites, and it is convenient to discuss the structure in terms of these Cu locations.

Cu' lies in the S layers forming a trigonal Cu-S sheet. Triangular coordination of Cu was found in tetrahedrite, Section II, and also occurs in the structure of covellite, CuS (Berry, 1954) and stromeyerite, CuAgS (Frueh, 1955). This coordination is unusual for a transition metal and appears to be unique for copper sulfides. Cu''occupies all the available tetrahedral sites. The arrangement of Cu'' and S is equivalent to a wurtzite structure in which the remaining tetrahedral sites are occupied. The remaining Cu''' atoms are located on three edges of the S tetrahedron and link an S atom to the three neighboring S atoms in the adjoining layer. Two-fold coordination of Cu is also found in Cu_2O, with which Cu_2S might be expected to bear some resemblance. This two-fold coordination, as discussed in detail in the following section, is also found for the Ag atom in CuAgS.

The Cu-S bond length for the triangularly coordinated Cu' is 2.28 Å. This is in good agreement with distances of 2.292 and 2.210 Å for the similar group in tetrahedrite, 2.26 and 2.29 Å in stromeyerite and 2.19 Å in covellite. The bond length Cu'''-S is 2.06 Å, which is quite short. A decrease in bond length of about this magnitude should be expected, however, as the coordination number of an atom decreases to two. Cu'' is not located in the center of the S tetrahedron, but has three neighboring S at 2.56 Å and one at 2.21 Å. The bond length for the tetrahedrally coordinated Cu (I) in tetrahedrite was 2.343 Å. Covellite also displays irregular tetrahedral coordination: the tetrahedrally coordinated Cu has three S atoms at 2.30 Å and one at 2.34 Å.

The distance Cu'- Cu'' is 2.56 Å, which is close to the distance 2.556 Å found in metallic copper. Cu'' and Cu''', however, are too close to be occupied simultaneously in an ordered structure. This is consistant with the probable low-chalcocite substructure in which only sites corresponding to Cu' and Cu'' are occupied.

3.8 Relation of Chalcocite to other Copper Sulfide Structures

It is of interest to compare the disordered high-chalcocite structure with that of stromeyerite, $CuAgS$ (Frueh, 1955). This structure is illustrated in Fig. 3.7. The atomic arrangement consists of alternate layers of hexagonal Cu-S rings and close-packed Ag sheets. The mineral is orthorhombic, but is markedly pseudohexagonal, as illustrated by the bond angles indicated in the Cu-S and Ag layers. The Cu-S sheets are stacked in nearly hexagonal close-packing. The Ag layers, however, are displaced along b such that each Ag atom is coordinated by two S atoms in neighboring layers. The sheets are knit together by these zig-zag Ag-S chains.

The relative arrangement of the layers in stromeyerite is perhaps best illustrated by the arrangement of atoms lying in the section (0yz). This is the section which has been previously used to describe the high-chalcocite structure. The section is compared with the corresponding section of the high-chalcocite structure in Fig. 3.8. (The origin of the high-chalcocite structure has been displaced by $\frac{1}{3}b$ to emphasize the similarity between the two structures.) The unit-cell dimensions for the two structures are quite similar, with the exception of the length of the c axis. This difference is in part due to the larger radius of the Ag atom.

It may be seen that the structures differ only in two respects. The Ag atom in stromeyerite links a S atom to only one S atom in the neighboring sheet, while the corresponding Cu''' atom in chalcocite statistically links a S atom to all three S atoms in the neighboring sheet. Secondly, some of the Cu has escaped into the tetrahedral sites. Stromeyerite may consequently be considered a derivative structure of the disordered high-chalcocite arrangement which is formed by ordering the linkage between Cu-S sheets and by relegating the remaining tetrahedral Cu to the Cu-S sheet.

At 93° C stromeyerite undergoes a phase transformation to a hexagonal modification (Djurle, 1958b), in striking similarity to the

Figure 3.7

The crystal structure of stromeyerite, CuAgS.

STROMEYERITE   CuAgS

● Cu   ● Ag   ○ S

124°36'

62°42'
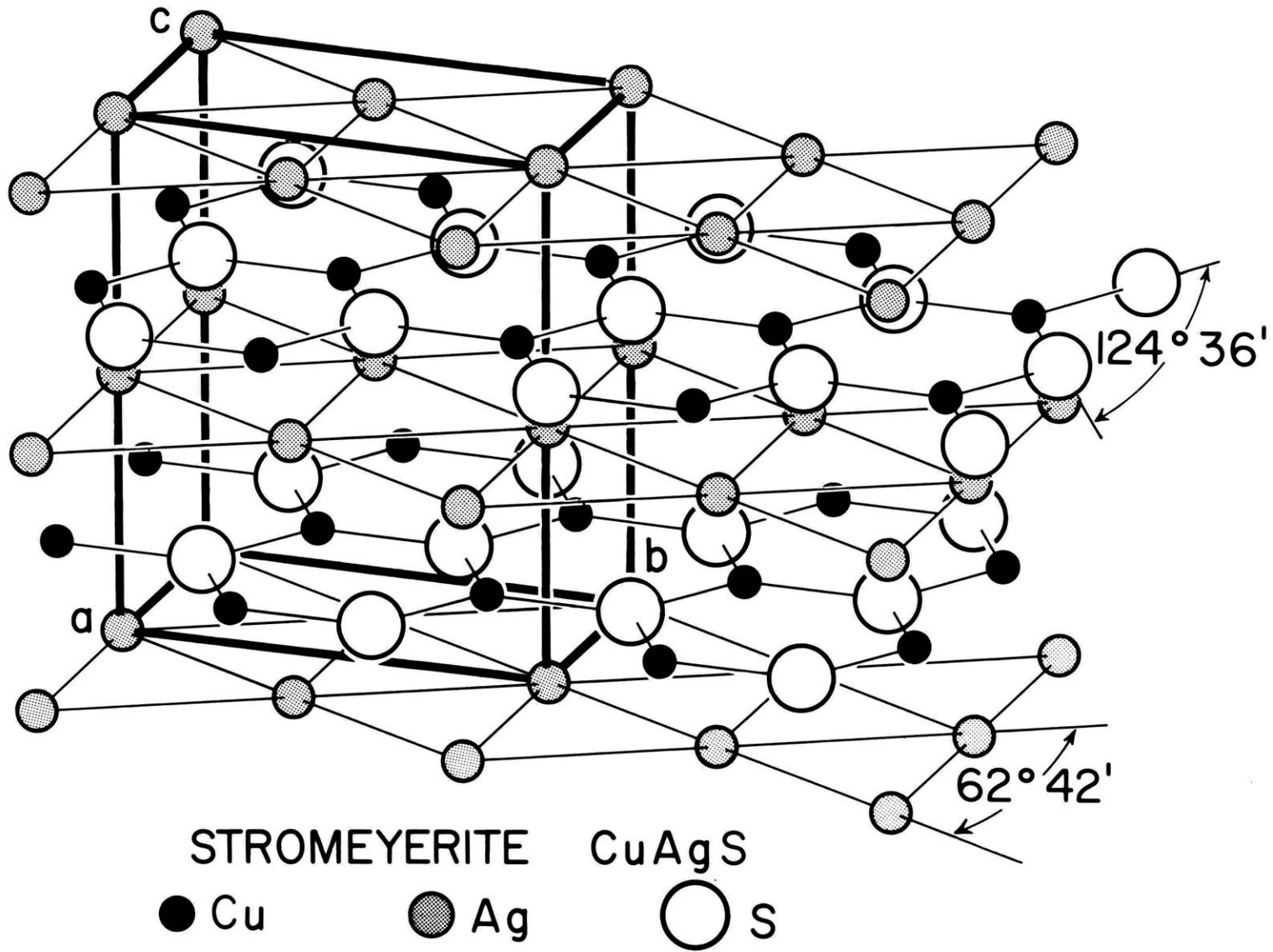
Figure 3.8

Comparison of crystallographic data and electron density sections 0yz for the disordered high-chalcocite structure and stromeyerite.
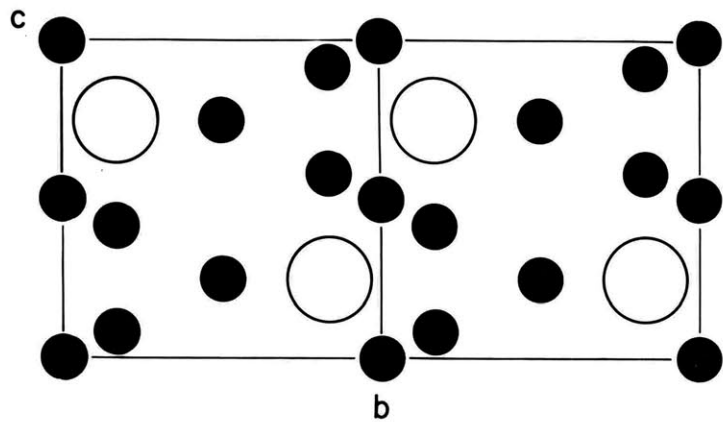
HIGH-CHALCOCITE Cu_2S
a = 3.95
b = 6.84
c = 6.75

Cmcm (orthorhombic   subgroup)
Z = 4
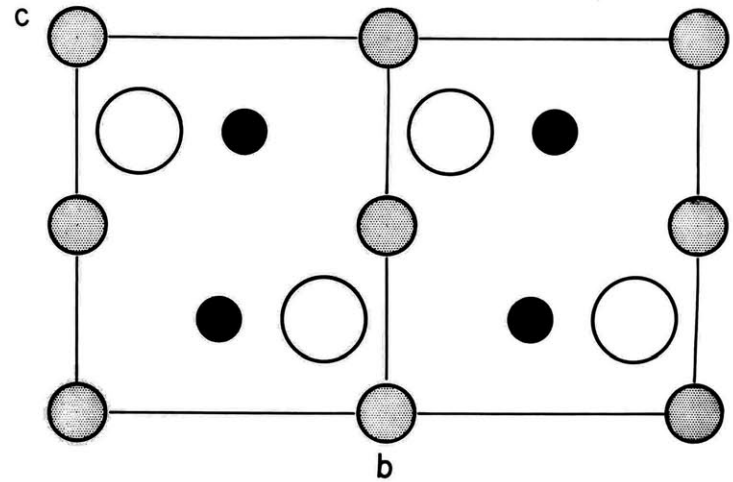
STROMEYERITE   CuAgS
a = 4.06
b = 6.66
c = 7.99

C mcm
Z = 4

transformation in low-chalcocite at 110° C. The structures therefore have similar thermal properties. It seems very likely that the structure of high-stromeyerite will prove to involve disorder of the type found for high-chalcocite.

It is also of interest to compare the low-chalcocite substructure with the structure of covellite, CuS (Berry, 1954). The low-chalcocite substructure has not been investigated in detail. As mentioned in Section 3.3, however, the low-chalcocite substructure Patterson may satisfactorily be interpreted in terms of a structure containing close-packed CuS sheets and Cu in the tetrahedral interstices. The electron density sections $0y\underline{z}$ for covellite and the low-chalcocite substructure are compared in Fig. 3.9. (The origin of the low-chalcocite section has been shifted by $-\frac{1}{3}\underline{b}$, $-\frac{1}{4}\underline{c}$ to emphasize the similarity between the two structures.) It may be seen that the low-chalcocite substructure consists of a curious combination of trigonal and tetrahedral Cu atoms which is similar to that of covellite. A unit cell of the covellite structure may be obtained from the atomic arrangement of the low-chalcocite substructure by joining layers, each consisting of a complete unit cell of low-chalcocite, which have been rotated 180° with respect to one another, and by omitting half of the Cu atoms which occupy tetrahedral sites.

3.9 References

Azaroff, Leonid V. (1954). Crystal settings for upper level photography, precession method. Rev.Sci.Instr.25. 928-929.

Belov, N.V. and Butuzov, V.P. (1946). The structure of high-chalcocite, Cu_2S. Compt.Rend.Acad.Sci.U.R.SS. 54, 717-720.

Berry, L.G. (1954). The crystal structure of covellite, CuS, and klockmannite, CuSe. Am.Mineral.39, 504-509.

Figure 3. 9

Comparison of crystallographic data and orthohexagonal
electron density sections 0yz for covellite and the probable low-
chalcocite substructure.
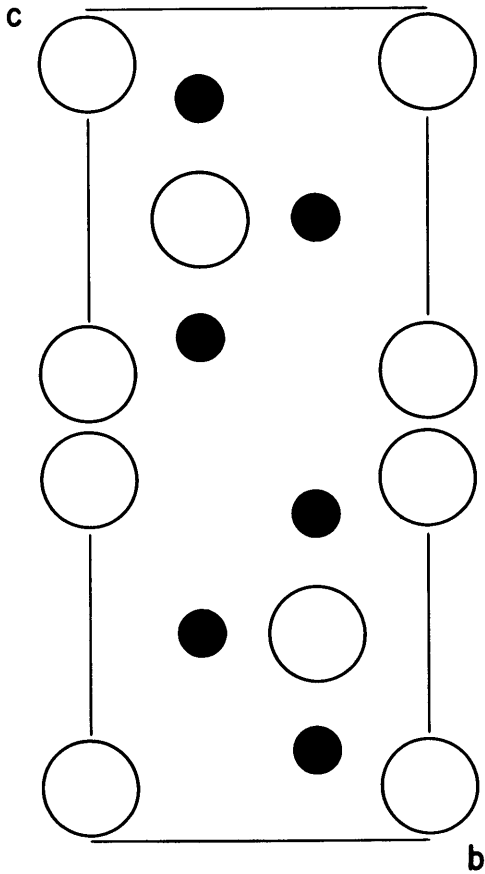
COVELLITE   CuS

a = 3.80
b = 6.58
c = 16.36
Cmcm (orthorhombic subgroup)
Z = 12
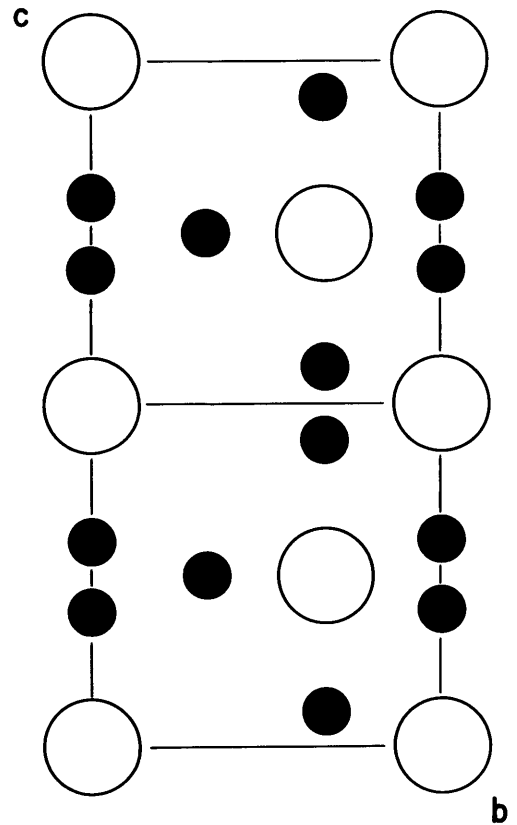
LOW-CHALCOCITE
SUBSTRUCTURE Cu_2S

a = 3.97
b = 6.82
c = 6.71
Cmcm
Z = 4

Bond, W.L. (1951). Making small spheres. Rev.Sci.Instr. 22, 344-345.

Buerger, M.J. (1959). Vector space and its application in crystal-structure investigation. (John Wiley and Sons, New York) 145-167.

Buerger, Martin J. (1960). Crystal-structure analysis. (John Wiley and Sons, New York) 144-146.

Buerger, M.J. and Buerger, Newton W. (1944). Low-chalcocite and high-chalcocite. Am.Mineral. 29, 55-65.

Buerger, Newton W. (1941). The chalcocite problem. Econ.Geol. 36, 19-44.

Buerger, Newton W. (1942). X-ray evidence of the existence of the mineral digenite, Cu_9S_5. Am.Mineral. 27, 712-716.

Djurle, Seved (1958a). An x-ray study on the system Cu-S. Acta Chem.Scand. 12, 1415-1426.

Djurle, Seved (1958b). An x-ray study on the system Ag-Cu-S. Acta Chem.Scand. 12, 1427-1436.

Frueh, Alfred J. (1955). The crystal structure of stromeyerite, AgCuS: A possible defect structure. Z.Krist. 106, 299-307.

Hirahara, Eiji (1947). Experimental studies on the electric conduction and heat capacity of cuprous sulfide semiconductors. J.Phys.Soc.Japan 2, 211-213.

Morimoto, Nobuo (1962). Djurleite, a new copper sulphide mineral. Min.J.Japan 3, 338-344.

Morimoto, N. and England, J.T. (1960). High-temperature Buerger precession camera. Carnegie Institution of Washington Year Book 59, 175 (only).

Posnjak, Eugen; Allen, E.T.; and Merwin, H.E. (1915). The sulphides of copper. Econ.Geol. 10, 491-535.

Roseboom, Eugene H.,Jr. (1962). Djurleite, $Cu_{1.96}S$, a new mineral. Am.Mineral. 47, 1181-1184.

Ueda, Ryuzo (1949). X-ray and thermal studies on the phase transitions of cuprous sulfide Cu_2S. J.Phys.Soc.Japan 4, 287-292.

IV The Superstructure and Twinning of

Pyrrhotite, Fe_7S_8

4.1 Introduction

The iron sulfide minerals found in nature include troilite, FeS; pyrrhotite, having variable composition $Fe_{1-x}S$ with $\underline{x}$ between 0 and approximately 0.2; smythite, Fe_3S_4; and pyrite and marcasite, FeS_2. Near composition FeS the system is extremely complex. These compositions have been studied extensively because of their unusual magnetic properties. Despite numerous investigations, the phase relations and magnetic properties are still not understood in detail.

The voluminous literature on pyrrhotite permits but a brief survey of pertinent work. The general nature of the pyrrhotite structure was determined some while ago by Alsen (1925), who assigned to it the arrangement now known as the NiAs-type (B8) structure. Hägg and Sucksdorff (1933) demonstrated that the compositional variations occurred through omission of Fe from sites normally occupied in the NiAs-type structure. Furthermore, they found that troilite and compounds with Fe deficiencies up to $Fe_{.953}S$ displayed a hexagonal super-structure with $|\underline{a}_1| = |\underline{a}_2| = \sqrt{3}\underline{A}_1$, $\underline{c} = 2\underline{C}$.[1] Following a series of studies of the magnetic properties of artificial Fe-S preparations, Haraldsen (1941) proposed a phase diagram for the system. No phases of symmetry lower than hexagonal were reported, and a superstructure

---

[1] Normal lower case symbols are used to denote the crystallographic axes of the superstructures based on the NiAs-type arrangement, since these are true unit cell translations. The NiAs-type substructure will be denoted by the hexagonal axes $\underline{A}_1$, $\underline{A}_2$, $\underline{C}$ or, where necessary, by the orthohexagonal axes $\underline{A}$, $\underline{B}$, $\underline{C}$ with $|\underline{A}| = \underline{A}_1$, $|\underline{B}| = \sqrt{3}\underline{A}_1$. In the past, most authors have used upper case symbols for the pyrrhotite superstructure.

was again observed only for "paramagnetic" compositions near troilite. The superstructure was found to invert to a NiAs-type structure at $138°C$. Bertaut (1956) subsequently determined the crystal structure of both troilite phases and found that the superstructure was caused by small displacements of Fe atoms normal to c and small displacements of S atoms parallel to c. This structure was confirmed by Andresen (1960) who determined improved atomic coordinates using neutron diffraction. Also, it is now known that troilite is antiferromagnetic, not paramagnetic as previously proposed. At the $138°C$ phase transition the Fe spins shift from an alignment parallel to c to a new antiferromagnetic alignment perpendicular to c. A further transition to a paramagnetic structure occurs at a Neel temperature of $325°C$. The "ferromagnetic" iron-deficient structures probably possess unbalanced antiferromagnetism, i.e. ferrimagnetism.

The structures with higher iron deficiencies are less well understood. As mentioned above, Haraldsen observed no phases with symmetry lower than hexagonal, and no superstructures other than that of the "paramagnetic" troilite. Byström (1945), however, in investigating powder patterns of natural magnetic pyrrhotite from a number of Swedish localities, surprisingly discovered that the majority of these pyrrhotites were monoclinic with $a = B$, $b = A$, $c \approx C$, $\beta = 90.4°$. No superstructures were observed. In a single-crystal x-ray study Buerger (1947) discovered that naturally occurring magnetic pyrrhotites from Morro Velho, Brazil, and Schneeberg, Saxony, exhibited hexagonal superstructures with $a_1 = 2A_1$, $a_2 = 2A_2$, and $c = 4C$. The possible presence of non-space group extinctions in the diffraction patterns, however, indicated that the specimens were perhaps twinned, and that the true symmetry was perhaps monoclinic or orthorhombic. This superstructure was confirmed by Bertaut (1953) on material of an unspecified nature. Twinning of a monoclinic cell was used to explain the non-space group extinctions. Still another type of hexagonal

superstructure, $\underline{a}_1 = 3\underline{A}_1$, $\underline{a}_2 = 3\underline{A}_2$, $\underline{c} = 2\underline{C}$, was reported by Graham (1949) for a synthetic pyrrhotite. The composition was unknown, but was presumably close to troilite since it was "non-magnetic". Erd et al. (1957) discovered naturally occurring Fe_3S_4, smythite, which had a rhombohedral superstructure with $\underline{a}_1 = \underline{A}_1$, $\underline{a}_2 = \underline{A}_2$, $\underline{c} = 6\underline{C}$.

Further work on the Fe-S phase relations has been done by Eliseev and Denisov (1957), and Grønvold and Haraldsen (1952). The latter authors resolved some of these existing contradictions and, in particular, showed that Byström's monoclinic distortion of the NiAs structure did indeed exist for a very narrow range of compositions around Fe_7S_8. This composition was taken as the limit of Fe deficiency, however, and did not extend to Fe_3S_4. Also, superstructures (other than that for troilite compositions) were observed only in the range $Fe_{.971}S$ - $Fe_{.925}S$ where an unidentifiable superstructure was observed in samples prepared at $185^\circ C$.

The superstructures exhibited by the iron-deficient structures are primarily due to ordered arrangement of the iron vacancies. These arrangements have been determined for Fe_7S_8 (Bertaut, 1953), Fe_3S_4 (Erd et al., 1957) and for several defect superstructures in the iron-selenium system where an analogous and equally complex situation exists (Okazaki and Hirakawa, 1956; Okazaki, 1959, 1961). With the exception of Fe_3S_4, where the available crystals were unfortunately of very poor quality, these structures have been determined only through observation of qualitative relations among the superstructure intensities. None have been refined. The proposed pyrrhotite structure (Bertaut, 1953), with which most of the latter structures have been compared, was determined by finding that ordered array of vacancies which was the most favorable energetically.

The present study was intended as an attempt to confirm the arrangement of vacancies in pyrrhotite by a direct structure determination and refinement. In view of the curious physical properties of the

structure, information about atomic displacements around the vacancies and accurate atomic distances would be of great interest. A large number of specimens were examined in a search for crystals suitable for intensity determination. All specimens were found to be twinned. Furthermore it was found that the twin law previously proposed was incorrect. No satisfactory twin law could be deduced. Since the contribution to the superstructure intensities has been assumed to be due to vacancies located at Fe sites in the NiAs-type structure, it was hoped that the structure and twin law could be deduced from Patterson maps based on intensities obtained from the twinned crystal. Frueh (1962) subsequently showed that this approach could indeed be used to solve simple structures for which the twin law was known. Three-dimensional data was collected from a twinned crystal of pyrrhotite, and Patterson projections were synthesized. These projections did not suggest a simple array of vacancies as expected. Rather, it appeared that the superstructure intensities received considerable contribution from displacements of atoms about the vacancies. Detailed analysis of the three-dimensional Patterson functions could perhaps have yielded the structure and twin law. At that time, however, it was learned that workers investigating phase relations in the Fe-S system had apparently succeeded in synthesizing an untwinned specimen of pyrrhotite (J. V. Smith, private communication, 1962), and that this specimen might be made available to the author at a later time. In view of the future availability of a single crystal of pyrrhotite, it seemed fruitless to proceed with analysis of the twinned crystal. The present section is therefore concerned only with the information on the unit cell and twin law which could be inferred from examination of the twinned diffraction patterns.

4.2 Selection and Composition of Crystals

Natural pyrrhotite from Morro Velho, Brazil, was used in the present study. This material (Harvard Catalogue Number 81821) was the same as that previously used by Buerger (1947). Fragments for a single-crystal study were broken from small, well-formed hexagonal platelets and were ground into spheres with the aid of an apparatus similar to that described by Bond (1951). Although care was taken to obtain specimens as free as possible from lineage structure, this effect was still present to some degree even in the best crystals. Polished sections examined in reflected light revealed no evidence for the presence of a second phase even when treated with a variety of etchants.

The composition of the pyrrhotite was determined with the aid of an empirical curve relating $\underline{d}$ for the $10 \cdot 2$ substructure reflection to metal content (Arnold and Reichen, 1962). Powder-diffractometer patterns, obtained using $CuK\alpha$ radiation, showed the $10 \cdot 2$ reflection to be split into two peaks of about equal intensity. (Fig. 4.1$\underline{a}$). As confirmed later, this indicated symmetry lower than hexagonal. The superstructure reflections were undetectable. Following Arnold and Reichen's procedure, the powder was then annealed for 26 hours at $575^{\circ}C$ in a sealed, evacuated Vyror tube. This treatment removed the splitting of the $10 \cdot 2$ reflection, Fig. 4.1$\underline{b}$. The tungsten powder used in the International Union of Crystallography precision lattice parameter project (Parrish, 1962) was used as an internal standard. The resulting hexagonal $\underline{d}_{10 \cdot 2}$ was found to be $2.0632 \pm .0002$ $\overset{o}{A}$, corresponding to $Fe_{.889}S$ (supposedly accurate to $\pm .23$ atomic percent). This composition is exactly Fe_8S_9, although the deviation from the ideal composition, Fe_7S_8, is slight.

4.3 X-ray Investigation

A single-crystal study of an unannealed spherical specimen was made using the precession method. A zero-level precession photograph

Figure 4.1

Powder diffractometer profiles of the 10·2 NiAs-type reflection for Morro Velho pyrrhotite. CuKα radiation. (a) unannealed pyrrhotite. (b) pyrrhotite annealed 26 hours at 575°C. (In comparing the two profiles, note that the 2θ scale for the unannealed specimen is half that for the annealed specimen. The splitting of the pseudo-hexagonal 10·2 peak is thus more pronounced than comparison of the shapes of the two profiles would at first suggest.)

UNANNEALED PYRRHOTITE

(a)
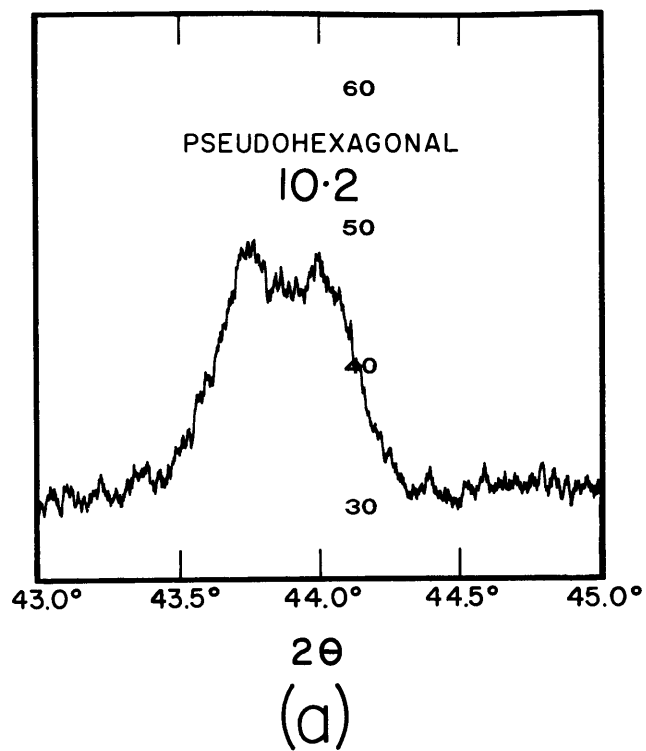
ANNEALED PYRRHOTITE
(26 HRS. AT 575°C)

(b)
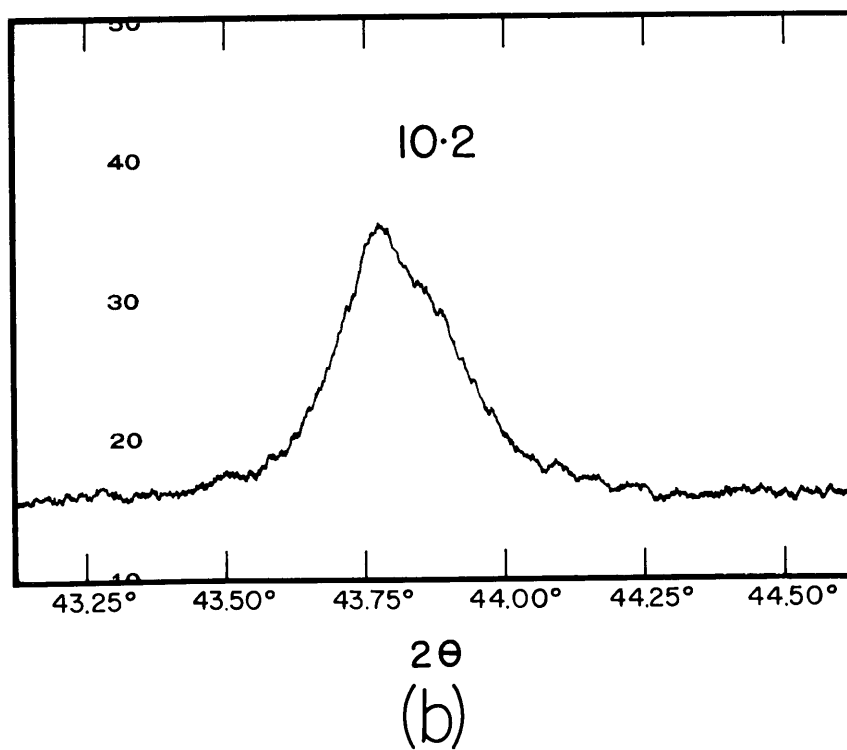
taken about one of the supposedly hexagonal $\underline{a}$ axes is given in Fig. 4.2. The very strong reflections of the NiAs-type substructure are immediately apparent. A large number of weak superstructure reflections may also be observed which, upon first inspection, appear to require doubling of $\underline{A}_1$ and quadrupling of $\underline{C}$. This would require

$$\underline{a}_1 = \underline{a}_2 = 2\underline{A}_1 = 6.88 \text{ Å}$$
$$\underline{c} = 4\underline{C} = 22.81$$

Closer inspection of the reciprocal lattice rows parallel to $\underline{C}$, however, indicates that those rows which do not contain substructure reflections exhibit only superstructure reflections having $\underline{l}$ not equal to $4\underline{n}$. In other words, these reflections occur only in triplets between $\underline{l}$ values corresponding to substructure reflections. This is the non-space group extinction rule previously observed by Buerger (1947) and Bertaut (1953). It was found to hold true for such superstructure reflections on $\underline{all}$ levels (i.e., rows with both $\underline{h}$ and $\underline{k} \neq 2\underline{n}$).

A curious feature of these triplets is illustrated in Fig. 4.3, in which four sets of these spots from the same first level $\underline{a}$-axis precession film have been enlarged and assembled together. If pyrrhotite were hexagonal, this level would display symmetry $2\underline{mm}$ and corresponding spots in the triplets should be equivalent. It may be seen, however, that the intensities do not display this symmetry. In addition, they are not equally spaced, but have very small and unequal displacements parallel to $\underline{C}^*$. The displacements of corresponding spots in the four triplets also bear no symmetric relation to one another. A general reciprocal lattice level for an axis normal to $\underline{C}$ is therefore without symmetry of any kind. Furthermore, the irregular displacement of spots parallel to $\underline{C}^*$ indicates that the superstructure reflections cannot lie on a single reciprocal lattice. This demonstrates conclusively that pyrrhotite is twinned.

Figure 4.2

Precession photograph of pyrrhotite taken about one of the
pseudo-hexagonal a axes/ Zero-level, MoKα, 39 Kv, 15ma, 39 hour
exposure. c* is vertical, a* is horizontal. The strong reflections
correspond to the NiAs-type substructure.
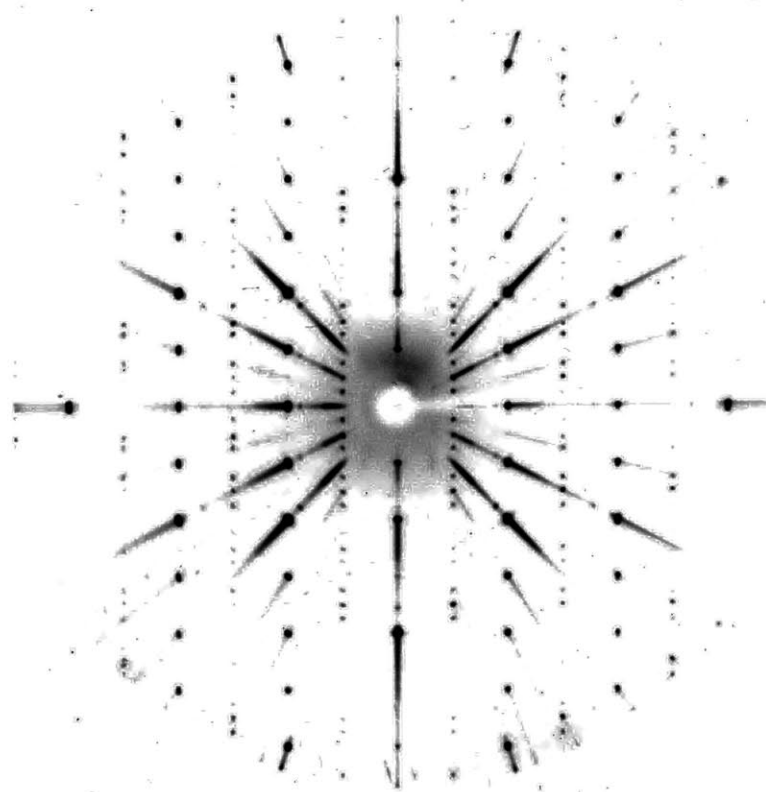
Figure 4. 3

Enlargement of four sets of superstructure "triplets" taken from a single first-level pseudo-hexagonal $\underline{a}$ axis precession photograph. Pseudo-hexagonal indices have been assigned to the reflections. Hexagonal symmetry would require that the triplets be equivalent. The intensities of corresponding reflections bear no symmetric relation. The spots also have small, unequal displacements parallel to $\underline{c}^*$.
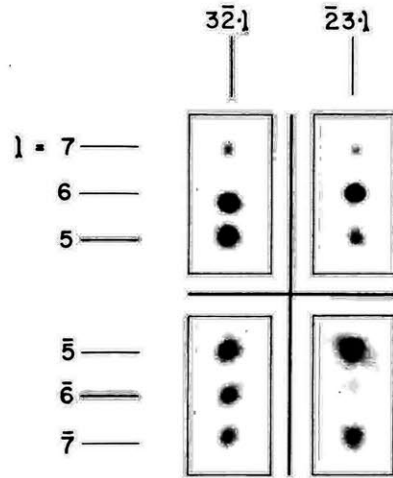
4.4 The Twin Law of Pyrrhotite

Bertaut (1953) postulated that the pyrrhotite twin was composed of two monoclinic crystals related by a 60° rotation about the pseudo-hexagonal $\underline{c}$-axis. A unit cell was proposed with $\underline{a} = 2\underline{B}$, $b = 2\underline{A}$, $\underline{c} \approx 4\underline{C}$, $\beta = 90.45^{\circ}$, and space group $\underline{F}\, 2/\underline{d}$. Figure 4.4 gives views along the pseudo-hexagonal axis for two such reciprocal lattices in this orientation. The slight monoclinic distortions have been neglected. The extinction rules for reciprocal lattice rows parallel to $\underline{C}^*$ are given by the special symbols indicated. Rows containing substructure reflections are represented by solid symbols; rows containing only superstructure reflections are represented by open symbols. Figure 4.4 also presents the resulting composite reciprocal lattice. It may be seen that the $\underline{l} = 4\underline{n}$ extinction rule appears only on two zero levels. Most of those superstructure rows not containing substructure reflections exhibit no extinction rule, whereas the "strange" extinction rule $\underline{l} = 4\underline{n}$ is, in fact, observed for most of these rows. Bertaut's cell and twin law therefore do not explain the unobserved reflections.

Only a single set of NiAs-type substructure reflections are observed in the diffraction patterns. Therefore the twin operation (or operations) must be one which transforms the substructure into itself (or nearly so, if slightly distorted). This situation is common in crystals having substructures, and, indeed, is the physical basis for the twinning. Clearly, no operation isogonal with a hexagonal lattice can give rise to small displacements of the superstructure spots such as those observed, if the superstructure lattice is orthogonal. The true symmetry of pyrrhotite must therefore be monoclinic or triclinic.

Buerger (1960) has shown that the symmetry of a twinned reciprocal lattice is given by the common symmetry of the individuals (when in twinned orientation) augmented by the symmetry of the twin law. If pyrrhotite is monoclinic, a 2-fold axis cannot be oriented

Figure 4.4

The twin law previously proposed for pyrrhotite. A face-centered
monoclinic cell was postulated. Views along $\underline{c}^*$ are given for two
reciprocal lattices related by the twin operation, and the result of super-
imposing the reciprocal lattices is shown. The various extinction
rules are denoted by special symbols.

kb^*

ha^*

60°

kb^*

ha^*

+ =
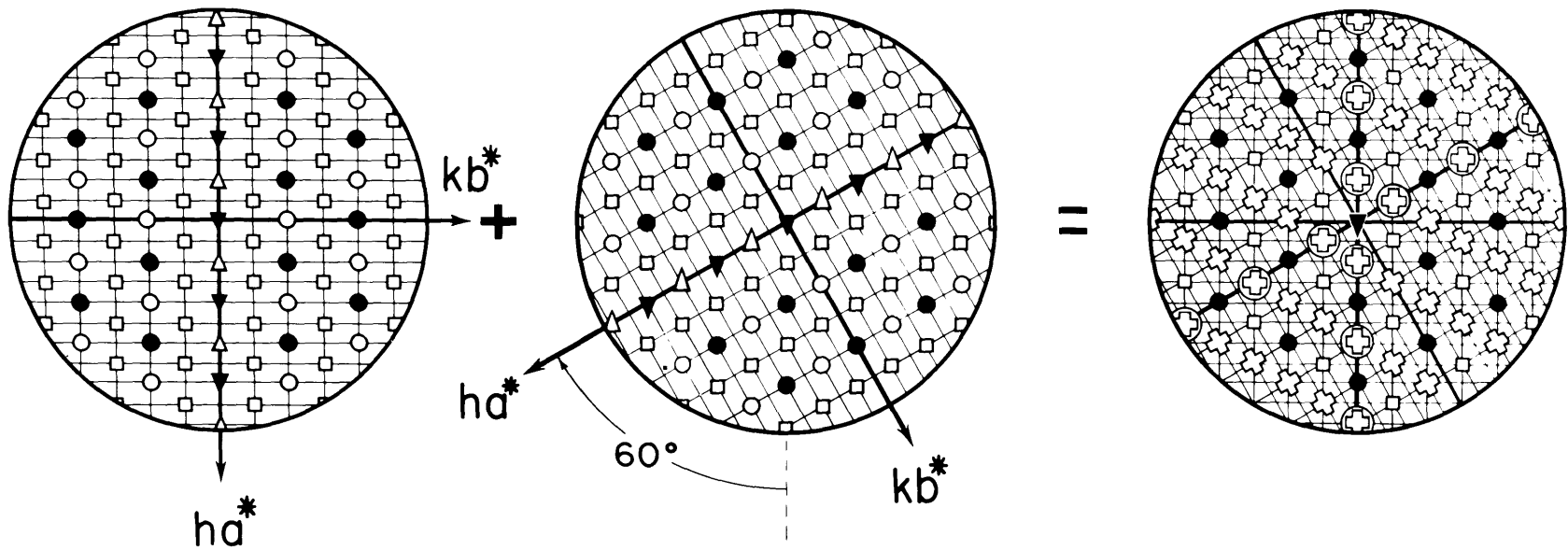
LEGEND FOR OBSERVED REFLECTIONS

● ○ l even

□ l odd

▼ l = 4n

△ l = 4n + 2

✢ all observed

⊕ l = 2n + 1, 2(2n + 1)

(l ≠ 4n)

Solid points represent reciprocal lattice
rows containing NiAs substructure reflections.

parallel to the pseudo-hexagonal $\underline{c}$ axis, since all candidate operations isogonal with a pseudo-hexagonal lattice transform this axis into itself. This would require the twin to exhibit at least 2-fold symmetry about this axis. Diffraction symmetry would then introduce a symmetry plane normal to this axis. This is not observed. The same argument also precludes a plane of symmetry normal to the pseudo-hexagonal axis. Therefore, if a 2-fold axis is present in pyrrhotite it must be normal to the pseudo-hexagonal axis.

To determine the symmetry of the twin, zero- and first-level precession patterns were obtained for all of the pseudo-orthohexagonal $\underline{a}$ and $\underline{b}$ axes. No rotation about the pseudo-hexagonal $\underline{c}$ axis was found which related any two patterns. Figure 4.5, for example, compares one of the triplets of Fig. 4.3 with corresponding sets from films taken at 60, 120 and 180 degree intervals. No equivalence is observed. The previously proposed twin law, however, would require two sets to be equivalent.

Only one operation proved to give identical diffraction patterns. Two sets of pseudo-orthohexagonal $\underline{b}$-axis photographs, for example, were found to be equivalent provided one was rotated 180°. Figure 4.6 compares pairs of reciprocal lattice rows in this orientation which were taken from first-level films in these two directions. The twinning operation therefore consists of a 60° rotation about the pseudo-hexagonal $\underline{c}$ axis, followed by a 2-fold rotation about the pseudo-hexagonal $\underline{b}$ axis. The combination of these two operations is equivalent to a single 2-fold rotation about the pseudo-hexagonal $\underline{a}$-axis midway between the two related $\underline{b}$ axes. One crystal therefore exists for each operation of the twin axis, unlike the previously proposed twin law.

4.5 Orientation of the Twin Axis and Unit Cell

The preceding discussion has described a twinning operation relative to a pseudo-hexagonal lattice. The nature of the true unit cell and the orientation of the twin axis relative to this cell have yet to be

Figure 4.5

Comparison of one of the superstructure reflection triplets of Fig. 4.3 with corresponding sets from precession photographs taken about the neighboring pseudo-hexagonal $\underline{a}$ axis. (Pseudo-hexagonal indices have been assigned to the reflections.)

$3\bar{2}\cdot1$ $21\cdot1$ $\bar{1}3\cdot1$ $\bar{3}2\cdot1$
$(0°)$ $(60°)$ $(120°)$ $(180°)$

$l = 7$

6

5
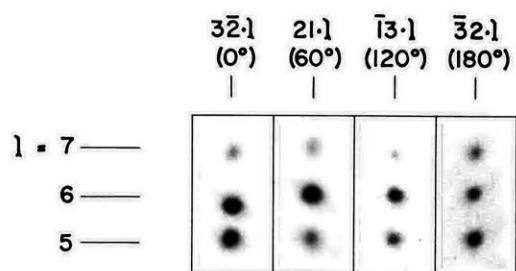
Figure 4.6

Comparison of reciprocal lattice rows related by the twin operation. Rows are compared from precession photographs taken about two first level pseudo-orthohexagonal b axes which are separated by 60°. One of the films has been rotated 180°. These operations are equivalent to a 2-fold rotation about the pseudo-hexagonal a axis between the two axes. (Pseudo-hexagonal indices have been assigned to the reflections.)

$\overline{2}\overline{1}\cdot 1$

$\overline{3}\overline{2}\cdot 1$

$\overline{2}3\cdot 1$

$\overline{3}5\cdot 1$
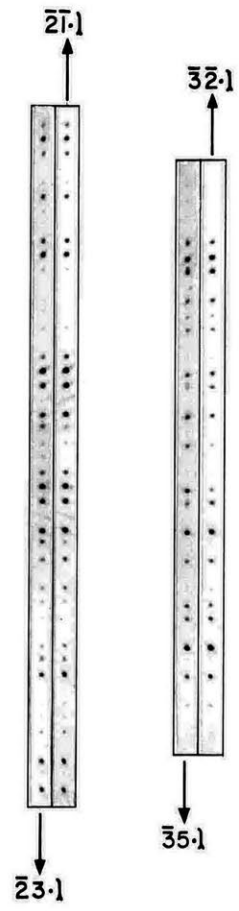
specified. It will now be shown that the displacement of spots which was observed in the precession patterns can arise only if the untwinned lattice is monoclinic.

Let a sublattice of the NiAs-type with true orthohexagonal symmetry be used as a reference system. The diffraction patterns of the twinned crystal indicate apparent doubling of $\underline{A}$ and $\underline{B}$. With the twin operation proposed, this may occur only if the actual $\underline{a}$ and $\underline{b}$ of the individual lattices are double the NiAs-type lattice translations. Assuming that the superstructure is based on a monoclinic distortion of this substructure, two cell geometries not precluded by the previous discussion are possible: the distortion may be such that the projection of $\underline{c}$ on (001) lies along either the orthohexagonal $\underline{A}$ or the orthohexagonal $\underline{B}$ axis of the substructure. The corresponding superstructures for the two possibilities may be expressed by the following general relations:

proj. c parallel to A:

$$\underline{a} = 2\underline{A}$$
$$\underline{b} = 2\underline{B}$$
$$\underline{c} = -\Delta \underline{A} + n\underline{C}$$

proj. c parallel to B:

$$\underline{a} = 2\underline{B}$$
$$\underline{b} = -2\underline{A}$$
$$\underline{c} = -\Delta \underline{B} + n\underline{C}$$

matrix for the transformation

$$\begin{array}{ccc} 2 & 0 & 0 \\ 0 & 2 & 0 \\ -\Delta & 0 & \underline{n} \end{array} \qquad \begin{array}{ccc} 0 & 2 & 0 \\ -2 & 0 & 0 \\ 0 & -\Delta & \underline{n} \end{array}$$

where Δ is a fraction and $\underline{n}$ is an integer. Corresponding matrices for the transformation in reciprocal space are given by the transpose of the inverses of the above matrices. Using this relation one obtains:

proj. c parallel to A:

$$\underline{a}^* = \tfrac{1}{2}\underline{A}^* + \tfrac{1}{2}\frac{\Delta}{n}\underline{C}^*$$
$$\underline{b}^* = \tfrac{1}{2}\underline{B}^*$$
$$\underline{c}^* = \frac{1}{n}\underline{C}^*$$

proj. c parallel to B:

$$\underline{a}^* = \tfrac{1}{2}\underline{B}^* + \tfrac{1}{2}\frac{\Delta}{n}\underline{C}^*$$
$$\underline{b}^* = -\tfrac{1}{2}\underline{A}^*$$
$$\underline{c}^* = \frac{1}{n}\underline{C}^*$$

From these relations it may be seen that $\underline{a}*$ and $\underline{b}*$ are halved in the directions of $\underline{A}*$ and $\underline{B}*$, as is observed. In both possibilities, however, $\underline{a}*$ has an additional component along the hexagonal axis $\underline{C}*$. This is the nature of the displacement of spots which was observed. A triclinic lattice would result in additional components normal to $\underline{C}*$. The pyrrhotite lattice must therefore be at least dimensionally monoclinic.

The two monoclinic possibilities may be distinguished from the nature of the splitting of the pseudohexagonal peaks in the powder pattern described in Section 4.2.[1] It was noted above that the reflection corresponding to the 10·2 reflection of the NiAs-type substructure was split into two components. This behavior requires that proj. $\underline{c}$ be parallel to $\underline{B}$; if proj. $\underline{c}$ were parallel to $\underline{A}$, the peak would be split into three components. The translations of the NiAs-type substructure are known. If it is assumed that $\underline{c}$ is an integral multiple of the pseudohexagonal $\underline{C}$, the value of β may be computed from the magnitude of the splitting of substructure reflections indexed on the basis of the NiAs-type lattice. In this fashion β was found to be $91.79°$.

All possible settings of $\underline{c}$ relative to the twin axis are indistinguishable upon suitable relabeling of the twins or redefinition of the cell. (Proj. $\underline{c}$ cannot, however, be normal to the twin axis, for in this case the twin operation is a symmetry element of the lattice.) The twin operation may therefore be described as a 2-fold rotation about [110].

Even with the information derived above, it is impossible to explain the observed $\underline{l} = 4\underline{n}$ extinction rule. This rule must be explained

---

[1] Splitting of superimposed reflections in the precession photographs was regarded as suspect because lineage structure was present to some degree in even the best crystals. In a powder pattern, however, any splitting must be entirely due to the symmetry of the lattice.

by superposition of lattice rows from each of the crystals comprising the twin. Since this rule is observed on all levels, it must involve space-group extinctions due to the lattice type. The $l = 4n$ extinction rule, however, requires superposition of rows with modulo 4 and modulo 2 extinction rules for l. It is impossible to find a lattice type which predicts absences with both of these periodicities. The lattice type and magnitude of the c translation of pyrrhotite remain undetermined at this time.

Several possible reasons may be advanced to explain this difficulty. The superstructure reflections are extremely weak. The superstructure may be such that reflections with a certain periodicity are too weak to be detectable. Another possibility is that further twinning exists, and that the twin actually consists of two or more crystals in twinned orientation which are then further repeated by a rotation about [110]. All attempts to explain the non-space group extinctions by further twinning were, however, unsuccessful. An additional, but less likely possibility is that the crystals investigated actually consisted of two phases with such similar properties that no intergrowth could be detected. This could perhaps explain the slight deviation of composition from ideal Fe_7S_8.

4.6 The Nature of the Superstructure

A complete set of three-dimensional intensities were collected from a twinned crystal of pyrrhotite. No symmetry was assumed for the twin, and all accessible reflections contained in one hemisphere of reciprocal space were recorded. Some reflections were slightly split due to lineage structure or imperfect superposition of reflections arising from different crystals in the twin. Therefore the intensities were recorded with an integrating precession camera. The effect of splitting of spots was minimized by this technique since all portions of the spot eventually contribute to the "plateau" of the integrated spot as the film is moved through a cycle. An additional advantage provided

by film techniques (and the precession method in particular) for this problem was that all reflections from the crystals comprising the twin could be recorded without detailed knowledge of the magnitude of the distortions from a true orthogonal lattice. This was made possible because, as mentioned above, the small displacements of the reciprocal lattice points have components only parallel to $\underline{C}$. Therefore reflections from the twinned crystal occur on the same level if an axis normal to C* is taken as the precession axis. Details of the procedure used in collecting and measuring the intensities are given in Appendix III.

Patterson projections along the $\underline{a}$ and $\underline{b}$ axes of one of the twins were synthesized using only the superstructure reflections obtained from the twinned crystal. The program ERFR2 written for the I.B.M. 7090 computer was used for these computations. The syntheses employed 119 $0\underline{kl}$ and 79 $\underline{h}0\underline{l}$ superstructure reflections respectively.

If the superstructure were primarily due to ordering of Fe vacancies, a determination of the structure and solution of the twin law would be comparatively simple. The superstructure reflections would have zero intensity if all Fe sites in a NiAs-type arrangement were occupied. If certain sites are vacant, however, the structure factors fail to be equal to zero by an amount equal to the scattering contribution of the missing atoms. The resulting structure factor is therefore the negative of that which would be obtained from the missing atoms alone:

$$F_{\substack{super-\\structure}} = \sum_{\substack{occupied\\sites}} f_{Fe} \exp(-2\pi i \underline{H}\cdot\underline{X}) = -\sum_{\substack{unoccupied\\sites}} f_{Fe}(-2\pi i \underline{H}\cdot\underline{X})$$

Since the superstructure intensities are proportional to F^2, the negative sign on the right of the above expression has no effect. Therefore, if only superstructure reflections are considered, the diffraction effect of an ordered arrangement of vacancies is completely equivalent to a structure in which Fe atoms alone occupy the vacancy sites. The Patterson projections based on the superstructure reflections should

then exhibit maxima only in locations corresponding to certain of the
Fe-Fe interactions of a NiAs arrangement. Consideration of the NiAs
structure shows that, in projection, these peaks may occur only on sub-
nets given by $\underline{a}' = \frac{1}{2}\underline{A}$, $\underline{c}' = \frac{1}{2}\underline{C}$, and $\underline{b}' = \frac{1}{2}\underline{B}$, $\underline{c}' = \frac{1}{2}\underline{C}$, respectively.

The two Patterson projections are presented in Fig. 4.7. F_{000}
has been omitted from the syntheses, and, for clarity, negative regions
have been shaded. Only half of the cell is shown; the remaining half of
the cell is related to the portion shown by inversion centers located at
$0\frac{1}{2}$ and $\frac{1}{2}\frac{1}{2}$. Both the pseudo-orthohexagonal $\underline{a}$ and $\underline{b}$ axes are halved in
projection because the twinned cell assumed is $\underline{C}$-centered. The subnet
on which Fe-Fe interactions should occur for an ideal NiAs-type arrange-
ment is shown as a light net.

Surprisingly, virtually none of the peaks fall on locations corres-
ponding to Fe-Fe interactions. The calculated weight of such inter-
actions is only slightly above the background of the maps. Also, the
observed maxima are not circular, suggesting interactions between
portions of atoms. It therefore appears that the superstructure inten-
sities are primarily due to distortions of the NiAs-type structure about
the vacancies.

Three-dimensional Patterson maps were being synthesized when
the writer learned that J.V.Smith (private communication) had synthe-
sized what appeared to be untwinned pyrrhotite. He offered to supply
the writer with a crystal of this material at a later date. Although the
crystal structure of pyrrhotite could perhaps be solved from the data
obtained in the present study, difficulties would certainly be encountered
in the refinement of the structure because of superimposed reflections.
It was therefore deemed wisest to suspend work on this problem until
the untwinned material became available.

Figure 4.7

Patterson projections for pyrrhotite based on superstructure reflections only. F_{000} omitted; negative regions shaded; contours at equal but arbitrary intervals. Since the pseudo-hexagonal cell is C-centered, $\underline{a}$ and $\underline{b}$ are halved in projection. Inversion centers at $0\frac{1}{2}$ and $\frac{1}{2}\frac{1}{2}$ relate the half of the cell shown to the remaining half. The subnets indicated predice the location of Fe-Fe interactions resulting from a NiAs-type substructure. If the superstructure intensities resulted only from omission of Fe atoms, peaks should occur only at these locations.
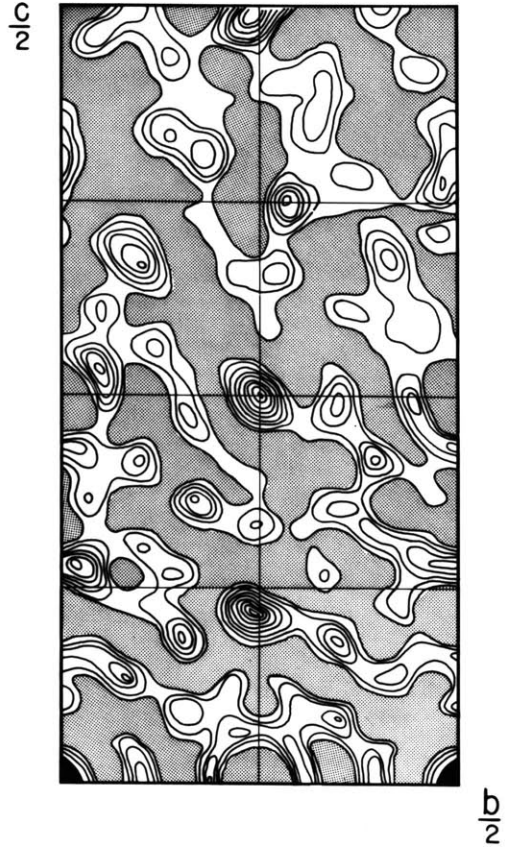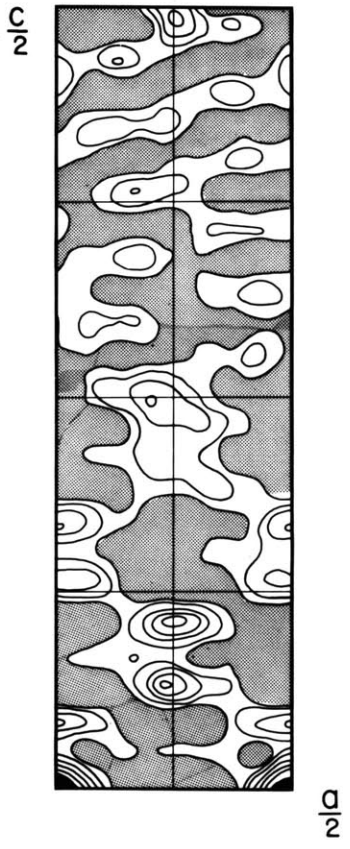
4.7 References

Alsen, Nils (1925), Röntgenographische Untersuchung der Kristallstruck-
turen von Magnetkies, Breithauptite, Pentlandite, Millerite und
verwandten Verbindungen. Geol. Fören. Förhandl. 47, 19-72.

Andresen, Arne F. (1960), Magnetic phase transitions in stoichiometric
FeS studies by means of neutron diffraction. Acta Chem. Scand.
14, 919-926.

Arnold, R.G. and Reichen, Laura E. (1962), Measurement of the metal
content of naturally occurring, metal-deficient, hexagonal
pyrrhotite by an x-ray spacing method. Am. Mineral. 47, 105-111.

Bertaut, E.F. (1953), Contribution a l'etude des structures lacunaires:
La pyrrhotine. Acta Cryst. 6, 557-561.

Bertaut, E.F. (1956), Structure de FeS stoechiometrique. Bull. Soc.
Franc. Mineral. Crist. 79, 276-292.

Bond, W.L. (1951), Making small spheres. Rev. Sci. Inst. 22, 344-345.

Buerger, M.J. (1957), The cell and symmetry of pyrrhotite. Am. Mineral.
32, 411-414.

Buerger, M.J. (1960), Crystal-Structure Analysis. John Wiley and Sons,
New York, 53-67.

Byström, Anders (1945), Monoclinic magnetic pyrites. Ark. Kemi.
Mineral. Geol. 19, 1-8.

Eliseev, E.N. and Denisov, A.P. (1957), X-ray studies of pyrrhotite,
Vestnik Leningrad Univ. 12, No. 18, Ser. Geol. i Geograph., No. 3,
68-78.

Erd, Richard C., Evans, Howard T., and Richter, Donald H. (1957),
Smythite, a new iron sulfide, and associated pyrrhotite from
Indiana. Am. Mineral. 42, 309-333.

Frueh, A.J. (1962), Fourier projections of twinned crystals. Nature
193, 1172.

Graham, A.R. (1949), Artificial pyrrhotite. Am. Mineral. 34, 462-464.

Grønvold, Fredrik and Haraldsen, Haakon (1952), On the phase relations of synthetic and natural pyrrhotites ($Fe_{1-x}S$). Acta.Chem.Scand. 6, 1452-1469.

Hägg, Gunnar, and Sucksdorff, Ingrid (1933), Die Kristallstruktur von Troilite und Magnetkies. Zeit.physik.Chem.B22 , 444-452.

Haraldsen, Haakon (1941), Über die Hochtemperaturumwandlungen der Eisen (11)-Sulfidmischkristalle. Zeit.anorg.chem.246, 195-226.

Okazaki, Atsushi, and Hirakawa, Kinshiro (1956), Structural study of iron selenides FeS_x. I. Ordered arrangement of defects of Fe atoms. J.Phys.Soc.Japan 11, 930-936.

Okazaki, Atsushi (1959), The variation of superstructure in iron selenide, Fe_7Se_8. J.Phys.Soc.Japan 14, 112-113.

Okazaki, Atsushi (1961), The superstructures of iron selenide Fe_7Se_8. J.Phys.Soc.Japan 16, 1162-1170.

Parrish, William (1960), Results of the I.U.Cr.precision lattice-parameter project. Acta Cryst. 13, 838-850.

Section V

X-ray Absorption Corrections for a Crystal of Arbitrary Shape

5.1 Introduction

Many crystal-structure analyses presently being conducted are concerned with obtaining very precise values for atomic positions and temperature factors. This has been made possible to a large extent by improvements in diffraction apparatus and by the availability of high-speed, large-storage electronic computers. Super-refinement obviously requires very accurate data. Routine counter-diffractometer techniques are capable of yielding a set of structure factors with an over-all precision of from 1 to 2 % (see, for example, Appendix I). In order to obtain this degree of reliability, however, it is necessary to apply an accurate absorption correction to the set of diffracted intensities which have been collected.

Determination of an accurate absorption correction is one of the most frustrating problems remaining in crystal-structure determination. In principle it is possible to determine the shape of the crystal to any desired degree of accuracy. This is particularly true if the crystal is bounded by simple forms such as natural plane faces, or a combination of simple shapes such as planes, spheres or cylinders. It follows, then, that it should also be possible, in principle, to determine an absorption correction to any desired degree of accuracy by using any of the several graphical methods which have been proposed. The limit placed on the accuracy of the corrections should ultimately be the accuracy to which the linear absorption coefficient may be computed. Unfortunately, the amount of labor involved in such a procedure is so excessive that this has, until recently, been impossible. The current generation of electronic computers, such as the IBM 709 and 7090, have storage capacities and speeds which make automatic computation of such

corrections feasible.

This section describes a straightforward method for the determination of transmission factors for a crystal of essentially arbitrary shape. The only restriction on the shape of the crystal is that it be describable in terms of a collection of functions which may be expressed analytically. Re-entrant angles are permitted. With but slight modification, the method is applicable to each of the three principal diffraction geometries: the precession, equi-inclination Weissenberg, and Eulerian cradle methods. The procedure is developed in such a manner as to be suitable for programming for high-speed computation. Special versions of such a program have already been written, and, in fact, were employed in Section III. Programming of the general procedure, however, is being done in collaboration with Dr. Charles T. Prewitt. The program will therefore not be described as part of this thesis.

5.2 The Status of the Absorption-Correction Problem

5.2.1 Preparing simple shapes. Previous approaches to the absorption correction problem have been of two types. Corrections for a simple shape, such as a sphere or circular cylinder, are fairly straightforward. The correction depends on but two parameters: the radius of the specimen and the linear absorption coefficient. These corrections may be evaluated as a function of θ and listed, once and for all, in the form of tables. The absorption problem has therefore been solved if the crystal may be ground into one of these simple shapes. Procedures for grinding spheres (Bond, 1951; Revell and Small, 1958) or cylinders (Kersten and Lange, 1932, Pepinsky, 1953; Barbieri and Durand, 1956) have been described. The necessary tables of absorption corrections have been computed for spheres by Evans and Ekstein (1952) and more recently by Bond (1959a). Cylindrical absorption corrections applicable for reflections in a plane normal to the cylinder axis have been evaluated graphically by Claassen (1930) and numerically by Bradley (1935). The latter values have been improved by Taylor and Sinclair (1945) and more

recently by Bond (1959b). Buerger and Niizeki (1958) have shown how these tables may be applied to upper-level reflections obtained with equi-inclination geometry. An analytical method for the determination of absorption corrections for ellipsoidal crystals has recently been given by Fitzwater (1961). The expression for the transmission factor was expanded in terms of definite integrals. The convergence of the series, however, was quite poor for $\mu r > 1$. Unfortunately, it is values of μr beyond this range which present very serious absorption problems, and for which an accurate correction would be desired.

It is not always possible to grind a crystal into a simple shape such as a sphere or cylinder. Crystals with very anisotropic hardnesses may assume ellipsoidal shapes. Very sectile crystals may be deformed to the extent of being rendered useless. Crystals with very perfect cleavages present similar problems. Furthermore, a certain amount of risk is always attendant in these grinding processes, since very small crystals are easily lost in the procedure. One therefore might be reluctant to apply them to rare crystals of limited availability.

5.2.2 Prismatic Absorption Corrections. A second group of methods has been concerned with absorption corrections for crystal shapes which present a constant cross-sectional area to the x-ray beam (i.e., prismatic shapes). The approach to this problem has been to develop convenient devices which permit transformation of the double integral of the transmission factor into a summation which may be evaluated graphically. Basic methods have been proposed by Hendershot (1937) and Albrecht (1939). These methods have been developed and modified by Howells (1950), Evans (1952), Grdenic (1952), Joel et al. (1953) and Rogers and Moffett (1956). These methods are all extremely tedious to apply. Furthermore, as has been noted, they apply only to prismatic shapes. It is difficult to apply them to upper-level reflections except in the case of equi-inclination geometry. They also represent approximations in that they neglect any effect caused by the forms

bounding the ends of the prism. Burnham (1961) has shown that appreciable error may result unless the crystal has a sufficiently large length to diameter ratio.

A first application of high-speed computation to the evaluation of transmission factors was made by Busing and Levy (1957). Their method employed the Gaussian quadrative method of numerical integration in evaluating transmission factors for a crystal bounded by plane faces. No re-entrant angles were permitted, and the method was applicable only to zero level reflections in the equi-inclination method. Burnham (1961) subsequently extended this method to include treatment of upper level reflections for equi-inclination geometry. A program employing this method has been written by Burnham for the IBM 7090 computer. This program has been in use in this laboratory for two years. It is quite efficient and, as far as equi-inclination geometry is concerned, is general in that curved surfaces may be approximated by a series of plane faces.

The method described in this section differs slightly from Burnham's procedure. It will provide equivalent results for the equi-inclination method except that (1) a slight advantage in speed and accuracy will be gained since quadratic forms such as cylinders and ellipsoids may be specified by a single function instead of being approximated by a series of planes, and (2) it is more general in that crystals with re-entrant angles may be treated. Unlike the Burnham method, the present procedure has also been extended to include the precession and Eulerian cradle geometries.

5.3 The General Nature of the Method

In the present method the crystal shape is specified by a combination of quadratic functions. This type of function is general enough to describe a large variety of shapes. These functions are specified in some natural coordinate system relative to the principal crystal shape. For example, if the crystal consists of an ellipsoid modified by a few

planes, the coordinate system is taken along the principal axes of the ellipsoid. This coordinate system has the advantage that the equation of the principal form is easily specified, and furthermore, assures selection of a system of volume elements which is evenly distributed with respect to the overall shape of the crystal.

The crystal is then subdivided into a selected number of volume elements. These elements are represented by a grid established as submultiples of the maximum dimensions of the crystal. Each grid point is then tested to determine whether or not it lies within the crystal. Those grid points lying outside of the crystal are discarded at this point. Crystals with re-entrant angles will require a special procedure for testing the grid points.

This natural coordinate system is next transformed to a coordinate system relative to the diffractometer (when all instrumental settings are at zero). This "orientation transformation" is used to transform the equations of all functions bounding the crystal, and also the coordinates of all retained grid points into the coordinate system of the diffractometer. All computations up to this point need be performed only once for each problem.

Next, the "diffraction transformation" is established for each of three diffraction geometries. This transformation is the operation, relative to the diffractometer axes, which is necessary to bring the crystal into the position in which a reflection is generated. The diffraction transformation will be determined in terms of the indices of the reflection and reciprocal cell dimensions for a triclinic cell. Performing the operation on the crystal itself would require a separate transformation of all grid point coordinates, and also transformation of the equations for all bounding functions. This procedure would have to be repeated for each reflection. Instead, the inverse of this transformation will be imployed. The crystal (and thus the reciprocal lattice) will be regarded as stationary, and the inverse transformation will be applied to the vectors representing the directions of the incident and diffracted beams.

In this fashion a unit vector in the directions of the incident and diffracted beams may be established relative to the crystal for a given reflection. The form of these expressions is the only manner in which the procedure differs for the various diffraction geometries.

To evaluate a transmission factor, it remains to determine the distance in the direction of the incident beam from the surface of the crystal to each grid point, and the distance in the direction of the diffracted beam from the grid point to the surface. To obtain these distances, appropriate scalar multiples of each beam vector are sought such that the terminal point of vectors from the grid point satisfies the equation for a particular bounding function. This leads to a quadratic equation for the desired distances, which must be solved for each bounding function. Again, a crystal shape with re-entrant angles requires a special treatment in order to eliminate portions of beam paths which lie outside the crystal. The transmission factor for the particular reflection is given by the average of the transmission factors for the separate grid points.

5.4 Specification of Bounding Functions

The crystal shape will be assumed to be representable by a collection of one or more functions which will be called bounding functions. It will be assumed that the quadratic form

$$f(x'y'z') = A'x'^2 + B'y'^2 + C'z'^2 + D'x'y' + E'y'z' + G'z'x'$$

$$+ H'x' + I'y' + J'z' \equiv F \tag{5.1}$$

is general enough to permit a variety of shapes sufficient to describe portions of even an irregular crystal. In equation (5.1) the symbols A, B, C, D, E, G, H, I, K, and F are constants. Table 5.1 lists a number of geometric shapes which can be described by a function of this form. The canonical form of the shape is presented, and then this expression is expanded to obtain values for the coefficients of (5.1). The origin of the surfaces has been placed at a general location $\underline{p}$, $\underline{q}$, $\underline{r}$ relative

Table 5.1

Geometric Shapes Which May Be Expressed as a Quadratic Function

Geometric Shape	Canonical form of equation of surface	Values of coefficients in general quadratic form $f(xyz) = A'x'^2 + B'y'^2 + C'z'^2 + D'x'y' + E'y'z'$ $\dotplus\, G'z'x' + H'x' + I'y' + J'z' \equiv F'$					
		A'	B'	C'	D'	E'	G'
Plane	$\dfrac{x'}{a} + \dfrac{y'}{b} + \dfrac{z'}{c} = 1$	0	0	0	0	0	0
Elliptic cylinder	$\dfrac{(x'-p)^2}{a^2} + \dfrac{(y'-q)^2}{b^2} = 1$	$1/a^2$	$1/b^2$	0	0	0	0
Elliptic paraboloid	$\dfrac{(x'-p)^2}{a^2} + \dfrac{(y'-q)^2}{b^2} = c(z'-r)$	$1/a^2$	$1/b^2$	0	0	0	0
Hyperbolic paraboloid	$\dfrac{(x'-p)^2}{a^2} - \dfrac{(y'-q)^2}{b^2} = c(z'-r)$	$1/a^2$	$-1/b^2$	0	0	0	0
Ellipsoid	$\dfrac{(x'-p)^2}{a^2} + \dfrac{(y'-q)^2}{b^2} + \dfrac{(z'-r)^2}{c^2} = 1$	$1/a^2$	$1/b^2$	$1/c^2$	0	0	0
Elliptic cone	$\dfrac{(x'-p)^2}{a^2} + \dfrac{(y'-q)^2}{b^2} - \dfrac{(z'-r)^2}{c^2} = 0$	$1/a^2$	$1/b^2$	$-1/c^2$	0	0	0
Hyperboloid of one sheet	$\dfrac{(x'-p)^2}{a^2} + \dfrac{(y'-q)^2}{b^2} - \dfrac{(z'-r)^2}{c^2} = 1$	$1/a^2$	$1/b^2$	$1/c^2$	0	0	0

Table 5.1 (continued)

Geometric Shapes Which May Be Expressed as a Quadratic Function

Geometric Shape	Value of coefficients in general quadratic form (continued)			
	H'	I'	J'	F'
Plane	$1/a$	$1/b$	$1/c$	1
Elliptic cylinder	$-2p/a^2$	$-2q/b^2$	0	$1 - p^2/a^2 - q^2/b^2$
Elliptic paraboloid	$-2p/a^2$	$-2q/b^2$	$-c$	$- p^2/a^2 - q^2/b^2 - cr$
Hyperbolic paraboloid	$-2p/a^2$	$+2q/b^2$	$-c$	$- p^2/a^2 + q^2/b^2 - cr$
Ellipsoid	$-2p/a^2$	$-2q/b^2$	$-2r/c^2$	$1 - p^2/a^2 - q^2/b^2 - r^2/c^2$
Elliptic cone	$-2p/a^2$	$-2q/b^2$	$+2r/c^2$	$- p^2/a^2 - q^2/b^2 + r^2/c^2$
Hyperboloid of one sheet	$-2p/a^2$	$-2q/b^2$	$-2r/c^2$	$1 - p^2/a^2 - q^2/b^2 + r^2/c^2$

to the origin of the coordinate system. It should be noted that a circular cylinder represents a special case of an elliptic cylinder with $\underline{a} = \underline{b}$. Similarly, a sphere or circular cone represents a special case of an ellipsoid or elliptic cone with $\underline{a} = \underline{b} = \underline{c}$.

Some precautions must be observed in employing certain of these shapes. The hyperboloid of one sheet and the hyperbolic paraboloid have surfaces which are concave outwards. These shapes therefore involve one of the problems associated with re-entrant angles and must be given the special treatment described in Section 5.10. The expression for the elliptic cone specifies two surfaces which, for the form of the expression given in Table 5.1, occur for $\underline{z} \leq \underline{r}$ and $\underline{z} \geq \underline{r}$. Since both surfaces ordinarily would not be used in describing a crystal shape, an artificial bounding plane specified by $\underline{z} = \underline{r}$ should be used to eliminate the unwanted portion of the surface. If the vertex of the cone happens to be modified by a second function for the particular crystal shape encountered, this procedure is, of course, unnecessary.

It is convenient to distinguish between two types of crystal shapes. The first class of shapes may be described in terms of unlimited bounding functions. The various forms of this class of crystal are such that any point lying within the volume of the crystal lies within all bounding functions. An example of this type of crystal is given in Fig. 5.1 $\underline{a}$. A second class of shapes must be specified in terms of limited bounding functions. In this class of shapes, a given function may bound the crystal until it intersects another bounding function. Beyond this second function, a different function bounds the crystal. An example of a crystal with this type of shape is given in Fig. 5.1 $\underline{b}$. The crystal is bounded by the function $\underline{f}_4$ until $\underline{f}_2$ is reached. The crystal is then bounded by $\underline{f}_5$. Crystal shapes having limited bounding functions exhibit re-entrant angles.

It is also convenient to subdivide crystals with limited bounding functions into two cases. In case I, illustrated by Fig. 5.1 $\underline{b}$, the bounding function or functions which specify the limits of applicability

Figure 5.1

Classification of crystal shapes according to the nature of the bounding functions.

(a) UNLIMITED BOUNDING FUNCTIONS
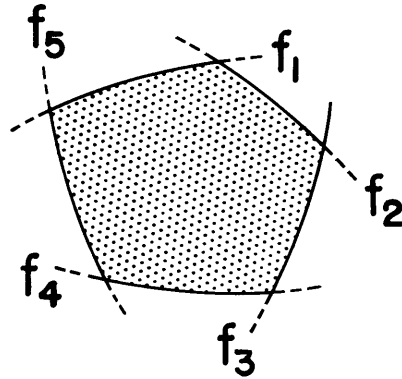
(b) LIMITED BOUNDING FUNCTIONS (CASE I)
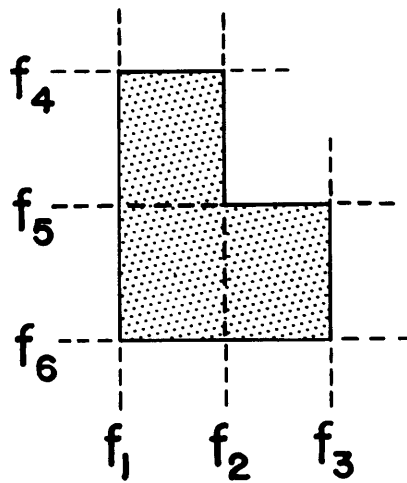
(c) LIMITED BOUNDING FUNCTIONS (CASE II)
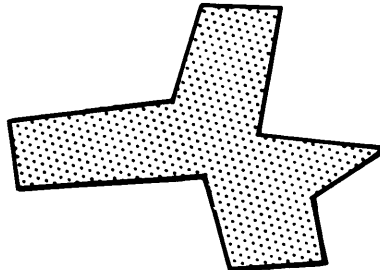
of other functions divide the crystal into sub-volumes which may, by themselves, be considered as bounded by unlimited bounding functions. Thus, in Fig. 5.1 b, for example, the crystal may be considered as two subvolumes defined by the sets of unlimited bounding functions f_{-1}, f_{-2}, f_{-4} and f_{-6}; and f_{-2}, f_{-3}, f_{-5}, f_{-6}. This is a special situation which does not obtain in Fig. 5.1 c. This crystal shape, case II, does not have limited bounding functions which subdivide the crystal volume.

It should be pointed out that consideration of crystals with limited bounding functions does not present a situation which is purely academic. Crystal shapes similar to Fig. 5.1 b might be encountered, for example, in prismatic cleavage fragments from which a small splinter is missing. The general case, Fig. 5.1 c, might represent a dendritic crystal. Ordinarily, one would discard these specimens in favor of a simpler shape. As pointed out in section 5.2.1, however, it may be neither desirable nor possible to do this if the specimen is rare.

5.5 Establishment of Volume Elements

Let the natural coordinate of the crystal be specified by a Cartesian coordinate system x', y', z'. As mentioned above, this coordinate system is established relative to the predominant form of the crystal. The equation of the predominant shape of the crystal is therefore specified in canonical form. Let the limits of the crystal be defined by a "box", such that all points within the crystal satisfy the conditions:

$$-u \leq x' \leq +u$$
$$-v \leq y' \leq +v \qquad (5.2)$$
$$-w \leq z' \leq +w .$$

The dimensions of the box, $2u$, $2v$, $2w$, are now subdivided into a desired number of intervals, N. For reasons which will become apparent later, it is convenient to restrict N to even integers.

The collection of volume elements will be represented by an array of grid points. Each grid point is located at the center of a volume element, Fig. 5.2. The coordinates of these grid points are therefore specified by

$$x'_{l'} = \frac{l'}{2} \frac{u}{N} \quad (l' = -\frac{N}{2}, -\frac{N}{2}+1, \ldots -1, +1, \ldots \frac{N}{2})$$

$$y'_{m'} = \frac{m'}{2} \frac{v}{N} \quad (m' = -\frac{N}{2}, \ldots \ldots \ldots \ldots \ldots \frac{N}{2}) \quad (5.3)$$

$$z'_{n'} = \frac{n'}{2} \frac{w}{N} \quad (n' = -\frac{N}{2}, \ldots \ldots \ldots \ldots \ldots \frac{N}{2})$$

In applying the method to high-speed computation, it is easier to store the array of subscripted variables $x'_{l'}$, $y'_{m'}$, $z'_{n'}$ if the integers l', m', n' are restricted to non-zero, positive integers. Accordingly, it is convenient to replace the subscripts l', m', n' by a new set l, m, n, such that:

$$x'_{l} = [-u - \frac{u}{N} + l(2u/N)] \quad (l = 1, 2, 3 \ldots N)$$

$$y'_{m} = [-v - \frac{v}{N} + m(2v/N)] \quad (m = 1, 2, 3 \ldots N) \quad (5.4)$$

$$z'_{n} = [-w - \frac{w}{N} + n(2w/N)] \quad (n = 1, 2, 3 \ldots N)$$

It will be shown later that only half the volume elements need be considered if the crystal shape is centrosymmetric. It may be seen that by restricting N to even integers, no grid points occur on the lines $x = 0$, $y = 0$, $z = 0$. This affords the advantage that a centrosymmetric equivalent exists for each grid point. If the grid points were not defined in this fashion, weights would have to be assigned to certain grid points in evaluating the transmission factor for a centrosymmetric crystal.

Figure 5.2

Establishment of volume elements and representative array of grid points.

ARRAY OF GRID POINTS

VOLUME ELEMENTS

$\ell' =$ -3   -2   -1   1   2   3

$\ell =$ 1   2   3   4   5   6

x=-u

x=+u
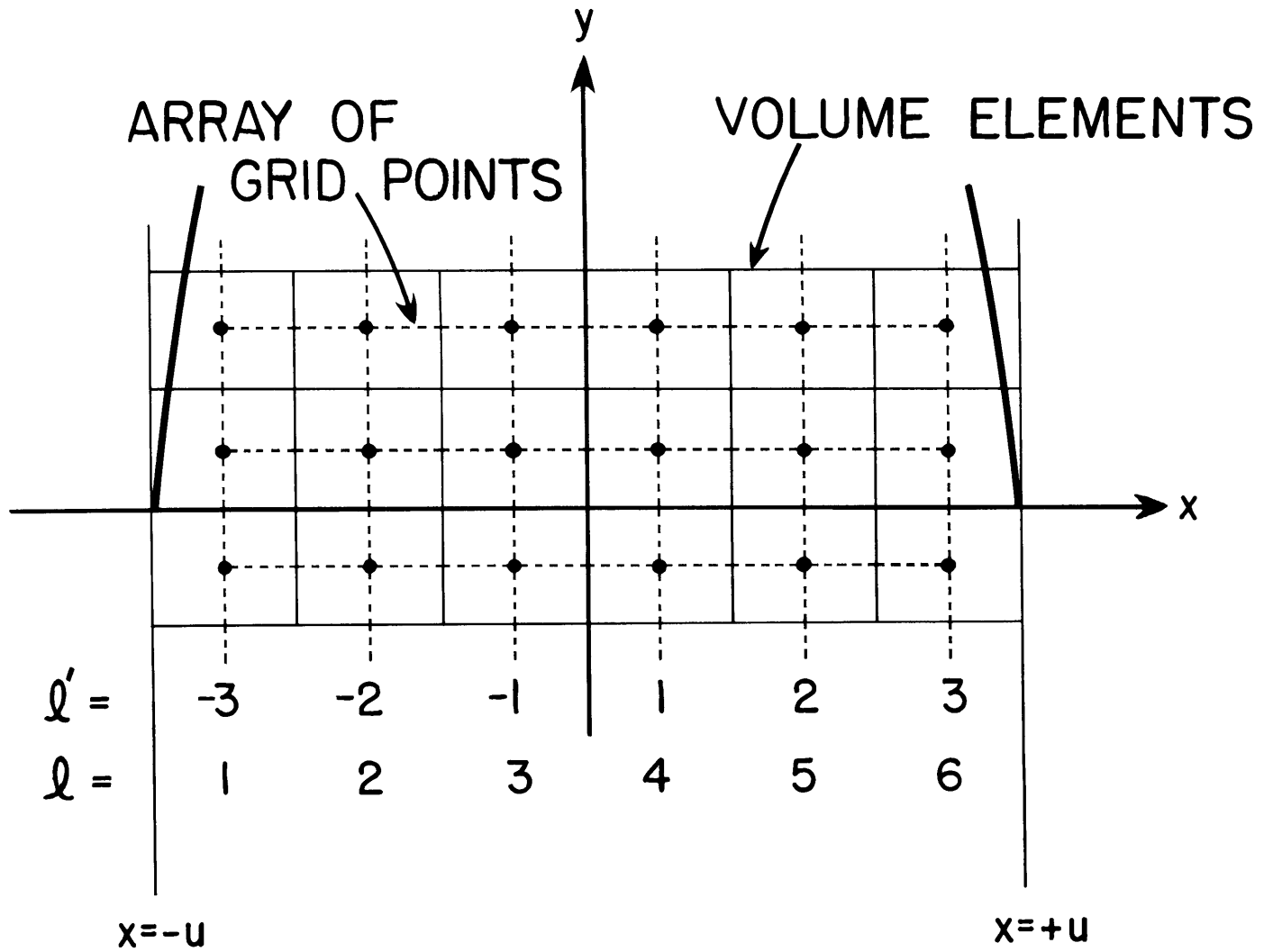
5.6 Testing of Grid Points

5.6.1 Unlimited Bounding Functions.

The "box" enclosing the crystal has now been subdivided into $\underline{N}^3$ volume elements represented by $\underline{N}^3$ grid points. Some of these grid points are contained with the crystal, others are not. It is now necessary to test each grid point so that grid points lying outside the crystal may be discarded.

A collection of functions $\underline{f}_1(\underline{xyz}) = \underline{F}_1$, $\underline{f}_2(\underline{xyz}) = \underline{F}_2$, $\underline{f}_3(\underline{xyz}) = \underline{F}_3 \ldots$ has been specified which describes the surface of the crystal. $\underline{F}_1$, $\underline{F}_2 \ldots$ represent constants. If the value of $\underline{f}_i(\underline{x}_l \underline{y}_m \underline{z}_n)$ for a particular grid point is less than the constant $\underline{F}_i$, then the grid point lies within the surface defined by that function. If, on the other hand, $\underline{f}_i(\underline{x}_l \underline{y}_m \underline{z}_n)$ is greater than $\underline{F}_i$, the grid point lies outside the surface of that function.

The shape of crystals with unlimited bounding functions is such that, by definition, any point within the crystal lies simultaneously within all the bounding functions. Therefore, any of the grid points, defined by 5.4, which lie within the crystal must simultaneously satisfy the conditions

$$f_1(x_l y_m z_n) < F_1$$

$$f_2(x_l y_m z_n) < F_2$$

$$\vdots \qquad \qquad \vdots$$

$$f_i(x_l y_m z_n) < F_i \quad .$$

(5.5)

Any grid point not satisfying all these conditions is rejected.

5.6.2 Limited Bounding Functions (Case I).

When the limiting bounding function divides the crystal into two or more subvolumes, as in Fig. 5.1 b, the grid point is first tested to determine the subvolume in which it occurs. The bounding functions relevant to that subvolume may then be considered as unlimited bounding functions. Thus in Fig. 5.1 b, for example, the testing procedure would be:[1]

---

[1] The origin has been assumed to be between F_1 and F_2.

if $f_2(x_l\,y_m\,z_n) < F_2$, then

$$f_1\,(x_l\,y_m\,z_n) < F_1$$

$$f_4\,(x_l\,y_m\,z_n) < F_4$$

$$f_6\,(x_l\,y_m\,z_n) < F_6$$

if $f_2(x_l\,y_m\,z_n) > F_2$, then   (5.6)

$$f_3\,(x_l\,y_m\,z_n) < F_3$$

$$f_5\,(x_l\,y_m\,z_n) < F_5$$

$$f_6\,(x_l\,y_m\,z_n) < F_6$$

This procedure may obviously be extended to shapes having any number of functions similar to f_2. Note that the conditions (5.6) involve but one test (per grid point) in addition to those which would have been applied had the crystal been described by unlimited bounding functions alone. The procedure therefore does not involve an excessive amount of additional computation.

5.6.3 Limited Bounding Functions (Case II). When the limited bounding functions do not divide the crystal into discreet subvolumes, a special and different sequence of tests must be applied. The procedure required will differ for each shape. The trick in this situation is to (1) successively test volume elements lying outside a given bounding function, starting with the functions at the greatest distance from the origin, and (2) test any particular grid point only once, and not in any subsequent test. In this process the outer regions of the crystal are successively tested until only a "core" contained within unlimited bounding functions results.

Figure 5.3 illustrates this procedure for the crystal of Fig. 5.1 c. In the upper left hand corner all grid points lying outside the function which has been drawn as an extended line have been tested. Grid points contained in the solid region of the crystal have been retained; those in

Figure 5.3

Example of procedure for testing of grid points for a crystal
with limited bounding functions (Case II).
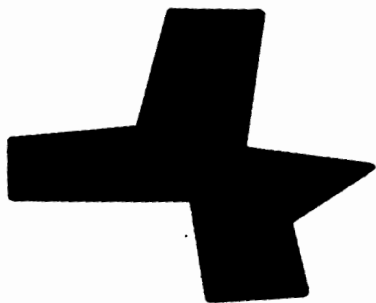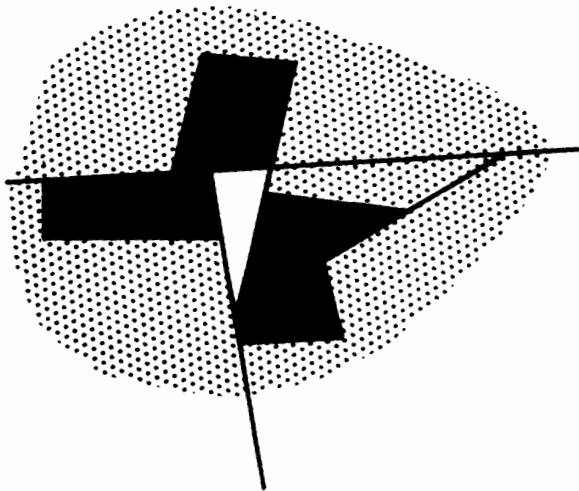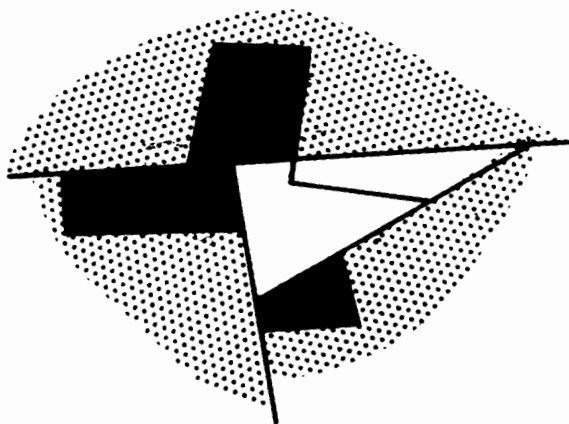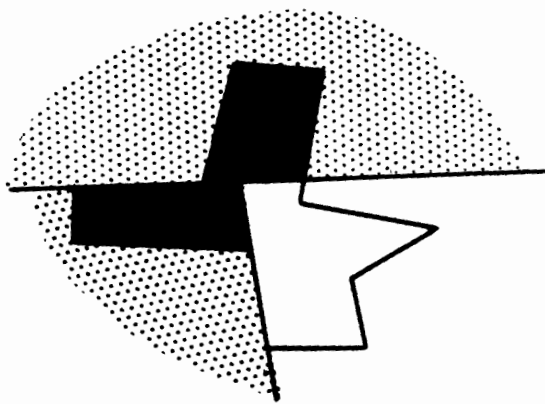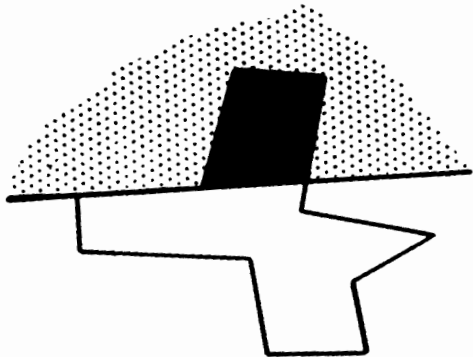
the shaded region have been rejected. In the upper right hand corner of Fig. 5.3 grid points lying outside a second function have been tested. Note that grid points already tested are not tested again. If this were done, certain volume elements actually within the crystal (those occurring in a small triangle bounded within the crystal by the two functions drawn as extended lines) would be incorrectly discarded by the second test.

In this fashion, points lying outside a third and fourth function (Fig. 5.3 center, left and center, right) are tested, until a small triangular core of untested points remains in the crystal. These final points are then tested in the normal fashion, (5.5).

5.7 The Orientation Transformation

In addition to a set of equations $f_{-1}(\underline{x}^1\underline{y}^1\underline{z}^1) \ldots f_{-i}(\underline{x}^1\underline{y}^1\underline{z}^1)$ specifying the surface of the crystal, we now have a set of grid points $\underline{x}^1_{-1} \, \underline{y}^1_{-m} \, \underline{z}^1_{-n}$ representing all volume elements lying within the crystal. The functions and grid points thus far have been specified in a coordinate system $\underline{x}^1\underline{y}^1\underline{z}^1$ relative to the crystal shape. These coördinates will now be transformed into a coordinate system $\underline{x}\,\underline{y}\,\underline{z}$ relative to the diffractometer. The axis $\underline{z}$ will be taken along the goniometer head axis, and the axis $\underline{x}$ along the x-ray beam when all instrumental settings are zero.

This transformation is the operation which is performed to crystallographically orient the crystal shape on the diffractometer. It will therefore be called the orientation transformation. It is desirable to specify the transformation in terms of angles which can readily be determined by the investigator. The transformation will therefore be specified by the polar angles ρ and ϕ, Fig. 5.4, since these angles may always be determined with the aid of a two-circle optical goniometer. The transformation may then be expressed, in terms of the orientation matrix $[\underline{Q}]$;

$$[\underline{x}] = [\underline{Q}] [\underline{x}^1] \qquad\qquad (5.7)$$

Figure 5.4

The orientation transformation. Relation between a coordinate system $x'y'z'$ relative to the crystal in oriented position, and a set of axes xyz relative to the diffractometer when all instrumental settings are at zero.

GONIOMETER
HEAD AXIS
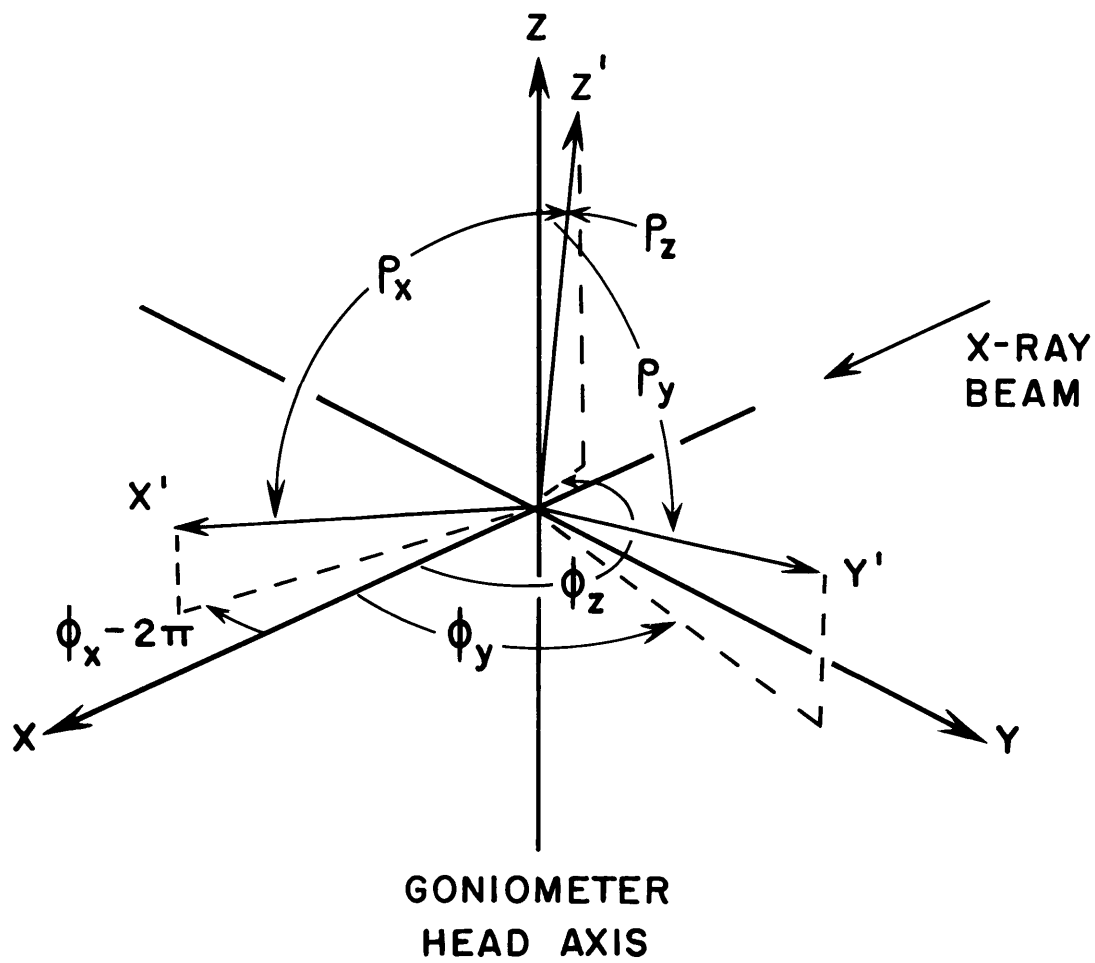
with

$$[\underset{\sim}{Q}] = \begin{bmatrix} \sin\rho_x \cos\phi_x & \sin\rho_y \cos\phi_y & \sin\rho_z \cos\phi_z \\ \sin\rho_x \sin\phi_x & \sin\rho_x \sin\phi_y & \sin\rho_z \sin\phi_z \\ \cos\rho_x & \cos\rho_y & \cos\rho_z \end{bmatrix} \qquad (5.8)$$

In specifying these angles, it should be noted that $[Q]$ is a unitary matrix. The sum of the squares of the elements in any row or column of $[\underset{\sim}{Q}]$ are therefore equal to unity. The angles ρ and ϕ therefore need not be determined for all three axes.

The necessary transformation of the coordinates of each retained grid point $x'_l y'_m z'_n$ is readily performed by application of (5.7). The transformed expressions for the bounding functions may be obtained by use of the inverse of the transformation of (5.7):

$$[\underset{\sim}{x'}] = [\underset{\sim}{Q}]^{-1} [\underset{\sim}{x}] \qquad (5.9)$$

Since $[\underset{\sim}{Q}]$ is a unitary matrix,

$$[\underset{\sim}{Q}]^{-1} = [\underset{\sim}{Q}]^{T} , \qquad (5.10)$$

where $[Q]^{T}$ is the transpose of the matrix $[\underset{\sim}{Q}]$. Although the dominant function of the crystal will be in canonical form in the system $\underline{x'}\underline{y'}\underline{z'}$, this, in general, will not be the case for every function. Therefore, to obtain the equation for the bounding functions in the diffractometer coordinate system, we must substitute the relations (5.9) in the general quadratic form (5.1):

$$\begin{aligned} f(xyz) = \quad & A'[\, \sin^2\rho_x \cos^2\phi_x x^2 + \sin^2\rho_x \sin^2\phi_x y^2 \\ & + \cos^2\rho_x z^2 + 2\sin^2\rho_x \cos\phi_x \sin\phi_x\, xy \\ & + 2\sin\rho_x \cos\rho_x \sin\phi_x\, yz \\ & + 2\sin\rho_x \cos\rho_x \cos\phi_x\, xz\,] \end{aligned}$$

$$+ B'[\ \sin^2\rho_y\ \cos^2\phi_y\, x^2 + \sin^2\rho_y\ \sin^2\phi_y\ y^2$$

$$+ \cos^2\rho_y\ z^2 + 2\sin^2\rho_y\ \cos\phi_y\ \sin\phi_y\ xy$$

$$+ 2\sin\rho_y\ \cos\rho_y\ \sin\phi_y\ yz$$

$$+ 2\sin\rho_x\ \cos\rho_x\ \cos\phi_x\ xz\,]$$

$$+ C'[\ \sin^2\rho_z\ \cos^2\phi_z\ x^2 + \sin^2\rho_z\ \sin^2\phi_z\ y^2 + \cos^2\rho_z\ z^2$$

$$+ 2\sin^2\rho_z\ \cos\phi_z\ \sin\phi_z\ xy$$

$$+ 2\sin\rho_z\ \cos\rho_z\ \sin\phi_z\ yz$$

$$+ 2\sin\rho_z\ \cos\rho_z\ \cos\phi_z\ xz\,]$$

$$+ D'[\ \sin\rho_x\ \sin\rho_y\ \cos\phi_x\ \cos\phi_y\ x^2 + \sin\rho_x\ \sin\rho_y\ \sin\phi_x\ \sin\phi_y\ y^2$$

$$+ \cos\rho_x\ \cos\rho_y\ z^2 + (\sin\rho_x\ \sin\rho_y\ \sin\phi_x\ \cos\phi_y$$

$$+ \sin\rho_x\ \sin\rho_y\ \cos\phi_x\ \sin\phi_y)\,xy + (\cos\rho_x\ \sin\rho_y\ \sin\phi_y$$

$$+ \sin\rho_x\ \cos\rho_y\ \sin\phi_x)\,yz + (\cos\rho_x\ \sin\rho_y\ \cos\phi_y$$

$$+ \sin\rho_x\ \cos\rho_y\ \cos\phi_x)\,xz\,]$$

$$+ E'[\ \sin\rho_y\ \sin\rho_z\ \cos\phi_y\ \cos\phi_z\ x^2 + \sin\rho_y\ \sin\rho_z\ \sin\phi_y\ \sin\phi_z\ y^2$$

$$+ \cos\rho_y\ \cos\rho_z\ z^2 + (\sin\rho_y\ \sin\rho_z\ \sin\phi_y\ \cos\phi_z$$

$$+ \sin\rho_y\ \sin\rho_z\ \cos\phi_y\ \sin\phi_z)\,xy + (\cos\rho_y\ \sin\rho_z\ \sin\phi_z$$

$$+ \sin\rho_y\ \cos\rho_z\ \sin\phi_y)\,yz + (\cos\rho_y\ \sin\rho_z\ \cos\phi_z$$

$$+ \sin\rho_y\ \cos\rho_z\ \cos\phi_y)\,xz\,]$$

$$+ G'[\ \sin\rho_x\ \sin\rho_z\ \cos\phi_x\ \cos\phi_z\ x^2 + \sin\rho_x\ \sin\rho_z\ \sin\phi_x\ \sin\phi_z\ y^2$$

$$+ \cos\rho_x\ \cos\rho_z\ z^2 + (\sin\rho_x\ \sin\rho_z\ \cos\phi_x\ \sin\phi_z$$

$$+ \sin\rho_x\ \sin\rho_z\ \sin\phi_x\ \cos\phi_z)\,xy + (\sin\rho_x\ \cos\rho_z\ \sin\phi_x$$

$$+ \cos\rho_x\ \sin\rho_z\ \sin\phi_z)\,yz + (\sin\rho_x\ \cos\rho_z\ \cos\phi_x$$

$$+ \cos\rho_x\ \sin\rho_z\ \cos\phi_z)\,xz\,]$$

$$+ H'[\, \sin\rho_x \cos\phi_x \; x + \sin\rho_x \sin\phi_x \; y + \cos\rho_x \; z\,]$$

$$+ I'[\, \sin\rho_y \cos\phi_y \; x + \sin\rho_y \sin\phi_y \; y + \cos\rho_y \; z\,]$$

$$+ J'[\, \sin\rho_z \cos\phi_z \; x + \sin\rho_z \sin\phi_z \; y + \cos\rho_z \; z\,]$$

$$= F' = F \tag{5.11}$$

Collection of terms in x^2, y^2, z^2, xy . . . . etc., leads to the desired expression

$$f(xyz) = Ax^2 + By^2 + Cz^2 + Dxy + Eyz + Gzx$$

$$+ Hx + Iy + Jz \equiv F \tag{5.12}$$

with

$$A = A' \sin^2\rho_x \cos^2\phi_x + B' \sin^2\rho_y \cos^2\phi_y + C' \sin^2\rho_z \cos^2\phi_z$$

$$+ D' \sin\rho_x \sin\rho_y \cos\phi_x \cos\phi_y$$

$$+ E' \sin\rho_y \sin\rho_z \cos\phi_y \cos\phi_z$$

$$+ G' \sin\rho_x \sin\rho_z \cos\phi_x \cos\phi_z$$

$$B = A' \sin^2\rho_x \sin^2\phi_x + B' \sin^2\rho_y \sin^2\phi_y + C' \sin^2\rho_z \sin^2\phi_z$$

$$+ D' \sin\rho_x \sin\rho_y \sin\phi_x \sin\phi_y$$

$$+ E' \sin\rho_y \sin\rho_z \sin\phi_y \sin\phi_z$$

$$+ G' \sin\rho_x \sin\rho_z \sin\phi_x \sin\phi_z$$

$$C = A' \cos^2\rho_x \qquad + B' \cos^2\rho_y \qquad + C' \cos^2\rho_z$$

$$+ D' \cos\rho_x \cos\rho_y + E' \cos\rho_y \cos\rho_z + G' \cos\rho_x \cos\rho_z$$

$$D = 2A' \sin^2\rho_x \cos\phi_x \sin\phi_x + 2B' \sin^2\rho_y \cos\phi_y \sin\phi_y$$

$$+ 2C' \sin^2\rho_z \cos\phi_z \sin\phi_z$$

$$+ D'(\sin\rho_x \sin\rho_y \sin\phi_x \cos\phi_y + \sin\rho_x \sin\rho_y \cos\phi_x \sin\phi_y)$$

$$+ E'(\sin\rho_y \sin\rho_z \sin\phi_y \cos\phi_z + \sin\rho_y \sin\rho_z \cos\phi_y \sin\phi_z)$$

$$+ G'(\sin\rho_z \sin\rho_x \sin\phi_z \cos\phi_x + \sin\rho_z \sin\rho_x \cos\phi_z \sin\phi_x)$$

$$E = 2A' \sin\rho_x \cos\rho_x \sin\phi_x + 2B' \sin\rho_y \cos\rho_y \sin\phi_y$$

$$+ 2C' \sin\rho_z \cos\rho_z \sin\phi_z$$

$$+ D'(\cos\rho_x \sin\rho_y \sin\phi_y + \sin\rho_x \cos\rho_y \sin\phi_x)$$

$$+ E'(\cos\rho_y \sin\rho_z \sin\phi_z + \sin\rho_y \cos\rho_z \sin\phi_y)$$

$$+ G'(\cos\rho_z \sin\rho_x \cos\phi_x + \sin\rho_z \cos\rho_x \sin\phi_z)$$

$$G = 2A' \sin\rho_x \cos\rho_x \cos\phi_x + 2B' \sin\rho_y \cos\rho_y \cos\phi_y$$

$$+ 2C' \sin\rho_z \cos\rho_z \cos\phi_z$$

$$+ D'(\sin\rho_y \cos\rho_x \cos\phi_y + \sin\rho_x \cos\rho_y \cos\phi_x)$$

$$+ E'(\sin\rho_z \cos\rho_y \cos\phi_z + \sin\rho_y \cos\rho_z \cos\phi_y)$$

$$+ G'(\sin\rho_x \cos\rho_z \cos\phi_x + \sin\rho_z \cos\rho_x \cos\phi_z)$$

$$H = H' \sin\rho_x \cos\phi_x + I' \sin\rho_y \cos\phi_y + J' \sin\rho_z \cos\phi_z$$

$$I = H' \sin\rho_x \sin\phi_x + I' \sin\rho_y \sin\phi_y + J' \sin\rho_z \sin\phi_z$$

$$J = H' \cos\rho_x + I' \cos\rho_y + J' \cos\rho_z$$

$$F = F' \tag{5.13}$$

The expressions (5.13) are completely general. When the bounding functions are in canonical form, as in Table 5.1, the expressions simplify considerably. These special forms of (5.13) are tabulated in Table 5.2. It should again be pointed out that while these expressions are algebraically complex, they are performed only once for each problem and therefore do not involve an excessive amount of computation.

5.8 The Diffraction Transformation and Equations for the Incident and Diffracted Beams

Expressions have now been obtained for all retained grid point coordinates, $x_{-l}\ y_{-m}\ z_{-n}$, relative to the diffractometer axes, and for all bounding functions relative to the diffractometer axes. All instrumental

Table 5.2

Coefficients in General Quadratic Form Following Orientation Transformation

Geometric shape	Coefficients of general quadratic form in coordinate system of diffractometer				
	A	B	C	D	E
Plane	0	0	0	0	0
Elliptic cylinder	$A'\sin^2\rho_x\cos^2\phi_x$ $+B'\sin^2\rho_y\cos^2\phi_y$	$A'\sin^2\rho_x\sin^2\phi_x$ $+B'\sin^2\rho_y\sin^2\phi_y$	$A'\cos^2\rho_x$ $+B'\cos^2\rho_y$	$2A'\sin^2\rho_x\cos\phi_x\sin\phi_x$ $+2B'\sin^2\rho_y\cos\phi_y\sin\phi_y$	$2A'\sin\rho_x\cos\rho_x\sin\phi_x$ $+2B'\sin\rho_y\cos\rho_y\sin\phi_y$
Elliptic paraboloid	"	"	"	"	"
Hyperbolic paraboloid	"	"	"	"	"
Ellipsoid	$A'\sin^2\rho_x\cos^2\phi_x$ $+B'\sin^2\rho_y\cos^2\phi_y$ $+C'\sin^2\rho_z\cos^2\phi_z$	$A'\sin^2\rho_x\sin^2\phi_x$ $+B'\sin^2\rho_y\sin^2\phi_y$ $+C'\sin^2\rho_z\sin^2\phi_z$	$A'\cos^2\rho_x$ $+B'\cos^2\rho_y$ $+C'\cos^2\rho_z$	$2A'\sin^2\rho_x\cos\phi_x\sin\phi_x$ $+2B'\sin^2\rho_y\cos\phi_y\sin\phi_y$ $+2C'\sin^2\rho_z\cos\phi_z\sin\phi_z$	$2A'\sin\rho_x\cos\rho_x\sin\phi_x$ $+2B'\sin\rho_y\cos\rho_y\sin\phi_y$ $+2C'\sin\rho_z\cos\rho_z\sin\phi_z$
Elliptic cone	"	"	"	"	"
Hyperboloid of one sheet	"	"	"	"	"

Table 5.2 (continued)

Coefficients in General Quadratic Form Following Orientation Transformation

Geometric shape	Coefficients of general quadratic form in coordinate system of diffractometer			
	G	H	I	J
Plane	0	$H' \sin \rho_x \cos \phi_x$ $+ I' \sin \rho_y \cos \phi_y$ $+ J' \sin \rho_z \cos \phi_z$	$H' \sin \rho_x \sin \phi_x$ $+ I' \sin \rho_y \sin \phi_y$ $+ J' \sin \rho_z \sin \phi_z$	$H' \cos \rho_x$ $+ I' \cos \rho_y$ $+ J' \cos \rho_z$
Elliptic cylinder	$2A' \sin \rho_x \cos \rho_x \cos \phi_x$ $+ 2B' \sin \rho_y \cos \rho_y \cos \phi_y$	$H' \sin \rho_x \cos \phi_x$ $+ I' \sin \rho_y \cos \phi_y$	$H' \sin \rho_x \sin \phi_x$ $+ I' \sin \rho_y \sin \phi_y$	$H' \cos \rho_x$ $+ I' \cos \rho_y$
Elliptic paraboloid	"	$H' \sin \rho_x \cos \phi_x$ $+ I' \sin \rho_y \cos \phi_y$ $+ J' \sin \rho_z \cos \phi_z$	$H' \sin \rho_x \sin \phi_x$ $+ I' \sin \rho_y \sin \phi_y$ $+ J' \sin \rho_z \sin \phi_z$	$H' \cos \rho_x$ $+ I' \cos \rho_y$ $+ J' \cos \rho_z$
Hyperbolic paraboloid	"	"	"	"
Ellipsoid	$2A' \sin \rho_x \cos \rho_x \cos \phi_x$ $+ 2B' \sin \rho_y \cos \rho_y \cos \phi_y$ $+ 2C' \sin \rho_z \cos \rho_z \cos \phi_z$	"	"	"
Elliptic cone	"	"	"	"
Hyperboloid of one sheet	"	"	"	"

settings of the diffractometer have been assumed to be at zero. In order to satisfy the diffraction condition for a particular reflection $\underline{hkl}$, it is now necessary to perform a second transformation on the crystal. This transformation, which brings the axes to a new setting $\underline{x}''\underline{y}''\underline{z}''$, is a function of the indices of the reflection $\underline{hkl}$ and the reciprocal cell dimensions $\underline{a}*$, $\underline{b}*$, $\underline{c}*$, $\alpha*$, $\beta*$, $\gamma*$.[1] Rather than repeat transformations of the form (5.13) and (5.9) for each reflection, the reverse transformation will be applied to the expressions for the incident and diffracted beams. The coordinate system $\underline{xyz}$ will therefore be considered fixed to the oriented crystal, and the coordinate system $\underline{x}''\underline{y}''\underline{z}''$ (originally coincident with $\underline{xyz}$) fixed with respect to the diffractometer.

5.8.1 <u>The Precession Method</u>.[2] Figure 5.5 indicates the relation between the coordinate system $\underline{xyz}$, fixed to the crystal, and the coordinate system $\underline{x}''\underline{y}''\underline{z}''$ fixed to the precession camera. Let unit vectors $\underset{\sim}{i}$, $\underset{\sim}{j}$, $\underset{\sim}{k}$ and $\underset{\sim}{i}''$, $\underset{\sim}{j}''$, $\underset{\sim}{k}''$ be defined in the two systems. The nature of the precession motion is such that $\underset{\sim}{i}$ precesses about $\underset{\sim}{i}''$ at constant angle $\bar{\mu}$. The vector $\underset{\sim}{k}$ oscillates back and forth in the $\underline{x}''\underline{y}''$ plane and, at a given point in the precession cycle, is at an angle α to $\underset{\sim}{k}''$. The vector $\underset{\sim}{j}$ should ideally oscillate in the $\underline{x}''\underline{y}''$ plane and, at a given point in the precession cycle, be at an angle β to $\underset{\sim}{j}''$. In the universal-joint suspension presently employed in the precession instrument, however, $\underset{\sim}{j}$ actually oscillates in a plane normal to $\underset{\sim}{k}$, and <u>not</u> in a plane normal to $\underset{\sim}{k}''$. This is the fashion in which the universal-joint motion deviates from a true precession motion.

---

[1] Scaled reciprocal cell dimensions are assumed in this treatment, $\underline{i}.\underline{e}.$ $\underline{a}* \equiv \lambda/d_{100}$, etc., <u>not</u> $1/d_{100}$

[2] Derivation of the transformation was first given by Wasser (1951).

Figure 5.5

The diffraction transformation for the precession method.

Relation between a coordinate system $\underline{xyz}$ fixed to the crystal shape

and reciprocal lattice, and a system $\underline{x}''\underline{y}''\underline{z}''$ relative to the precession

instrument.
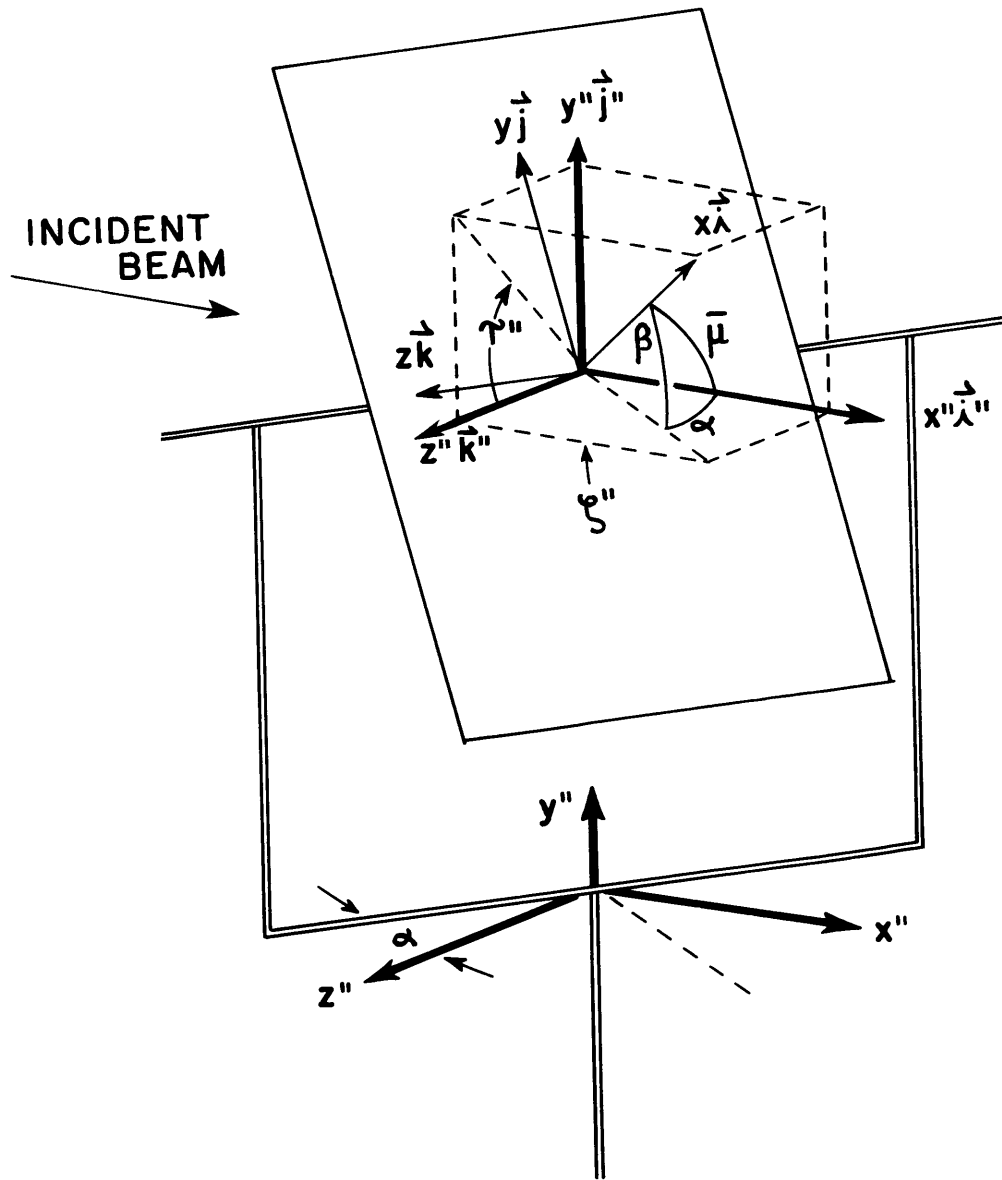
The relation between the axes $\underline{xyz}$ and $\underline{x''y''z''}$ is readily expressed in terms of the angles α and β.

$$\underline{i} = \cos\alpha\,\cos\beta\,\underline{i}'' + \sin\beta\,\underline{j}'' + \sin\alpha\,\cos\beta\,\underline{k}''$$

$$\underline{j} = -\cos\alpha\,\sin\beta\,\underline{i}'' + \cos\beta\,\underline{j}'' - \sin\alpha\,\cos\beta\,\underline{k}'' \qquad (5.14)$$

$$\underline{k} = -\sin\alpha \qquad \underline{i}'' \qquad + \cos\alpha \qquad \underline{k}''$$

The desired diffraction matrix $[D]$ is

$$[D] = \begin{bmatrix} \cos\alpha\,\cos\beta & \sin\beta & \sin\alpha\,\cos\beta \\ -\cos\alpha\,\sin\beta & \cos\beta & -\sin\alpha\,\sin\beta \\ -\sin\alpha & 0 & \cos\alpha \end{bmatrix} \qquad (5.15)$$

The angles α and β are not independent. Since, by definition, $\underline{i}$ is always at an angle $\bar{\mu}$ to $\overrightarrow{i}''$,

$$\underline{i} \cdot \underline{i}'' = \cos\bar{\mu} \qquad (5.16)$$

But, from (5.14),

$$\underline{i} \cdot \underline{i}'' = (\cos\alpha\,\cos\beta\,\underline{i}'' + \sin\beta\,\underline{j}'' + \sin\alpha\,\cos\beta\,\underline{k}'') \cdot \underline{i}''$$

$$= \cos\alpha\,\cos\beta \qquad (5.17)$$

Therefore

$$\cos\alpha\,\cos\beta = \cos\bar{\mu} \qquad (5.18)$$

It will also be convenient to define the diffraction matrix in terms of cylindrical coordinates for the precessing axis $\underline{i}$. Figure 5.5 also defines the cylindrical coordinates τ'' and ζ''; the value of the third coordinate for the end of $\overrightarrow{i}$ is unity. The relations involving α and β in (5.15) may be expressed in terms of τ'' by noting that

$$\underline{i} = \cos\bar{\mu}\,\underline{i}'' + \sin\bar{\mu}\,\sin\tau''\,\underline{j}'' + \cos\tau''\,\underline{k} \qquad (5.19)$$

Comparison with (5.14) yields

$$\sin\beta = \sin\bar{\mu}\,\sin\tau'' \qquad (5.20)$$

$$\sin\alpha\,\cos\beta = \sin\bar{\mu}\,\cos\tau'' \qquad (5.21)$$

Transformation of the remaining terms in (5.14) may be accomplished with the aid of (5.20) and (5.21) by using the relations

$$\cos\beta = (1 - \sin^2\beta)^{\frac{1}{2}}$$

$$= (1 - \sin^2\bar{\mu} \sin^2 \tau'')^{\frac{1}{2}} \tag{5.22}$$

From (5.21) and (5.22)

$$\sin\alpha = \frac{\sin\bar{\mu} \cos\tau''}{\cos\beta}$$

$$= \frac{\sin\bar{\mu} \cos\tau''}{(1 - \sin^2\bar{\mu} \sin^2\tau'')^{\frac{1}{2}}} \tag{5.23}$$

From (5.18) and (5.22)

$$\cos\alpha = \frac{\cos\bar{\mu}}{\cos\beta}$$

$$= \frac{\cos\bar{\mu}}{(1 - \sin^2\bar{\mu} \sin^2\tau'')^{\frac{1}{2}}} \tag{5.24}$$

From (5.20) and (5.24)

$$\cos\alpha \sin\beta = \frac{\cos\bar{\mu} \sin\bar{\mu} \sin\tau''}{(1 - \sin^2\bar{\mu} \sin^2\tau'')^{\frac{1}{2}}} \tag{5.25}$$

From (5.20) and (5.23)

$$\sin\alpha \sin\beta = \frac{\sin^2\bar{\mu} \sin\tau'' \cos\tau''}{(1 - \sin^2\bar{\mu} \sin^2\tau'')^{\frac{1}{2}}} \tag{5.26}$$

Using relations (5.18) through (5.26), the diffraction matrix may be expressed

$$[D] = \begin{bmatrix} \cos\bar{\mu} & \sin\bar{\mu} \sin\tau'' & \sin\bar{\mu} \sin\tau'' \\[2em] \dfrac{-\cos\bar{\mu} \sin\bar{\mu} \sin\tau''}{(1 - \sin^2\bar{\mu} \sin^2\tau'')^{\frac{1}{2}}} & (1 - \sin^2\bar{\mu} \sin^2\tau'')^{\frac{1}{2}} & \dfrac{\sin^2\bar{\mu} \sin\tau'' \cos\tau''}{(1 - \sin^2\bar{\mu} \sin^2\tau'')^{\frac{1}{2}}} \\[2em] \dfrac{-\sin\bar{\mu} \cos\tau''}{(1 - \sin^2\bar{\mu} \sin^2\tau'')^{\frac{1}{2}}} & 0 & \dfrac{\cos\bar{\mu}}{(1 - \sin^2\bar{\mu} \sin^2\tau'')^{\frac{1}{2}}} \end{bmatrix} \tag{5.27}$$

The vector representing the incident beam assumes a very simple expression in the coordinate system $\underline{x}''\underline{y}''\underline{z}''$. An expression for the diffracted beam, however, is difficult to obtain. Therefore, for the case of the precession method it is simpler to transform the sphere of reflection into the coordinate system of the crystal, and then derive expressions for the incident and diffracted beam. This is easier than transforming explicit expressions for the beam vectors, as outlined in the discussion of the general method, Section 5.3.

Relative to the precession camera axes $\underline{x}''\underline{y}''\underline{z}''$, the sphere of reflection has unit radius and has its center located at $\underline{x}_0'' = -1$, $\underline{y}_0'' = \underline{z}_0'' = 0$. To obtain the coordinates of the center relative to axes fixed in reciprocal space (to which the coordinate system, $\underline{x}\underline{y}\underline{z}$, fixed to the crystal shape also applies) the transformation

$$\begin{Bmatrix} x_o \\ y_0 \\ z_0 \end{Bmatrix} = [D] \begin{Bmatrix} x_0'' \\ y_0'' \\ z_0'' \end{Bmatrix} = [D] \begin{Bmatrix} -1 \\ 0 \\ 0 \end{Bmatrix} \tag{5.28}$$

is performed. Using the expression (5.27) for $[D]$:

$$x_0 = -\cos\bar{\mu} \tag{5.29a}$$

$$y_0 = \frac{\cos\bar{\mu}\,\sin\bar{\mu}\,\sin\tau''}{(1 - \sin^2\bar{\mu}\,\sin^2\tau'')^{\frac{1}{2}}} \tag{5.29b}$$

$$z_0 = \frac{\sin\bar{\mu}\,\cos\tau''}{(1 - \sin^2\bar{\mu}\,\sin^2\tau'')^{\frac{1}{2}}} \tag{5.29c}$$

Relation (5.29a) confirms a relation obvious from the usual diagram of reciprocal space drawn in the coordinate system of the instrument; namely that the center of the sphere of reflection is located at a distance $\cos\bar{\mu}$ from the zero level. Relations (5.29b) and (5.29c) are more readily understood when transformed into the cylindrical coordinates

$$\zeta_0 = x_0 = -\cos\bar{\mu} \qquad (5.30\underline{a})$$

$$\xi_0^2 = y_0^2 + z_0^2 \qquad (5/30\underline{b})$$

$$\tau_0 = \tan^{-1} y_0/z_0 \qquad (5.30\underline{c})$$

The coordinates are indicated in Fig. 5.6. Use of relations (5.29$\underline{b}$) and (5.29$\underline{c}$) yields

$$\xi_0^2 = \frac{\cos^2\bar{\mu}\,\sin^2\bar{\mu}\,\sin^2\tau'' + \sin^2\bar{\mu}\,\cos^{\frac{1}{2}}\tau''}{1 - \sin^2\bar{\mu}\,\sin^2\tau''}$$

$$= \frac{\sin^2\bar{\mu}\,(\cos^2\bar{\mu}\,\sin^2\tau'' + \cos^2\tau'')}{1 - \sin^2\bar{\mu}\,\sin^2\tau''}$$

$$= \frac{\sin^2\bar{\mu}\,[\cos^2\tau'' + \sin^2\tau''\,(1 - \sin^2\bar{\mu})]}{1 - \sin^2\bar{\mu}\,\sin^2\tau''}$$

$$= \frac{\sin^2\bar{\mu}\,[1 - \sin^2\tau''\,\sin^2\bar{\mu}]}{1 - \sin^2\bar{\mu}\,\sin^2\tau''}$$

$$= \sin^2\bar{\mu} \qquad (5.31)$$

Relation (5.31) confirms the relation that, in reciprocal space, the center of the sphere of reflection lies at a distance $\sin\bar{\mu}$ from a line through the origin of reciprocal space and normal to the zero level. Relation (5.30$\underline{c}$) gives the desired relation between the angular position of the center of the sphere of reflection and the angular position of the precessing axis. Using (5.29$\underline{b}$) and (5.29$\underline{c}$)

$$\tau_0 = \tan^{-1}\left[\frac{\cos\bar{\mu}\,\sin\bar{\mu}\,\sin\tau''}{\sin\bar{\mu}\,\cos\tau''}\right]$$

$$= \tan^{-1}(\cos\bar{\mu}\,\tan\tau'') \qquad (5.32)$$

Note that the modifying factor $\cos\bar{\mu}$ on the right of (5.32) causes the motion of τ_0 to differ from the motion of the precessing axis τ.

Figure 5.6 now permits derivation of the desired expressions for unit vectors $\underset{\sim}{s}_0$ and $\underset{\sim}{s}$ which describe the directions of the incident and diffracted beams, respectively, in the coordinate system of the crystal. The coordinates of the center of the sphere of reflection are

$$x_0 = -\cos\bar{\mu}$$

$$y_0 = \sin\bar{\mu}\,\sin T_0 \qquad (5.33)$$

$$z_0 = \sin\bar{\mu}\,\cos T_0$$

The coordinates of a given reciprocal lattice point, Fig. 5.6 may be given by

$$x = -d*$$

$$y = \xi_{hkl}\,\sin T_{hkl} \qquad (5.34)$$

$$z = \xi_{hkl}\,\cos T_{hkl}$$

The direction of the incident beam is parallel to a line passing through the center of the sphere of reciprocal space and the origin. Since the radius of the sphere is unity, and since the sphere passes through the origin, the vector from the center of the sphere to the origin is the desired unit vector $\underset{\sim}{s}_0$. Therefore, using (5.33),

$$\underset{\sim}{s}_0 = s_{0_x}\,i + s_{0_y}\,j + s_{0_z}\,k \qquad (5.35)$$

with

$$s_{0_x} = -\cos\bar{\mu}$$

$$s_{0_y} = \sin\bar{\mu}\,\sin T_0 \qquad (5.36)$$

$$s_{0_z} = \sin\bar{\mu}\,\cos T_0 \ .$$

The vector from the center of the sphere of reflection to reciprocal lattice point P_{hkl} gives the direction of the diffracted beam:

$$S = S_x\,i + S_y\,j + S_z\,k \qquad (5.37)$$

Figure 5.6

Position of the center of the sphere of reflection relative to axes xyz fixed with respect to the crystal shape and reciprocal lattice (Precession method).
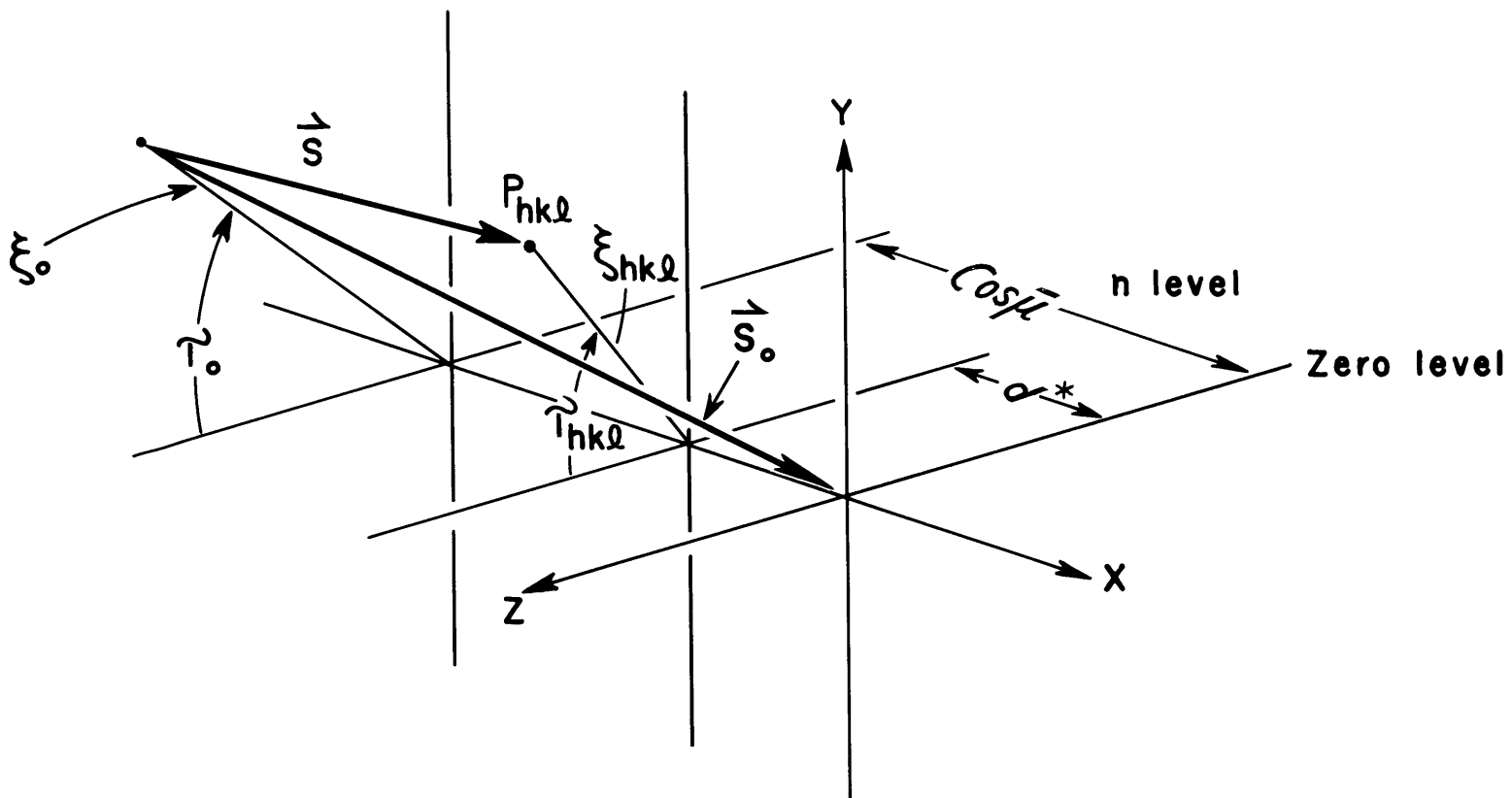
From (5.33) and (5.34) the desired unit vector $\underset{\sim}{s}$ is given by

$$\underset{\sim}{s} = \frac{S_x}{|S|}\,\underset{\sim}{i} + \frac{S_y}{|S|}\,\underset{\sim}{j} + \frac{S_z}{|S|}\,\underset{\sim}{k} \tag{5.38}$$

with

$$S_x = \cos\bar{\mu} - d^* = \cos\bar{\nu} \tag{5.39}$$

$$S_y = \xi_{hkl}\,\sin\tau_{hkl} - \sin\bar{\mu}\,\sin\tau_0$$

$$S_z = \xi_{hkl}\,\cos\tau_{hkl} - \sin\bar{\mu}\,\cos\tau_0$$

$$|S| = [\,\cos^2\bar{\nu} + (\xi_{hkl}\,\sin\tau_{hkl} - \sin\bar{\mu}\,\sin\tau_0)^2$$

$$+ (\xi_{hkl}\,\cos\tau_{hkl} - \sin\bar{\mu}\,\cos\tau_0)^2\,]^{\frac{1}{2}}$$

It now remains to express ξ_{hkl}, τ_{hkl} and τ_0 in terms of hkl and the reciprocal cell dimensions of a general triclinic lattice. Figure 5.7a presents a diagram of an upper-level of the reciprocal lattice ($\underline{x} = -\underline{d}^*$). The center, P_0, of the circular intersection of the sphere of reflection with the level is located at distance $\xi_0 = \sin\bar{\mu}$ from the origin (5.31). The circle of intersection has radius $\sin\bar{\mu} - \underline{d}^* = \sin\bar{\nu}$. It may be seen that there are two locations of the center of this circle, $P_0^{\,1}$ and $P_0^{\,2}$ at which reflections are generated. These locations occur at cylindrical coordinates $\tau_0^{\,1}$ and $\tau_0^{\,2}$. From Fig. 5.7a it may be seen that the desired expression for τ_0 in terms of hkl is given by

$$\tau_0^{\,1} = \tau_{hkl} - \eta$$
$$\tau_0^{\,2} = \tau_{hkl} + \eta \tag{5.40}$$

The values of η may be found by applying the law of cosines to the triangle bounded by ξ_{hkl} $\sin\bar{\mu}$ and $\sin\bar{\nu}$:
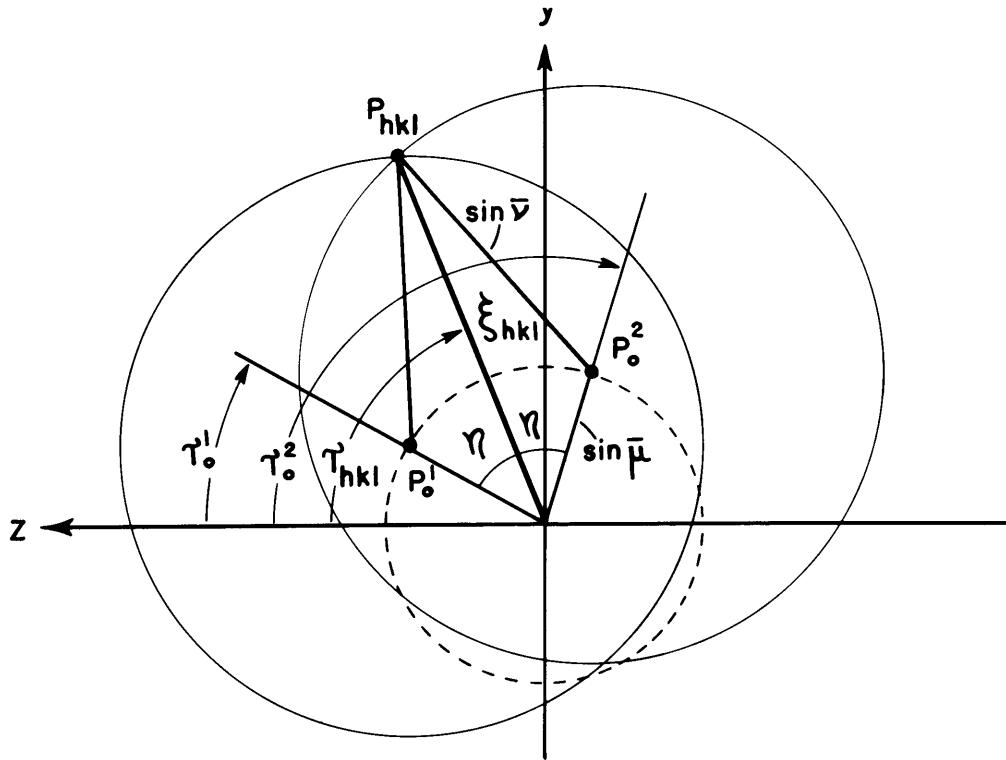
$$\cos\eta = \frac{\sin^2\bar{\mu} + \xi_{hkl}^2 - \sin^2\bar{\nu}}{2\xi_{hkl}\,\sin\bar{\mu}} \tag{5.41}$$
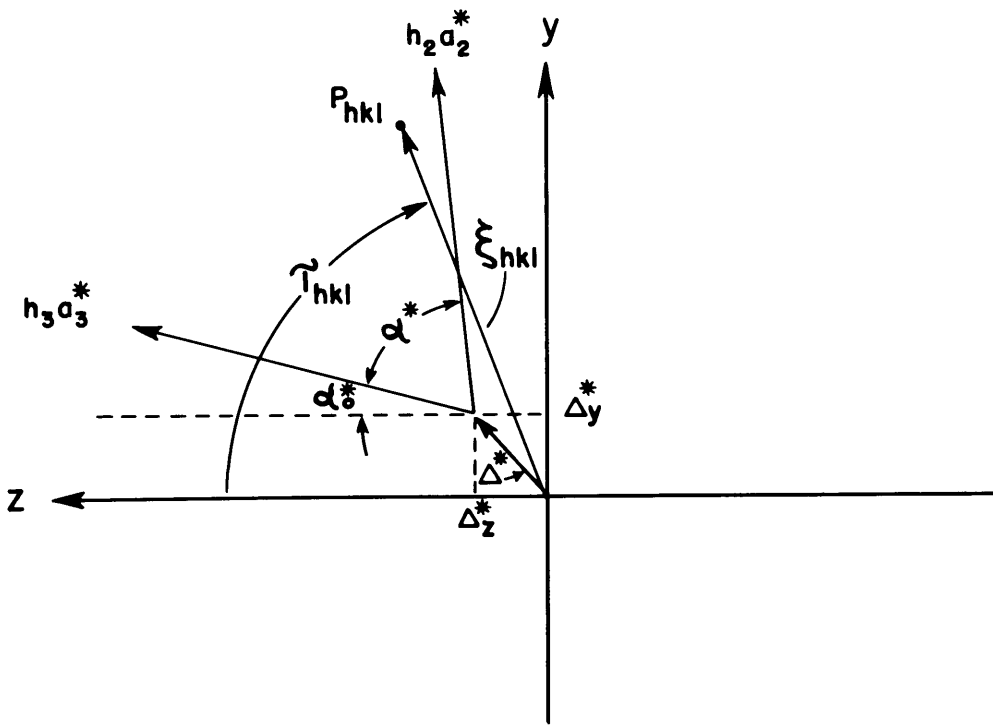
Figure 5.7

Relation between center of sphere of reflection and coordinates

of a reciprocal lattice point in the precession method.

(a) Relation between τ_0 and τ_{hkl}

(b) Derivation of τ_{hkl}

(a)

(b)

The reciprocal cell constants must now be used to evaluate ξ_{hkl} and τ_{hkl}. As shown in Fig. 5.7b, the upper level of a triclinic reciprocal lattice is displaced from the origin by a vector Δ^* which will be a function of the reciprocal cell constants and the index h_1 of the level. Also, it is convenient to assume[1] that the axis a_3^* makes a general angle α_0^* with z. The value of ξ_{hkl} is given by

$$\xi_{hkl} = (\xi_y^2 + \xi_z^2)^{\frac{1}{2}} \tag{5.42}$$

$$\tau_{hkl} = \tan^{-1}(\xi_y/\xi_z) \tag{5.43}$$

with

$$\xi_y = \Delta_y^* + h_2 a_2^* \sin(\alpha^* + \alpha_0^*) + h_3 a_3^* \sin \alpha_0^* \tag{5.44}$$

$$\xi_z = \Delta_z^* + h_2 a_2^* \cos(\alpha^* + \alpha_0^*) + h_3 a_3^* \cos \alpha_0^*$$

Expressions for Δ_y^* and Δ_z^* may be determined by expressing $h_1 a_1^*$ as

$$h_1 a_1^* = \Delta_x^* \, \underset{\sim}{i} + \Delta_y^* \, \underset{\sim}{j} + \Delta_z^* \, \underset{\sim}{k} \tag{5.45}$$

Similarly,

$$h_2 a_2^* = h_2 a_2^* \sin(\alpha^* + \alpha_0^*) \, \underset{\sim}{j} + h_2 a_2^* \cos(\alpha^* + \alpha_0^*) \, \underset{\sim}{k} \tag{5.46}$$

$$h_3 a_3^* = h_3 a_3^* \sin \alpha_0^* \, \underset{\sim}{j} + h_3 a_3^* \cos \alpha_0^* \, \underset{\sim}{k} \tag{5.47}$$

---

[1] This may, in general, be the case for a triclinic or monoclinic crystal. Introduction of this variable, however, also allows a convenient device for specifying the orientation of the crystal axes in the yz plane. For an orthogonal crystal, for example, α_0^* may be specified as either 0 or $\pi/2$, corresponding to situations in which a_3^* is horizontal or vertical. Some provision must be made for internal transformation of indices in the program, since the orientation of the crystal may not correspond to that used to derive the expressions of this section. If the orientation of axes in the yz plane is unimportant, only three crystal orientations need be distinguished. These occur when a, b, or c are chosen as the precession axis.

Forming the dot-product of (5.45) into (5.46) and (5.47) provides

$$h_1 a_1^* \cos \gamma^* = \Delta_y^* \sin(\alpha^* + \alpha_0^*) + \Delta_z^* \cos(\alpha^* + \alpha_0^*) \qquad (5.48)$$

$$h_1 a_1^* \cos \beta^* = \Delta_y^* \sin \alpha_0^* + \Delta_z^* \cos \alpha_0^* \qquad (5.49)$$

Solution of (5.48) and (5.49) for Δ_y^* and Δ_z^* leads to

$$\Delta_y^* = \frac{h_1 a_1^* [\cos \gamma^* \cos \alpha_0^* - \cos \beta^* \cos(\alpha^* + \alpha_0^*)]}{\sin \alpha^*} \qquad (5.50)$$

$$\Delta_z^* = \frac{h_1 a_1^* [\cos \beta^* \sin(\alpha^* + \alpha_0^*) - \cos \gamma^* \sin \alpha_0^*]}{\sin \alpha^*} \qquad (5.51)$$

All quantities required for the expressions for $\underset{\sim}{s}_0$ (5.35) and $\underset{\sim}{s}$ (5.38) are now expressed in terms of hkl and reciprocal cell constants in relations (5.39) through (5.44), and (5.50) and (5.51).

5.8.2 The Equi-inclination Weissenberg Method.

Figure 5.8 indicates the geometry employed in recording upper-level reflections by the equi-inclination method. The coordinate system $\underline{x}''\underline{y}''\underline{z}''$ is again defined relative to the diffractometer so that $\underline{x}''$ is along the incident x-ray beam, and $\underline{z}''$ is along the diffractometer spindle axes. For upper-levels, the incident beam $\underset{\sim}{s}_0$, originally parallel to $\underline{x}''$, is inclined an amount μ to $\underline{x}''$ in the $\underline{x}''\underline{z}''$ plane. The expression for $\underset{\sim}{s}_0''$ is therefore given by

$$\underset{\sim}{s}_0'' = \cos \mu \, \underset{\sim}{i}'' - \sin \mu \, \underset{\sim}{k}'' \qquad (5.52)$$

The diffracted beam, $\underset{\sim}{s}''$, is at an angle ν to the $\underline{x}''\underline{y}''$ plane. Under equi-inclination conditions, $\nu = \mu$. The diffracted beam also is inclined to the $\underline{x}''\underline{z}''$ plane by an amount specified by Υ, which is the angle between the projections of $\underset{\sim}{s}_0$ and $\underset{\sim}{s}$ on the $\underline{x}''\underline{y}''$ plane. The expression for $\underset{\sim}{s}''$ is therefore

$$\underset{\sim}{s}'' = \cos \mu \cos \Upsilon \, \underset{\sim}{i}'' + \cos \mu \sin \Upsilon \, \underset{\sim}{j}'' + \sin \mu \, \underset{\sim}{k}'' \qquad (5.53)$$

Figure 5.8

Geometry in recording upper-level reflections by the equi-

inclination method. The crystal axes xyz are initially coincident with

the diffractometer axes x"y"z".
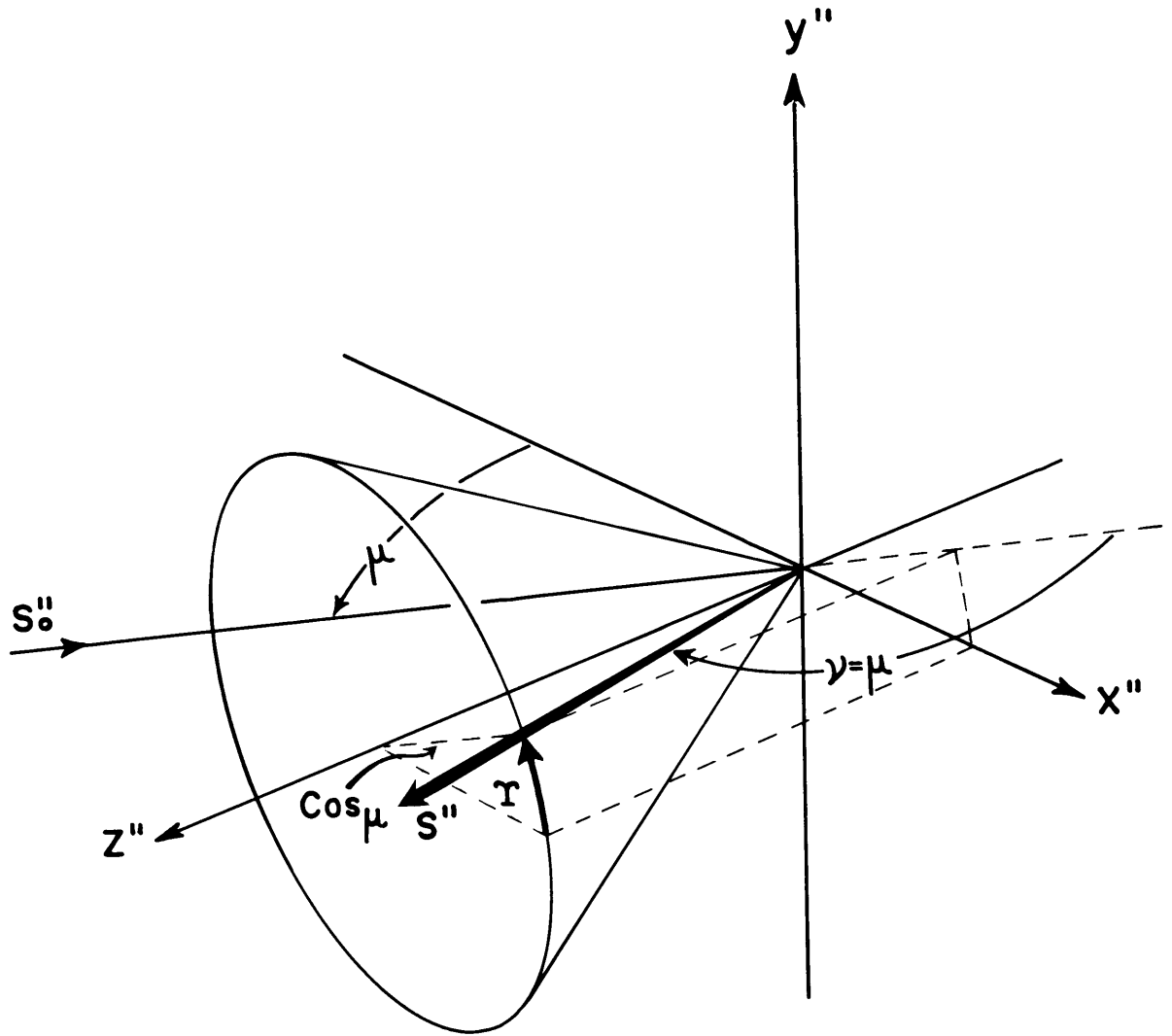
In order to bring the crystal to a position in which a reflection is generated, it is necessary to rotate the crystal an amount ϕ about $\underline{z}''$. In defining ϕ, it is customary to denote ϕ as 0 when $\underline{a}^*$ is parallel to $\underline{x}$. For complete generality it will be assumed that the $\underline{a}^*$ makes an angle ϕ_0 with $\underline{x}''$, Fig. 5.9. The crystal must therefore be rotated an amount $\phi - \phi_0$ to satisfy the diffraction condition. The diffraction transformation is therefore:

$$\underline{x} = [\underline{D}] \, \underline{x}'' \tag{5.54}$$

with

$$[\underline{D}] = \begin{bmatrix} \cos(\phi - \phi_0) & -\sin(\phi - \phi_0) & 0 \\ \sin(\phi - \phi_0) & \cos(\phi - \phi_0) & 0 \\ 0 & 0 & 1 \end{bmatrix} \tag{5.55}$$

where, as before, $\underline{xyz}$ are the crystal axes relative to the diffractometer axes when in diffracting position. Again, the reverse transformation

$$[\underline{D}]^{-1} = \begin{bmatrix} \cos(\phi - \phi_0) & \sin(\phi - \phi_0) & 0 \\ -\sin(\phi - \phi_0) & \cos(\phi - \phi_0) & 0 \\ 0 & 0 & 1 \end{bmatrix} \tag{5.56}$$

will be applied to the expressions for $\underline{s}''_0$ and $\underline{s}''$ to obtain relations for the incident and diffracted beams in the coordinate system of the crystal. The relations

$$\underline{s}_0 = [\underline{D}]^{-1} \underline{s}''_0 \tag{5.57}$$

and

$$\underline{s} = [\underline{D}]^{-1} \underline{s}'' \tag{5.58}$$

lead to

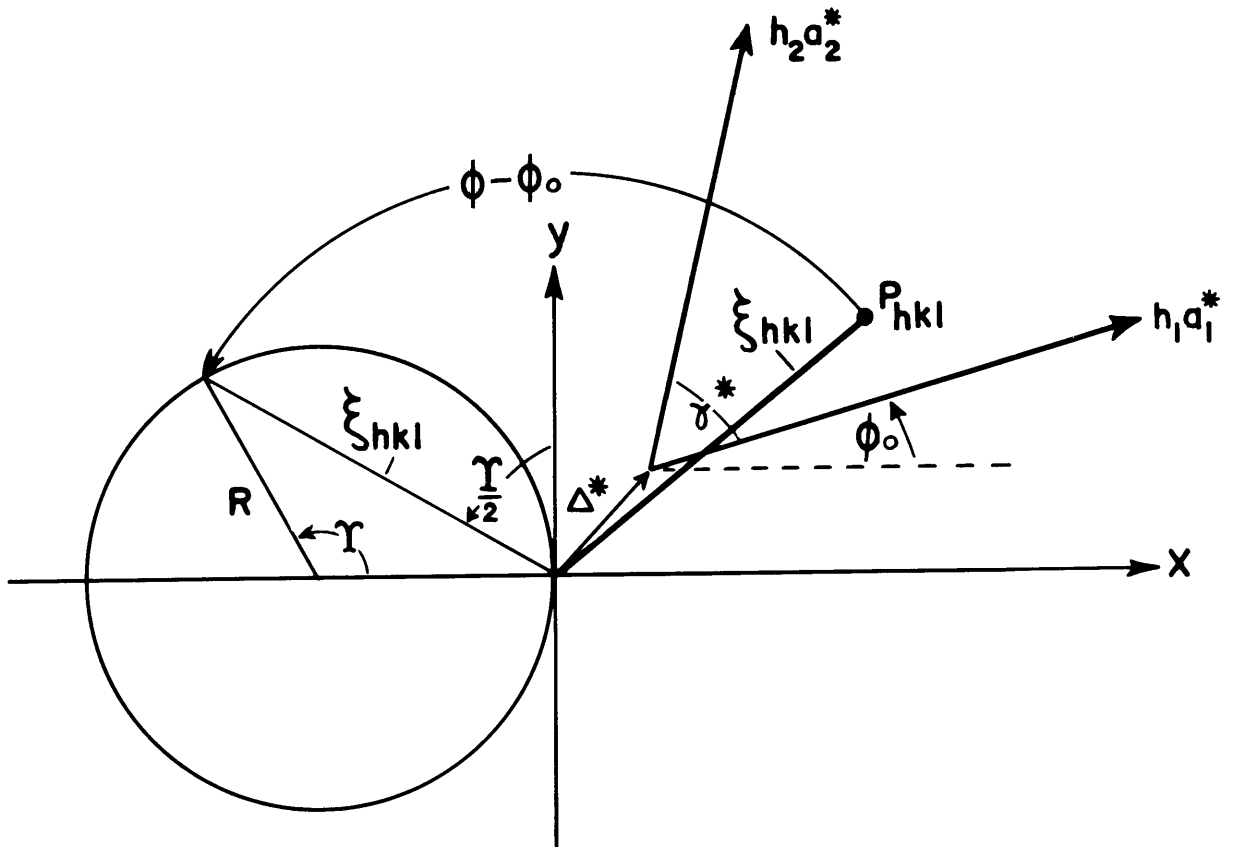$$s_{0_x} = \cos\mu \, \cos(\phi - \phi_0)$$

$$s_{0_y} = -\cos\mu \, \sin(\phi - \phi_0) \tag{5.59}$$

$$s_{0_z} = -\sin\mu$$

and

Figure 5.9

Section through an upper level of a reciprocal lattice being investigated with equi-inclination geometry.

$$s_x = \cos\mu \cos\Upsilon \cos(\phi - \phi_0) + \cos\mu \sin\Upsilon \sin(\phi - \phi_0)$$

$$s_y = -\cos\mu \cos\Upsilon \sin(\phi - \phi_0) + \cos\mu \sin\Upsilon \cos(\phi - \phi_0)$$

$$s_z = \sin\mu \tag{5.60}$$

It now remains to express μ, Υ, and ϕ in terms of the indices of the reflection, hkl, and the reciprocal cell constants.[1] These have been previously derived by Prewitt (1960). Figure 5.9 gives a view along z of the geometry in the level being recorded. The value of Υ is given by

$$\Upsilon = 2\sin^{-1}\left(\frac{\xi}{2R}\right) \tag{5.61}$$

For equi-inclination

$$R = \cos\mu = \left(1 - \frac{\zeta^2}{4}\right)^{\frac{1}{2}} \tag{5.62}$$

An expression for ξ has been previously given in (5.42):

$$\xi = \left(\xi_x^2 + \xi_y^2\right)^{\frac{1}{2}} \tag{5.63}$$

with

$$\xi_x = \Delta_x^* + h_1 a_1^* \cos\phi_0 + h_2 a_2^* \cos(\gamma^* + \phi_0) \tag{5.64}$$

$$\xi_y = \Delta_y^* + h_1 a_1^* \sin\phi_0 + h_2 a_2^* \sin(\gamma^* + \phi_0) \tag{5.65}$$

and

$$\Delta_x^* = \frac{h_3 a_3^*\left[\cos\alpha^* \cos\phi_0 - \cos\beta^* \cos(\gamma^* + \phi_0)\right]}{\sin\gamma^*} \tag{5.66}$$

$$\Delta_y^* = \frac{h_3 a_3^*\left[\cos\beta^* \sin(\gamma^* + \phi_0) - \cos\alpha^* \sin\phi_0\right]}{\sin\gamma^*} \tag{5.67}$$

The value for ζ may be obtained from the relation

$$\left(h_3 a_3^*\right)^2 = \zeta^2 + \left(\Delta_x^*\right)^2 + \left(\Delta_y^*\right)^2 \tag{5.68}$$

Therefore

$$\zeta = \left[\left(h_3 a_3^*\right)^2 - \left(\Delta_x^*\right)^2 - \left(\Delta_y^*\right)^2\right]^{\frac{1}{2}} \tag{5.69}$$

---

[1] It should be noted that in using the equi-inclination or, in the following section, the Eulerian cradle geometries, one ordinarily will have computed these angles for collection of the intensities. A useful option of the program based on this method is to read in these angles from cards rather than computing them directly within this program.

Figure 5.9 shows that the value of $(\phi - \phi_0)$ is given by

$$(\phi - \phi_0) = \frac{\pi}{2} - \tan^{-1}(\xi_y/\xi_x) + \frac{\Upsilon}{2} \qquad (5.70)$$

if $\underline{P}_{hkl}$ is in the quadrant shown. An unambiguous expression for $\phi - \phi_0$ (Prewitt, 1960) which gives the correct value for $\underline{P}_{hkl}$ in any quadrant, is

$$(\phi - \phi_0) = \pi - \tan^{-1}(\xi_y/\xi_x) + \frac{\Upsilon}{2} - (\xi_x/|\xi_x|)\frac{\pi}{2} \qquad (5.71)$$

The quantities required in the expressions for the incident- and diffracted-beam vectors, (5.59) and (5.60) have now been determined in terms of the reciprocal cell constants and indices of the reflection with relations (5.61) through (5.71).

5.8.3 The Eulerian Cradle Method.

In the Eulerian Cradle geometry, all upper-level reflections are brought to the diffraction condition in the zero level. The incident beam, Fig. 5.10 $\underline{a}$, initially parallel with the $\underline{x}''$ axis, is inclined at the proper Bragg angle θ. The diffracted beam, also in the zero level, also makes an angle θ to the $\underline{x}''$ axis. The expressions for the incident and diffracted beam in the coordinate system of the diffractometer are therefore

$$\underline{s}_0'' = \cos\theta \; \underline{i}'' - \sin\theta \; \underline{j}'' \qquad (5.72)$$

$$\underline{s}'' = \cos\theta \; \underline{i}'' + \sin\theta \; \underline{j}''. \qquad (5.73)$$

To bring the crystal into diffracting position, a rotation ϕ, Fig. 5.10 $\underline{b}$ is first performed. This operation brings the reciprocal lattice point $\underline{P}_{hkl}$ into the plane $\underline{y}''\underline{z}''$. A second rotation χ is then performed to bring the reciprocal lattice point to the $\underline{y}''$ axis.

The matrix of the transformation for the first operation is

$$[\underline{\phi}] = \begin{bmatrix} \cos\phi & -\sin\phi & 0 \\ \sin\phi & \cos\phi & 0 \\ 0 & 0 & 1 \end{bmatrix} \qquad (5.74)$$

Figure 5.10

Geometry in recording upper-level reflections by the Eulerian

cradle method. (a) Location of the incident and diffracted beam with

respect to the diffractometer axes. (b) Rotations ϕ and χ necessary

to bring an upper level reciprocal lattice point to the zero level.

(a)

(b)
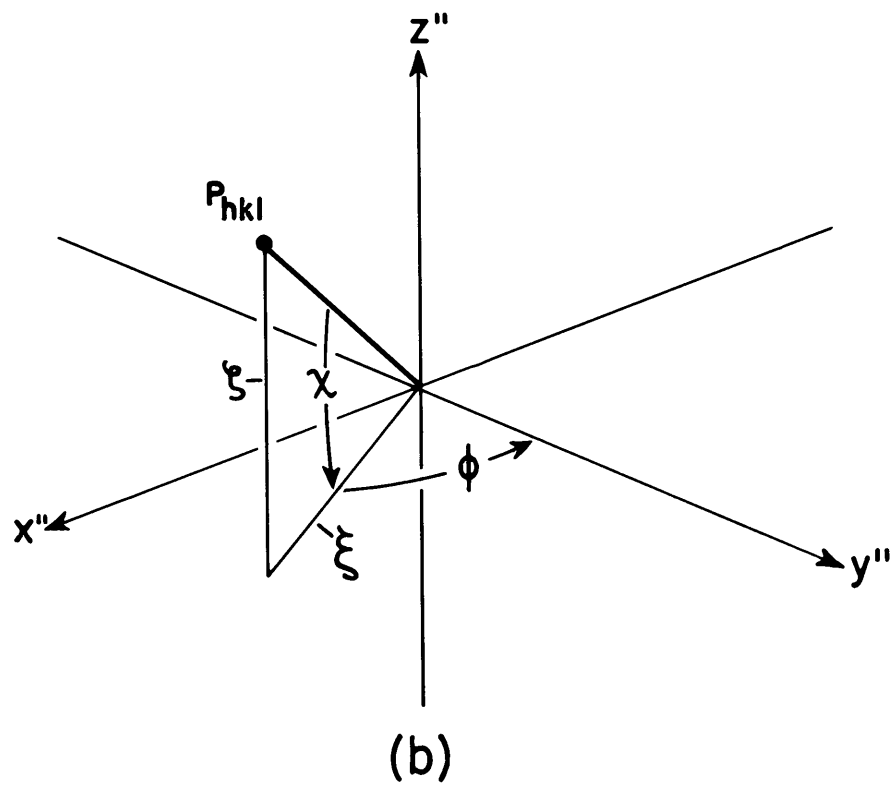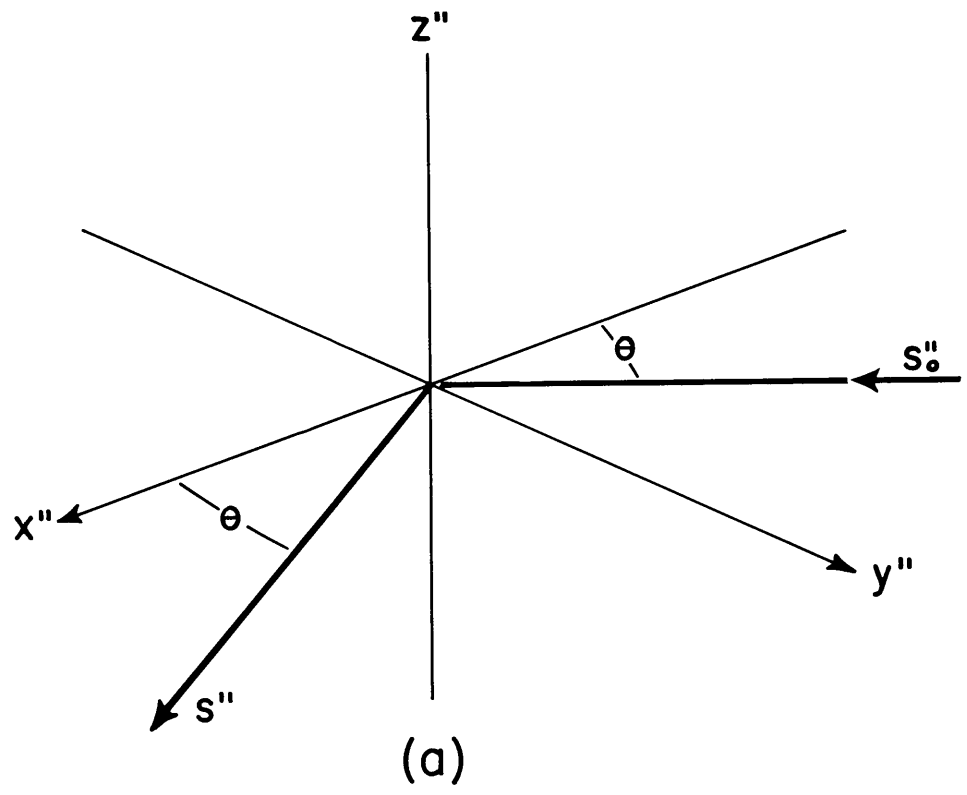
The second rotation χ is performed about $\underline{x}$" so that

$$[\chi] = \begin{bmatrix} 1 & 0 & 0 \\ 0 & \cos\chi & \sin\chi \\ 0 & -\sin\chi & \cos\chi \end{bmatrix} \qquad (5.75)$$

The diffraction transformation, $[D]$, where

$$[\underline{x}] = [\underline{D}]\,\underline{x}" \qquad (5.76)$$

is therefore given by

$$[\underline{D}] = [\underline{\chi}][\underline{\phi}] \qquad (5.77)$$

so that

$$[\underline{D}] = \begin{bmatrix} \cos\phi & -\sin\phi & 0 \\ \cos\chi\sin\phi & \cos\chi\cos\phi & \sin\chi \\ -\sin\chi\sin\phi & -\sin\chi\cos\phi & \cos\chi \end{bmatrix} \qquad (5.78)$$

Application of the reverse transformation $[\underline{D}]^{-1}$ to the expressions for $\underline{s}_0$" (5.72) and $\underline{s}$" (5.73) leads to the desired expression

$$\underline{s}_0 = s_{0_x}\underline{i} + s_{0_y}\underline{j} + s_{0_z}\underline{k} \qquad (5.79)$$

with

$$s_{0_x} = \cos\phi\cos\theta - \cos\chi\sin\phi\sin\theta$$

$$s_{0_y} = -\sin\phi\cos\theta - \cos\chi\cos\phi\sin\theta \qquad (5.80)$$

$$s_{0_z} = -\sin\chi\sin\theta$$

and

$$\underline{s} = s_x\underline{i} + s_y\underline{j} + s_z\underline{k} \qquad (5.81)$$

with

$$s_x = \cos\phi\cos\theta + \cos\chi\sin\phi\sin\theta$$

$$s_y = -\sin\phi\cos\theta + \cos\chi\cos\phi\sin\theta \qquad (5.82)$$

$$s_z = \sin\chi\sin\theta$$

Again, ϕ, χ and θ must be expressed in terms of the indices of the reflection and reciprocal cell constants. The value of θ is given by the standard expression for the Bragg angle for a triclinic cell:

$$\sin\theta = \tfrac{1}{2}[h_1^2 a_1^{*2} + h_2^2 a_2^{*2} + h_3^2 a_3^{*2}$$

$$+ 2h_1 h_2 a_1^* a_2^* \cos\gamma^*$$

$$+ 2h_2 h_3 a_2^* a_3^* \cos\alpha^*$$

$$+ 2h_3 h_1 a_3^* a_1^* \cos\beta^*]^{\frac{1}{2}} \tag{5.83}$$

The value of ϕ, Fig. 5.11, is given by

$$\phi = \tan^{-1} (\xi_x / \xi_y) \tag{5.84}$$

Expressions for ξ_x and ξ_y have been previously given in (5.64) through (5.67). The value for χ, Fig. 5.9 b, is given by

$$\chi = \tan^{-1} (\zeta/\xi) \tag{5.85}$$

where ζ is given by (5.69) and ξ by (5.63). When substituted in (5.80) and (5.82), expressions (5.83) through (5.85) give the desired relations for $\underset{\sim}{s}_0$ and $\underset{\sim}{s}$ in terms of the indices of the reflection and reciprocal cell constants.

5.9 Beam Path-lengths in Crystals

Expressions have now been obtained for unit vectors relative to the crystal shape, specifying the directions of the incident and diffracted beam in each of the principal diffraction geometries. These expressions were placed in the form

$$\underset{\sim}{s}_0 = s_{0_x} \underset{\sim}{i} + s_{0_y} \underset{\sim}{j} + s_{0_z} \underset{\sim}{k}$$

$$\underset{\sim}{s} = s_x \underset{\sim}{i} + s_y \underset{\sim}{j} + s_z \underset{\sim}{k}$$

Figure 5.11

Section through an upper level of a reciprocal lattice being investigated with the Eulerian cradle geometry.
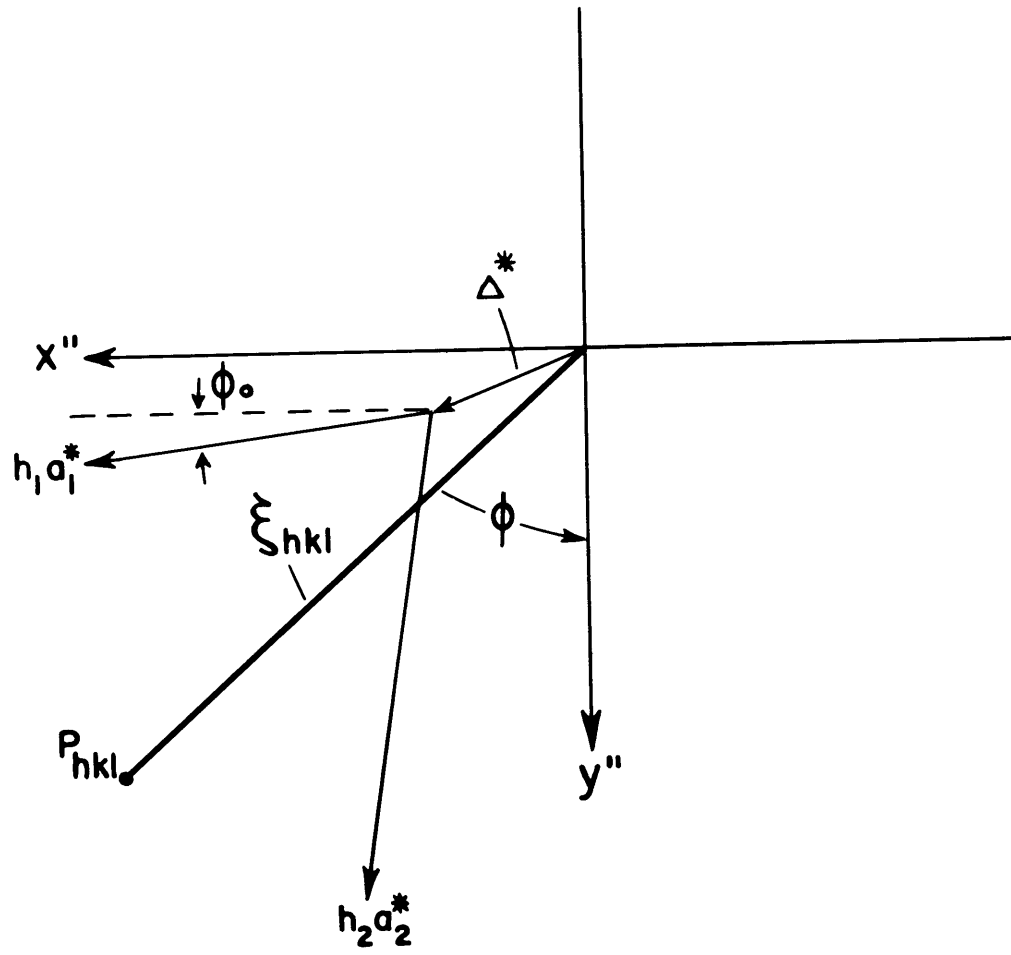
Now, for each grid point $\underline{x}_l \ \underline{y}_m \ \underline{z}_n$ we seek a scalar multiple of each of these vectors such that the resulting vector extends from a grid point to the surface of the crystal. This scalar multiple will be found for each bounding function. The several solutions must then be tested, as described in Section 5.10, to determine which scalar represents the desired path length.

Let $\underline{t}_0$ be defined as the scalar multiple of the incident-beam vector and $\underline{t}$ as the scalar multiple of the diffracted-beam vector. In order that the values of $\underline{t}_0$ and $\underline{t}$ be positive, $\underline{t}_0$ is defined as a negative multiple of $\underset{\sim}{s}_0$ and $\underline{t}$ as a positive multiple of $\underset{\sim}{s}$. The desired vectors $\underline{t}_0 \underset{\sim}{s}_0$ and $\underline{t} \underset{\sim}{s}$ have the grid point $\underline{x}_l \ \underline{y}_m \ \underline{z}_n$ as origin, and coordinates $\underline{x}_{0_i} \ \underline{y}_{0_i} \ \underline{z}_{0_i}$ and $\underline{x}_{-i} \ \underline{y}_{-i} \ \underline{z}_{-i}$ respectively, as the terminal points. These points are given by:

$$x_{0_i} = x_l - t_{0_i} s_{0_x}$$

$$y_{0_i} = y_m - t_{0_i} s_{0_y} \qquad\qquad (5.86)$$

$$z_{0_i} = z_n - t_{0_i} s_{0_z}$$

and

$$x_i = x_l + t_i s_x$$

$$y_i = y_m + t_i s_y \qquad\qquad (5.87)$$

$$z_i = z_n + t_i s_z$$

The points $\underline{x}_{0_i} \ \underline{y}_{0_i} \ \underline{z}_{0_i}$ and $\underline{x}_{-i} \ \underline{y}_{-i} \ \underline{z}_{-i}$ satisfy the equation $\underline{f}_{-i}(xyz) \equiv F_{-i}$, where the general form of f_{-i} is given in equation (5.12) and (5.13). Substitution of the expressions (5.86) in (5.12) gives:

$$A_i(x_l - t_{0_i} s_{0_x})^2 + B_i(y_m - t_{0_i} s_{0_y})^2 + C_i(z_n - t_{0_i} s_{0_z})^2$$

$$+ D_i(x_l - t_{0_i} s_{0_x})(y_m - t_{0_i} s_{0_y})$$

$$+ E_i (y_m - t_{0_i} s_{0_y})(z_n - t_{0_i} s_{0_z})$$

$$+ G_i (z_n - t_{0_i} s_{0_z})(x_l - t_{0_i} s_{0_x})$$

$$+ H_i (x_l - t_{0_i} s_{0_x}) + I_i (y_m - t_{0_i} s_{0_y})$$

$$+ J_i (z_n - t_{0_i} s_{0_z}) = F_i \qquad (5.88)$$

Expansion of this expression and collection of terms in $t_{0_i}^2$ and t_{0_i} leads to a quadratic equation in t_{0_i} :

$$[A_i s_{0_x}^2 + B_i s_{0_y}^2 + C_i s_{0_z}^2 + D_i s_{0_x} s_{0_y} + E_i s_{0_y} s_{0_z}$$

$$+ G_i s_{0_x} s_{0_z}] t_{0_i}^2 - [2A_i s_{0_x} x_l + 2B_i s_{0_y} y_m$$

$$+ 2C_i s_{0_z} z_n + D_i (s_{0_y} x_l + s_{0_x} y_m)$$

$$+ E_i (s_{0_y} z_n + s_{0_z} y_m) + G_i (s_{0_z} x_l + s_{0_x} z_n)] t_{0_i}$$

$$+ [A_i x_l^2 + B_i y_m^2 + C_i z_n^2 + D_i x_l y_m + E_i y_m z_n$$

$$+ G_i x_l z_n + H_i x_l + I_i y_m + J_i z_n] = F_i \qquad (5.89)$$

The solutions for t_{0_i} are therefore given by

$$t_{0_i} = \frac{-q \pm \sqrt{q^2 - 4p(r - F_i)}}{2p} \qquad (5.90)$$

with

$$p = [A_i s_{0_x}^2 + B_i s_{0_y}^2 + C_i s_{0_z}^2 + D_i s_{0_x} s_{0_y}$$

$$+ E_i s_{0_y} s_{0_z} + G_i s_{0_x} s_{0_z}] \qquad (5.91\underline{a})$$

$$q = -[\, 2A_i \, s_{0_x} \, x_l + 2B_i \, s_{0_y} \, y_m + 2C_i \, s_{0_z} \, z_n$$

$$+ D_i(s_{0_y} \, x_l + s_{0_x} \, y_m) + E_i(s_{0_y} \, z_n + s_{0_z} \, y_m)$$

$$+ G_i(s_{0_z} \, x_l + s_{0_x} \, z_n)\,] \qquad\qquad (5.91\underline{b})$$

$$r = [\, A_i \, x_l^2 + B_i \, y_m^2 + C_i \, z_n^2 + D_i \, x_l \, y_m + E_i \, y_m \, z_n$$

$$+ G_i \, x_l \, z_n + H_i \, x_l + I_i \, y_m + J_i \, z_n\,] \qquad (5.91\underline{c})$$

It is readily seen that substitution of (5.87) in (5.12) leads to solutions for t_{-i} of the form (5.90) except that (a) in (5.91 $\underline{a}$) and (5.91 $\underline{b}$) the appropriate expressions s_{-x}, s_{-y}, and s_{-z} replace s_{-0_x}, s_{-0_y}, and s_{-0_z} respectively, and (b) the sign of $\underline{q}$, equation (5.91 $\underline{b}$), is positive and not negative.

5.10 Interpretation of Beam-Path-Length Solutions.

5.10.1 Selection of Path-Length of Correct Sign. There are two ambiguities in the solutions for t_{-0} and t_{-}, (5.90). In general, there will be two solutions to (5.90), one positive and one negative, (except for the case of a plane, when coefficients A_{-i} through G_{-i} are zero, and (5.89) reduces to a linear equation.) The positive solution, t_{-}^+, is the one required. The negative solution represents the interaction of the beam with the opposite side of the function (see Fig. 5.14, below). The latter solution, t_{-}^-, is ordinarily discarded, unless the crystal has a centro-symmetric shape (Section 5.12).

A second type of ambiguity results from the fact that solution of (5.90) for each bounding function $f_{-i}(\underline{xyz})$ leads to a collection of path lengths t_{-i}^+. Of these, only one represents the true path distance to the surface of the crystal. The technique of selecting the proper path length differs slightly depending on whether the crystal has limited or unlimited bounding functions.

5.10.2 Unlimited Bounding Functions. The procedure for crystals displaying unlimited bounding functions is straightforward. Figure 5.12a presents a simple example in which three solutions t_1, t_2 and t_3 are obtained. The correct value, t_1, is merely the smallest value in the collection.

$$t = \text{Min.} \left\{ t_1, t_2, t_3 \ldots \right\} \tag{5.92}$$

5.10.3 Limited Bounding Functions. Figure 5.12b gives an example of the situations which will be encountered with crystals displaying limited bounding functions. In the example shown, six solutions are obtained. Some of these, t_1, t_2 and t_4, are real solutions corresponding to distances at which the beam leaves or re-enters the crystal. Other solutions, typified by t_3, represent intersection of the beam with a function lying within the volume of the crystal. These solutions have no meaning and should be discarded. Still other solutions, t_5 and t_6, correspond to intersections of the beam with functions which lie outside the crystal. These solutions also have no meaning and should also be discarded.

Solutions of these types may be distinguished by a special test. Let a small increment ϵ be added to t. The terminal point of $(t + \epsilon)$ is given by either (5.86) or (5.87) depending on whether a path length of the incident or diffracted beam is involved. Assuming, in this example, that a path length of the diffracted beam is concerned, (5.87) gives

$$x_i = x_1 + (t + \epsilon) s_x$$
$$y_i = y_m + (t + \epsilon) s_y \tag{5.93}$$
$$z_i = z_n + (t + \epsilon) s_z$$

Similarly, if an increment ϵ is subtracted from t, the terminal point of the vector becomes

$$x_i = x_1 + (t - \epsilon) s_x$$

Figure 5.12

Interpretation of the set of solutions for the path length from a grid point to the bounding functions of a crystal. (a) Unlimited bounding functions. (b) Limited bounding functions.

$$y_i = y_m + (t - \epsilon) s_y \tag{5.94}$$
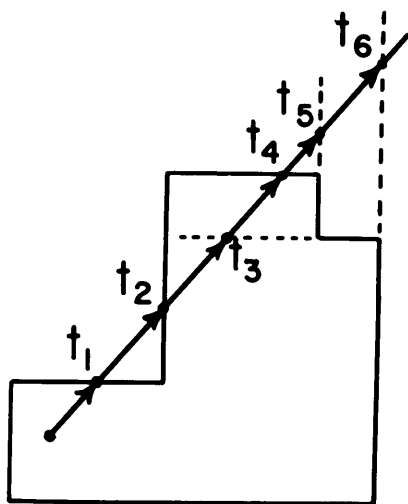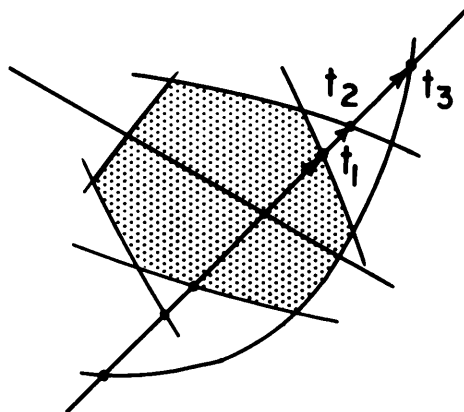
$$z_i = z_n + (t - \epsilon) s_z$$

Let the terminal points (5.93) and (5.94) now be tested according to (5.6) or the procedure of Section 5.6.3 to determine whether or not these points lie within the volume of the crystal. Let (+) represent the result that the new terminal point lies within the crystal and (-) the result that the point lies without the crystal. These tests, applied to the example in Fig. 5.12 b, give

	$t + \epsilon$	$t - \epsilon$	
t_6	(-)	(-)	
t_5	(-)	(-)	
t_4	(-)	(+)	
t_3	(+)	(+)	(5.95)
t_2	(+)	(-)	
t_1	(-)	(+)	

when the collection of t's are arranged in order of decreasing magnitude. Distances t_{-3}, which intersect a function lying within the crystal, give positive results for both tests. Distances of this sort may be discarded. Similarly, distances such as t_{-5} and t_{-6}, which intersect functions outside the volume of the crystal, give negative results for both tests and may be discarded. It should be noted that there is a much simpler test which may be applied to immediately discard solutions of the type t_{-5} and t_{-6}. By definition, equation (5.2), the crystal lies within a "box" with dimensions 2u, 2v, 2w. Therefore all real solutions for t must satisfy the relation

$$|t| \le 2(u^2 + v^2 + w^2)^{\frac{1}{2}} \tag{5.96}$$

Considerable computation time will be saved if this test is first applied to the set of values for t.

The desired values of $\underline{t}$ are those which yield results in (5.95) of the form "(+)(-)" or "(-)(+)"; a "(-)(+)" solution represents a beam leaving the crystal volume, and a "(+)(-)" solution represents a beam re-entering the crystal. The smallest $\underline{t}$ of the set must therefore be of the type (-)(+). Having ordered the set of solutions by magnitude, the desired path length is given by

$$t = t_{(-)(+)} - [t_{(+)(-)} - t_{(-)(+)}] - [t_{(+)(-)} - t_{(-)(+)}] \cdots$$

(5.97)

where the terms on the right of (5.97) are in order of increasing magnitude. For the example of Fig. 5.12 $\underline{b}$, the solution (5.97) takes the form

$$t = t_1 - [t_2 - t_4] .$$

(5.98)

5.11 Extension of the Method to Complex Special Cases.

The program may be extended with slight modifications to treat very complex special cases. Figure 5.13 presents two examples which represent problems which might actually be encountered. Figure 5.13 $\underline{a}$ represents a crystal with re-entrant angles and absorption coefficient μ_1 surrounded by mother liquid of absorption coefficient μ_2 which is in turn enclosed in a glass cylinder of absorption coefficient μ_3. To treat this problem, grid points are established within the crystal, and beam path-lengths computed as above. The functions representing the inner and outer walls of the cylinder are also included with the collection of bounding functions, so that the path lengths from each grid point to these walls are also determined. The path lengths in the crystal are again determined as above. Path lengths outside the crystal, however, are now retained and absorption coefficient μ_2 is applied to these distances. Letting t_{-C} and $t_{-C'}$ represent the distances to the inner and outer walls of the cylinder respectively, the desired value of $\mu\underline{t}$ for a particular ray

Figure 5.13

Examples of complex special cases which may be treated with a modified version of the general method.

(a) crystal with re-entrant angles enclosed with mother liquid in a glass capillary tube.

(b) small crystal partially obscured by glass fiber on which it is mounted.

(a)

(b)
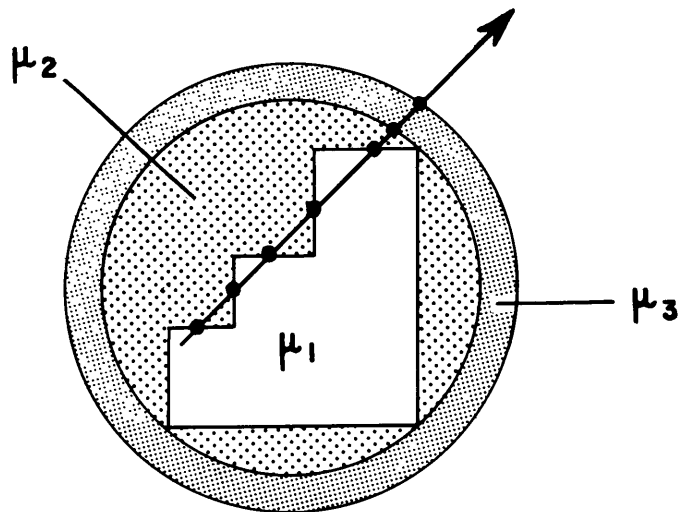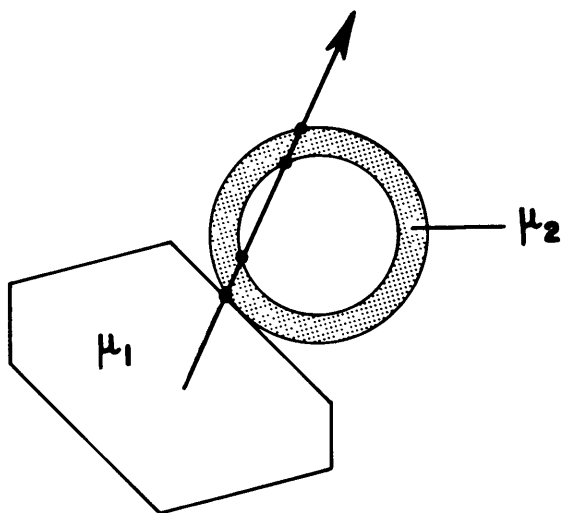
is given by

$$\mu t = \mu_1 \left\{ t_{(-)(+)} - [t_{(+)(-)} - t_{(-)(+)}] - [t_{(+)(-)} - t_{(-)(+)}] \cdots \right\}$$

$$+ \mu_2 \left\{ -[t_{(-)(+)} - t_{(+)(-)}] - [t_{(-)(+)} - t_{(+)(-)}] \cdots \right.$$

$$\cdots -[t_{(-)(+)} - t_{C'}] \right\} + \mu_3(t_{C'} - t_C) . \qquad (5.99)$$

Figure 5.13 b gives an example of a second sort of problem which might be encountered. Here, a small crystal of absorption coefficient μ_1 has been attached to a glass capillary tube in the normal fashion. The crystal is assumed to be so small, however, that the glass capillary causes appreciable absorption effects.[1] This problem may be treated in a fashion similar to that described above.

5.12 Evaluation of the Transmission Factor.

The path lengths of the beams to and from each grid point have now been evaluated for each grid point for a particular reflection hkl. The transmission factor T_{hkl} is given by

$$T_{hkl} = \frac{1}{V} \int e^{-(t+t_0)\mu} dV \qquad (5.100)$$

Replacement of (5.100) with a summation over all retained grid points gives:

$$T_{hkl} = \frac{1}{M(\frac{2u}{N})(\frac{2v}{N})(\frac{2w}{N})} \sum_{\substack{\text{retained} \\ \text{grid} \\ \text{points}}} e^{-(t^+ + t_0^+)\mu} (\frac{2u}{N})(\frac{2v}{N})(\frac{2w}{N})$$

$$= \frac{1}{M} \sum_{\substack{\text{retained} \\ \text{grid points}}} e^{-(t^+ + t_0^+)\mu} \qquad (5.101)$$

---

[1] This problem was actually encountered in the investigation of the crystal structure of turquoise (H. Cid-Dresdner, private communication). Equivalent intensities differed by as much as 50 %!

where $\underline{M}$ is the number of retained grid points.

If the crystal has a centrosymmetric shape, only half of the grid points established in Section 5.5 need be investigated. Figure 5.14 shows that, if the crystal is centrosymmetric, the negative path lengths obtained from (5.90) which would normally be discarded for a particular grid point x_{-l}, y_{-m}, z_{-n}, are equivalent to the desired positive path lengths for grid point $x_{-\bar{l}}$, $y_{-\bar{m}}$, $z_{-\bar{n}}$. Therefore, for a crystal of centrosymmetric shape,

$$T_{hkl} = \frac{1}{2M} \sum [e^{-(t^{+} + t_{0}^{-})\mu} + e^{-(|t^{-}| + |t_{0}^{-}|)\mu}] \tag{5.102}$$

where $\underline{M}$ now represents the number of grid points $\underline{treated}$, which is $\underline{half}$ the total number of grid points lying within the volume of the crystal.

5.13 Assessment of the Procedure.

As mentioned above, a program based on the completely general method presented in this section is still being developed. Special versions, however, for computing transmission factors for ellipsoidal crystals have been written. Using a $12 \times 12 \times 12$ grid-point system, reflections were processed on the IBM 7090 at a rate of about 36 per minute. This rate is rapid enough to make use of such a program practical.

The speed of the program, however, will be greatly reduced with use of a greater number of bounding functions or when the crystal shape has re-entrant angles. In the final version of the general program, this will be partially offset by employing Gaussian quadrature. (In this method, the grid points are established at unequal intervals and are assigned weights depending upon their locations. (Lowans et al., 1942). The effect of the procedure is to provide the accuracy of a larger number of equally-spaced grid points while actually using but a few intervals.)

Even with these provisions, however, computations for a crystal of complex shape, or computations for an involved problem similar to

Figure 5.14

Demonstration that the negative solution, t^-, for the path

length from a grid point $x_{\underline{-lmn}}$ represents the correct solution t^+ for

the centric equivalent of the grid point, $x_{\underline{-\bar{l}mn}}$, provided the crystal

has a centrosymmetric shape.
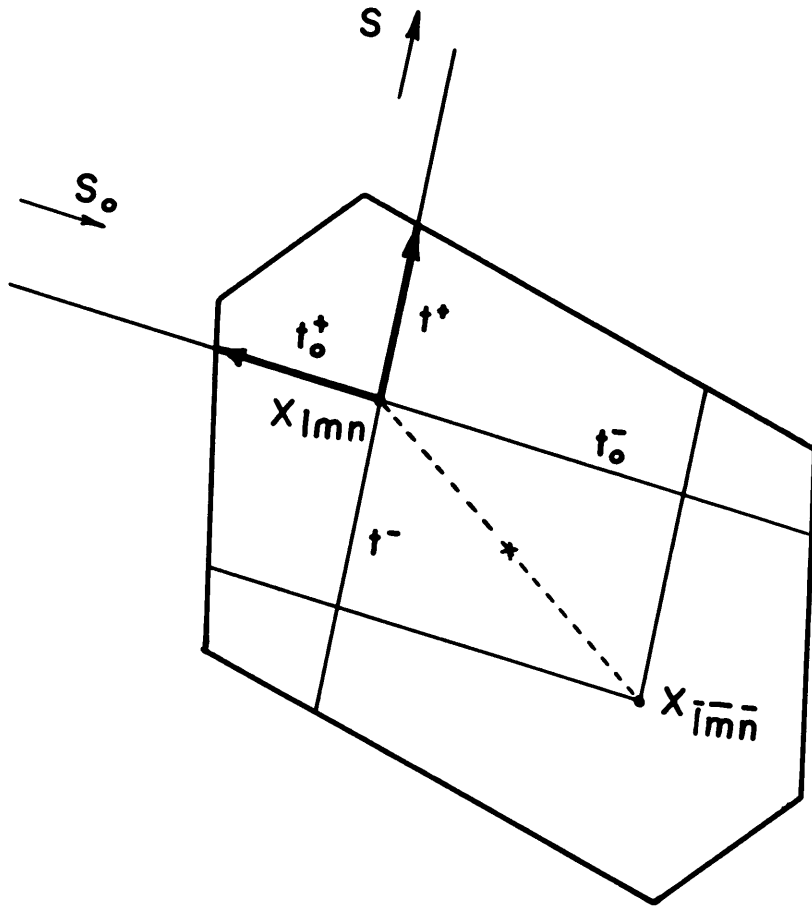
those outlined in Section 5.11 may be too costly in terms of computer time to be applied to a large number of intensities.

For complex cases, use of the program would probably be limited to two-dimensional data, crystals with small unit cells, or in situations where absorption effects are so serious that application of anything but an exact correction would leave the diffraction data worthless. Nevertheless, the significance of the present method is that problems of essentially any complexity can now be successfully handled if one is willing to expend the necessary computer time.

5.14 References.

Albrecht, Gustav (1939). The absorption factor in crystal spectroscopy. Rev.Sci.Instr. 10, 221-222.

Barbieri, F. and Durand, J. (1956). Method of cutting cylindrical crystal. Rev.Sci.Instr. 27, 871-872.

Bond, W.L. (1951). Making small spheres. Rev.Sci.Instr. 22, 344-345.

Bond, W.L. (1959 a). Sphere of radius R, bathed in a uniform incident x-ray beam. Section 5.3.6, International Tables for X-ray Crystallography, Vol. 2.(Kynoch Press, Birmingham) 299-300, 302-305.

Bond, W.L. (1959 b). Cylindrical crystal of radius R, bathed in a uniform beam of x-ray normal to its axis. Section 5.3.5, International Tables for X-ray Crystallography, Vol. 2, (Kynoch Press, Birmingham) 291-299.

Bradley, A.J. (1935). The absorption factor for the powder and rotating-crystal methods of x-ray analysis. Proc.Phys.Soc. (London) 47, 879-899.

Buerger, M.J. and Niizeki, N. (1958). The correction for absorption for rod-shaped single crystals. Am.Mineral. 43, 726-731.

Burnham, Charles W. (1961). The structures and crystal chemistry of the aluminum-silicate minerals, Ph.D. thesis, Department of Geology and Geophysics, M.I.T.

Busing, William R. and Levy, Henri A. (1957). High-speed computation of the absorption correction for single crystal diffraction measurements. Acta Cryst. 10, 180-182.

Claasen, A. (1930). The calculation of absorption in x-ray powder photographs and the scattering power of tungsten. Phil.Mag. 9, 57-65.

Evans, Howard T.,Jr. (1952). X-ray absorption corrections for single crystals. J.Appl.Phys. 23, 663-668.

Evans, H. T., Jr. and Ekstein, Miriam G. (1952). Tables of
absorption factors for spherical crystals. Acta Cryst. 5,
504-542.

Fitzwater, D. R. (1961). X-ray absorption factors for spherical
crystals. Acta Cryst. 14, 521-526.

Grdenic, D. (1952). A note on the calculation of the absorption
factor for single crystals of high absorbing power. Acta Cryst. 5,
283-284; 9, 540.

Hendershot, Otis P. (1937). Absorption factor for the rotating-
crystal method of x-ray crystal analysis. Rev. Sci. Instr. 8,
324-326.

Howells, R. Gwynne (1950). A graphical method of estimating
absorption factors for single crystals. Acta Cryst. 3, 366-369.

Joel, N., Vera, R. and Garaycochea, I. (1953). A method for the
estimation of transmission factors in crystals of uniform
cross section. Acta Cryst. 6, 465-468.

Kersten, H. and Lange, W. (1932). Method for preparing crystals
for rotation photographs. Rev. Sci. Instr. 3, 790-791.

Lowans, A. N., Davids, N. and Levenson, A. (1942). Table of the
zeros of the Legendre polynomials of order 1-16 and the
weight coefficients for Gauss' mechanical quadrature formula.
Bull. Am. Math. Soc. 48, 739-743.

Pepinsky, Ray (1953). Method for cutting and shaping fragile
crystals. Rev. Sci. Instr. 24, 403.

Prewitt, Charles T. (1960). The parameters T and ϕ for equi-
inclination, with application to the single-crystal counter
diffractometer. Zeit. Krist. 114, 355-360.

Rogers, D. and Moffett, R. H. (1956). A graphical aid for the
rapid evaluation of absorption corrections by Albrecht's
method. Acta Cryst. 9, 1037-1038.

Revell, K.S. and Small, R.W.H. (1958). The preparation of
    spherical single-crystals for x-ray diffraction work.
    J.Sci.Instr. 35, 73-74.

Taylor, A. and Sinclair, H. (1945). The influence of absorption
    on the shapes and positions of lines in Debye-Scherrer
    powder photographs. Proc.Phys.Soc. 57, 108-125.

Wasser, Jürg (1951). The Lorentz factor for the Buerger
    Precession Method. Rev.Sci.Instr. 22, 563-566.

APPENDIX I

The Reliability of Equi-inclination Counter Diffractometer Data

With the availability of high-speed computers with large storage capacities, it has become possible to refine even complex crystal structures to a high degree of precision. In this laboratory, values for the disagreement factor $R = \Sigma \mid \mid F_o \mid - \mid F_c \mid \mid / \Sigma \mid F_o \mid$ for silicate structures have ranged from of the order of 9% to as low as 6%. This level of agreement may perhaps begin to approach the overall reliability of the data. Very few studies of the consistency of diffractometer data have been made. Without this information, it is not possible to assess the significance of very low disagreement factors.

The majority of the crystal structures investigated in this laboratory have been of fairly low symmetry. Tetrahedrite (Section II), however, is isometric with space group I$\bar{4}$3m. The independent intensities are therefore contained within 1/48 of reciprocal space (i. e., $h \geq k \geq l$). Each general reflection occurs as 24 equivalent mates, excluding those related by Friedel's Law. The comparison of structure factors required by symmetry to be equivalent thus provided an unusual opportunity to examine normal diffractometer data for random and systematic error.

The diffracted intensities were obtained from a small spherical specimen of 0.114 mm radius ($\mu r = 7.39$ for CuKα), spherical to ±1.7%. Integrated intensities were determined by recording the total number of counts accumulated as the crystal was rotated through 6°ϕ. Background intensity was counted for 100 sec. on either side of the diffraction peak, and a suitable deduction of integrated background was made from the measured integrated intensity. A Kr-filled proportional counter was used to measure intensities. The associated electronics were standard Norelco equipment and included pulse-height analysis circuitry.

Using a representative sample of reflections, ranging from the weakest detectable to those with a maximum peak height of 2,000 counts

per second, three varieties of checks were performed:

(1) Measurement of certain reflections was repeated over a period of several weeks. The degree of agreement of these measurements is affected by reproducibility of the diffractometer settings (μ, γ, ϕ, Υ), counting statistics, and drift in the electronic equipment.

(2) Equivalent reflections of the form $\underline{hkl}$ and $\underline{khl}$ were examined within a given level, $\underline{l}$. The agreement between these data involves the above errors, plus variations in the absorption correction required, because of deviations of the crystal shape from a true sphere.

(3) Equivalent reflections of the form $\underline{hkl}$ and $\underline{hlk}$, $\underline{lhk}$ were compared between different levels. Agreement between these data is affected by all of the above errors, plus systematic errors from level to level, such as an error in the computed values of μ, incorrect correction for Lorentz and polarization factors, or differences in the manner in which the white radiation streak is crossed.

The results of the study are summarized in Table A1.1. While the deviation between equivalent structure factors in the same level exceeds the reproducibility of the data, it is of the same magnitude as the deviation between structure factors occurring on different levels. The main source of error in the set of tetrahedrite structure factors is therefore most likely uncertainty in the absorption correction. The 1.7% variation in radius causes an uncertainty of roughly 2% in the transmission factors, and consequently a 1% variation in the structure factors. This is about the right magnitude to account for the 1.7% increase in error over the reproducibility of the data. It would appear that with a more favorable value of $\underline{\mu r}$ and with an accurate correction for absorption, standard equi-inclination counter diffractometry is capable of providing a set of structure factors with an over-all precision of better than 2%.

Table A1.1

Comparison of Equivalent Isometric Structure Factors for Tetrahedrite

TEST	Range of intensities (Integrated peak intensity: integrated background intensity, counts $\times 10^4$)	Range of deviations from mean, F^2	RMS deviation from mean, F^2	Range of deviations from mean, F	RMS deviation from mean, F
Reproducibility (F_{hkl}, F_{hkl})	$8.29/2.13 - 1.17/6.32$	$0.016 - 6.1\%$	2.42%	$0.016 - 2.8\%$	1.15%
Symmetry within a given level (F_{hkl}, F_{khl})	$8.29/2.13 - 0.103/0.751$	$0.13 - 14.9\%$	5.82%	$0.066 - 7.5\%$	2.92%
Symmetry between levels $(F_{hkl}, F_{hlk}, F_{lhk})$	''	$0.86 - 11.9\%$	5.63%	$0.43 - 6.0\%$	2.82%

Appendix II

A High-Temperature Attachment for Use with the Precession Camera

A2.1 Introduction

Many minerals have phase-transitions at modest temperatures. Sulfide minerals, in particular, often display transitions in the range $100 - 300^o$ Centigrade. These temperatures can be obtained with relatively simple devices which do not require elaborate cooling precautions to protect the film and diffraction equipment. This appendix describes a heating attachment for the precession apparatus. The device is a modified version of a design originally mentioned by Morimoto and England (1960).

A2.2 Description of the Device

An exploded view of the device is given in Fig. A2.1, and a section through the device, when in position on the precession camera, in Fig. A2.2. The entire device is supported on the x-ray collimator, A. A mushroom-shaped cap, B, has two cylindrical portions which have been slotted to provide a firm friction fit to the other pieces of the assembly. The inner cylinder slides snugly over the x-ray collimator and is secured in proper position by means of a small ring, C, containing a recessed screw. A hollow brass cylinder, D, in which the heating element is mounted, slides snugly over the outer cylinder of the cap. This motion allows the entire heater to be retracted towards the x-ray tube as the crystal and goniometer head are mounted on the precession camera.[1] Once the crystal is in position, the heating unit, D, is slid

---

[1] In performing this operation it is recommended that the spindle of the precession camera be retracted as far as possible by means of its translating screw.

Figure A2.1

Exploded view of a high-temperature attachment for use with the precession camera. Lettered components are described in the text.
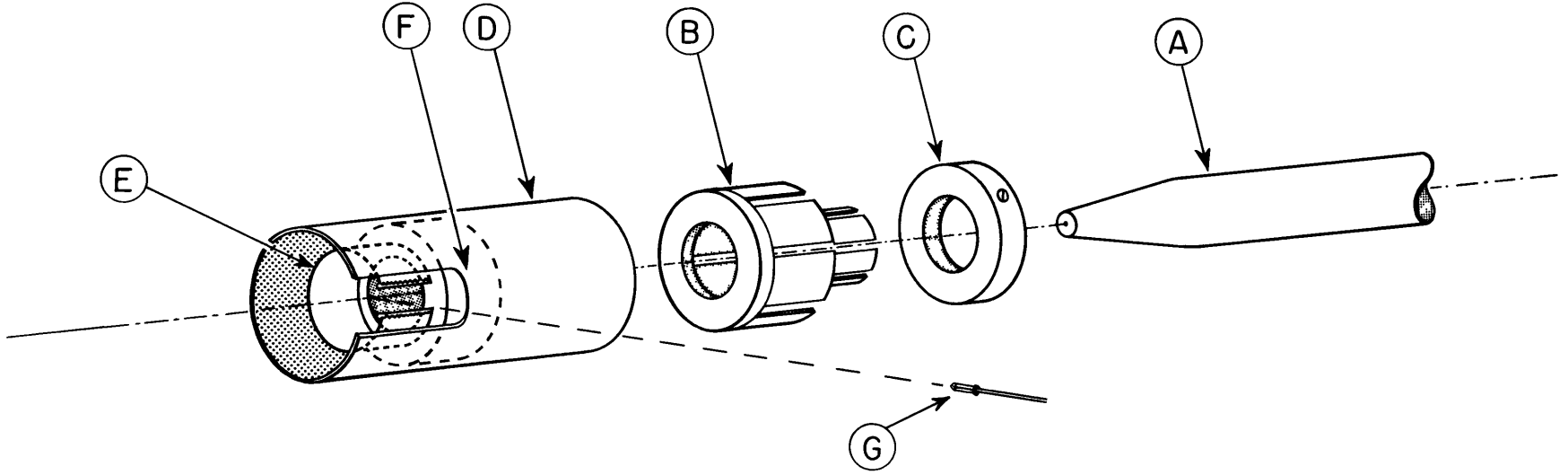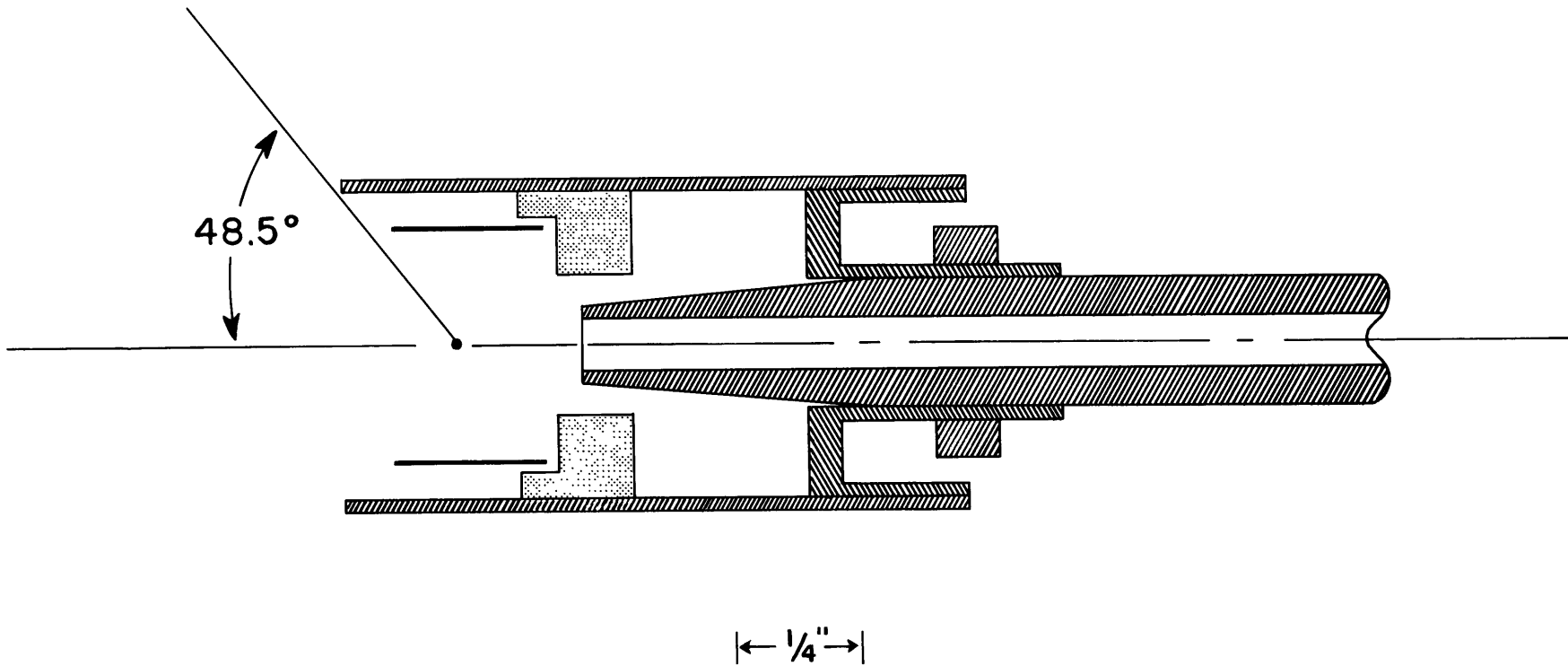
Figure A2.2

Scale drawing of section through the assembled high-temperature attachment.

48.5°

|←— ¼" —→|

forward to center the crystal with respect to the heating element. The heating element, E, consists of a 3/8 inch strip of 0.001 inch 90% Pt - 10% Rh foil. The foil is bent into a cylindrical shape concentric with the x-ray beam. The foil is supported at the ends by two copper wires which also serve as electrical contacts. These wires are crimped onto the foil and make only a mechanical connection. The wire supports, in turn, are supported by a pyrophyllite base, F, which is attached to the brass cylinder. The leads are extended through the pyrophyllite base and out the side of the brass cylinder where electrical connections are made. The pyrophyllite base serves as both a thermal and electrical insulator. A slight lip (see Fig. A2.2) extends around the lower portion of the cylindrical heating element to aid in supporting the foil and in preserving its cylindrical shape as it expands at elevated temperatures. The brass cylinder is extended beyond the top of the heating foil to serve as a heat shield. The geometry is such as to permit passage of a cone of diffracted radiation of half-angle 48.5° without interference.

The fiber supporting the crystal, G, is admitted through a slot in the side of the brass cylinder, D, and passes between the two wires supporting the heating foil to intersect the x-ray beam. Normal centering of the crystal by sighting through the x-ray collimator may be performed with the heating attachment in place. Figure A2.2 shows that contact between the heating assembly and the x-ray collimator is limited to the very thin top of the mushroom cap, B. This prevents heating of the x-ray collimator when the heater is in operation.

Regulation of the heater is very simple. The output leads of the secondary winding of a standard variac are connected to the primary winding of a 6.3 volt, 20 ampere transformer. The secondary winding of this transformer is connected directly to the heating unit leads.

A2.3 Calibration of the Unit

A small copper-constantan thermocouple was mounted in a short length of double-bore Alundum thermocouple tubing. This tubing was mounted in a goniometer head, and the thermocouple placed in the position of the crystal. The temperature detected by the thermocouple was calibrated against the setting of the variac. The calibration curve is given in Fig. A2.3 The procedure was performed on two occasions, and the results were consistent to within $\pm 5^\circ$C. This level of repro-ducibility was considered satisfactory for the present work, in which it was necessary merely to maintain the crystal above a given transforma-tion temperature while the diffraction record was being obtained. The calibration is considered sufficiently reproducible to be employed for a similar purpose by future users of the device. If the device is to be used in an application in which it is necessary to know the precise temperature of the crystal (e.g. determination of a transition temperature) it may be desirable to mount the crystal on a thermocouple, as described below.

It should be noted that calibration of the device was carried out only to 200°C. This was the maximum temperature required for the work contained in this thesis. At this temperature the variac is at only 25% of its maximum setting. The device is therefore capable of attaining much higher temperatures (at least 450°C) than those which have been reported here. It remains to be seen, however, what the life of the heating element will be, and how much heat will be conducted to the x-ray collimator at these temperatures.

A2.4 Mounting of the Crystal

Two problems are encountered in mounting the crystal when the device is used. First, an adhesive which will withstand the elevated temperatures must be found to secure the crystal to a supporting fiber. Second, the supporting fiber passes in close proximity to the copper

Figure A2.3

Calibration curve for the high-temperature attachment. Plot of temperature at crystal location as a function of voltage applied to primary winding of step-down transformer.
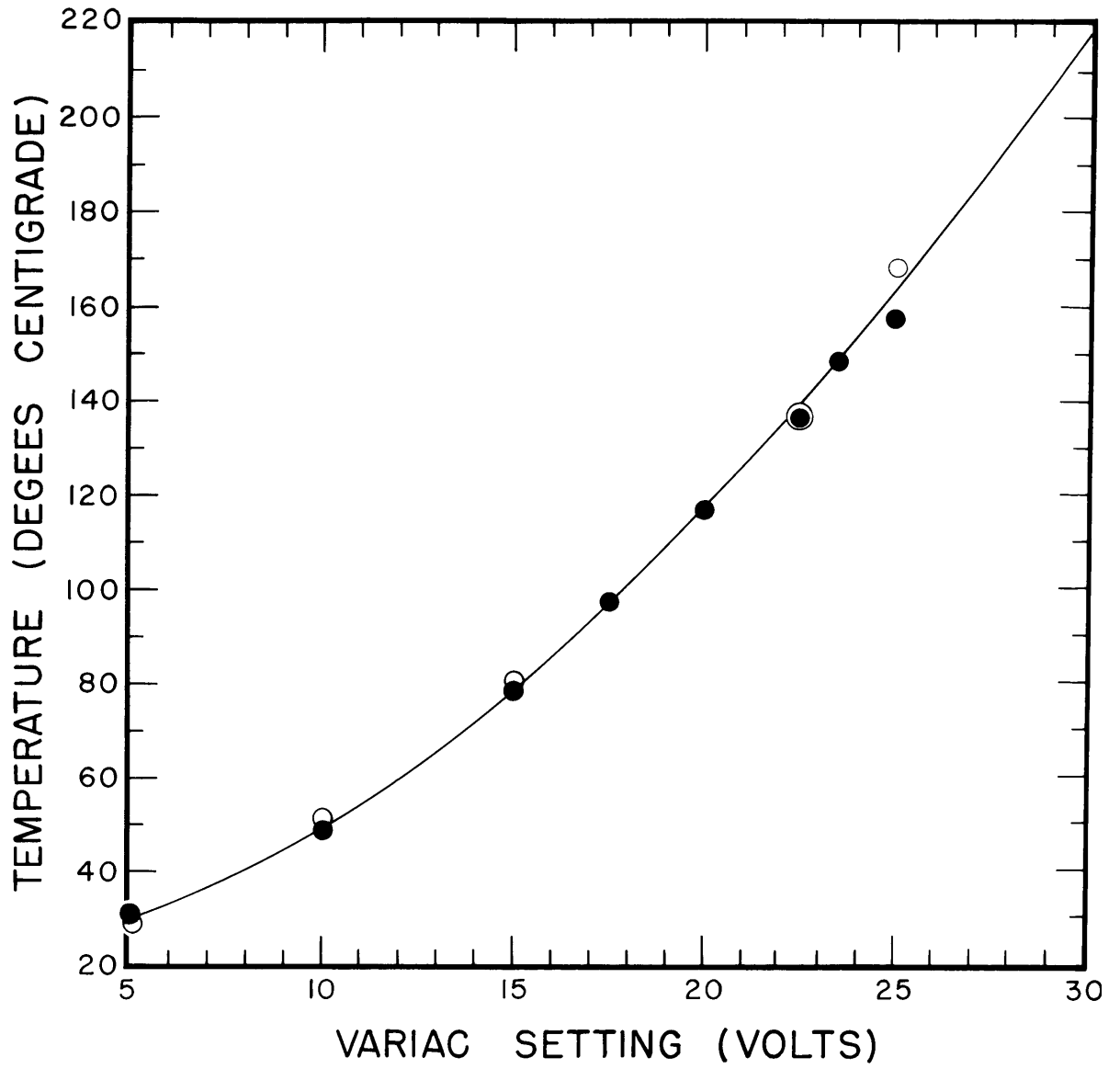
leads supporting the heating element. This portion of the fiber will experience a higher temperature than the crystal itself, since it is closer to the foil than is the crystal. This problem is made worse by the fact that the mechanical connection of the wires to the foil has relatively high resistance and thus becomes considerably hotter than the foil itself. The glass used to prepare the fibers on which crystals are usually mounted may be expected to soften at about 700 - 800° C. It was felt that a thin fiber would begin to creep and sag at a much lower temperature.
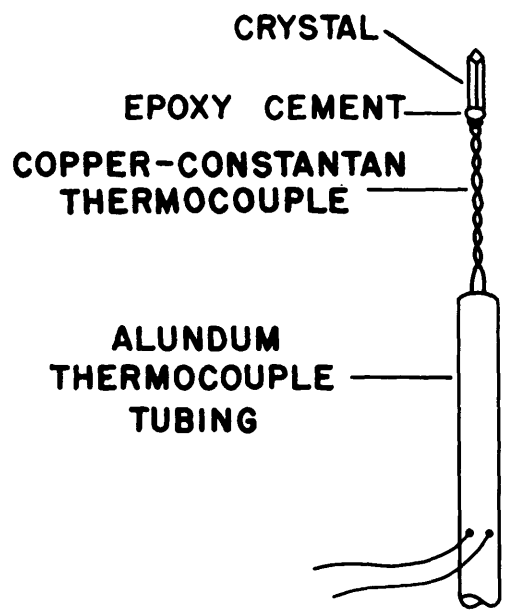
Two types of mounts which were found useful are illustrated in Fig. A2.4 <u>a</u> and <u>b</u>. In the first type, a copper-constantan thermocouple was mounted in double-bore Alundum thermocouple tubing. The crystal was attached directly to the end of the thermocouple. The thermocouple wires were led out through a nick filed in the side of the Alundum tubing, thus leaving the end of the tubing free for mounting in a goniometer head. This type of mount has the advantage of permitting continuous determination of the temperature of the crystal. Unfortunately, it is troublesome to use: The two wires in the thermocouple expand differentially as the temperature is increased. Final orientation of the crystal must therefore be performed after the crystal is at temperature. This is undesirable if the crystal has any tendency to deteriorate upon prolonged heating.

A more satisfactory, though less elegant, mount is shown in Fig. A2.4 <u>b</u>. In this arrangement a straight copper wire was soldered to the usual brass pin, and then extended to a length sufficient to almost bring it into the x-ray beam. A very short length of glass fiber was then attached to the end of the wire, and the crystal, in turn, was attached to the end of the glass fiber. The glass fiber is just long enough to prevent the copper wire from entering the x-ray beam.

The problem of a suitable adhesive was not completely solved. The organic adhesives normally used in mounting crystals are, of course, unsuitable, since they will deteriorate at about 100° C. Epoxy resin was found to be suitable for use with high-chalcocite, since only the modest

Figure A2.4

High-temperature crystal mounts. (A) Thermocouple mount
which affords the advantage of permitting continuous determination of
the temperature of the crystal. (B) Copper-wire mount which retains
crystal orientation more satisfactorily as temperature is increased.

CRYSTAL

EPOXY CEMENT

COPPER-CONSTANTAN
THERMOCOUPLE

ALUNDUM
THERMOCOUPLE
TUBING

CRYSTAL

GLASS FIBER

EPOXY CEMENT

COPPER WIRE

SOLDER

BRASS PIN

(A)
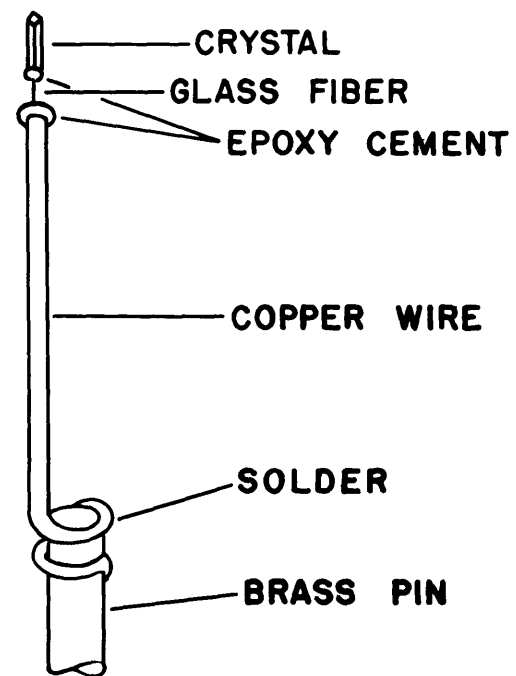
(B)

temperature of 125°C was required. At 200°C epoxy resin begins to deteriorate by carbonizing, and the crystal eventually drops off. Okazaki (1961) has used potter's clay as an adhesive. This material is quite sticky. The bond should actually grow stronger with time and temperature, since the clay will tend to shrink and sinter.

It should be noted that introduction of a thermocouple or poly-crystalline adhesive into the x-ray beam does not cause excessive background problems. Any scattered radiation reaching the film must pass through the layer-line screen, and thus travels essentially along the Laue cone. During the precession cycle, this radiation is uniformly distributed over the film. In the worst possible situation, a powder line might fortuitously occur at the same angle as the Laue cone. This may be checked by means of a cone-axis photograph. The problem is easily remedied by slightly shifting the setting of the precession angle $\bar{\mu}$, and thus changing the angle of the Laue cone. A copper-constantan thermo-couple placed in the x-ray beam was found to cause no appreciable increase of background in $MoK\alpha$ precession photographs of over 60 hours duration.

A2.5 References

Morimoto, N. and England, J.L. (1960), High-temperature Buerger
    precession camera. Carnegie Institution of Washington Year Book
    59, 175.

Okazaki, Atsushi (1961), The superstructures of iron selenide Fe_7Se_8.
    J.Phys.Soc.Japan, 16 1162-1170.

Appendix III

Preparation and Processing of Integrated Precession Films

A3.1 Introduction

When film is exposed to x-radiation, grains of silver bromide contained in the emulsion are influenced in such a way that a suitable developing process reduces them to particles of metallic silver. Up to a certain saturation point, the number of silver grains will be proportional to the number of x-ray quanta incident on the film. If the number of silver grains contained in a layer of thickness dt in the developed emulsion is N per unit area, then the intensity of a beam of light transmitted through the film will be attenuated by an amount dL given by

$$dL = -kNLdt \qquad (A3.1)$$

where k is a constant. Integration of (A3.1) over the thickness of the film leads to

$$T = \frac{L}{L_0} = e^{-kNt} \qquad (A3.2)$$

where T is defined as the transmission factor of the film. From (A3.2),

$$\ln \frac{L_0}{L} = kNt \qquad (A3.3)$$

The quantity kNt is defined as the optical density, D, of the film. Since N is proportional to the intensity of the incident beam of x-radiation, it follows that D is also proportional to the x-ray intensity.

Unfortunately, when a developed x-ray film is scanned with a beam of light, the intensity of the transmitted beam is proportional to T and not D. Determination of an integrated intensity would therefore first require conversion of T to D, ie

$$D = \ln\left(\frac{1}{T}\right) \qquad (A3.4)$$

Provision for accomplishing this conversion may be incorporated into the apparatus used to measure the film. An alternative procedure was proposed by Dawton (1938). The method consists of preparing a second print from the original x-ray film. Since the second print is a "negative" of the original x-ray film, it consists of transparent spots on an opaque background. When the characteristics of the two films are carefully matched through a specific exposure and developing procedure, a second film can be obtained such that the transmission through each transparent spot is proportional to the total energy in the x-ray beam which caused the original reflection.

A suitable development procedure which matched Kodak No-Screen x-ray film and Kodak Commercial Ortho film was developed in this laboratory in about 1941 (Buerger, 1960). This method fell into disuse as counter diffractometers were developed. Eastman-Kodak subsequently discontinued production of No-Screen x-ray film in favor of more sensitive x-ray films.

Still another solution to the problem is to employ a "plateau" technique. In these methods the normal Weissenberg or precession camera is modified so that the film may be given a slight displacement following each cycle of the apparatus. If the film is displaced in a cyclic fashion over a distance which exceeds the size of the spot, each portion of the normal diffraction spot has an opportunity to contribute to the central portion of the "smeared" spot. This central portion will therefore display a "plateau". The density of the plateau is proportional to the integrated x-ray intensity, since it represents the sum of all intensities in the distribution of intensities contained in the diffracted x-ray beam. In this fashion, densities are added by mechanical means as the film is exposed. This reduces determination of an integrated intensity to the problem of converting one transmission factor to a density.

As mentioned in Sections III and IV, film methods afforded several advantages in the collection of intensities for chalcocite and pyrrhotite. Since conditions for the use of the Dawton method would have had to have been carefully re-established for present-day x-ray films, it was decided to obtain integrated films.

A version of the Wiebenga (1947) integrating Weissenberg apparatus has been commercially available for some time. (Nonius, Delft, Holland). The principle has been extended to the precession method (Nordman et al., 1955). About the time intensity data was to be collected for chalcocite and pyrrhotite, the Charles Supper Company had produced a prototype of an integrating precession instrument. The author was kindly permitted to use this device in collecting intensities in order to test its capabilities. A modified and improved version of the apparatus is now being produced, and the laboratory has acquired one of these instruments. This appendix describes the procedures used by the writer to expose, develop and measure integrated precession films. A detailed discussion is given in hopes that these experiences may be of use to future users of the apparatus.

A3.2 Use of the Integrating Precession Apparatus

The Charles Supper Company integrating precession camera is identical to the standard precession instrument except for the provisions for cyclic translation of the film. In the integrating device, the film cassette is attached to a plate which is free to move in a vertical direction with respect to a second plate. This second plate, in turn, is free to translate in a horizontal direction relative to the body of the instrument. The two plates are translated by means of two cams, one of which is contained in a slot in each plate. The plate is spring-loaded so that one edge of the slot always remains in contact with the surface of the slot. The cam translating the first plate (the vertical motion of the film cassette) is coupled to that of the second plate by means of shafts bearing a 24-tooth ratchet and a 2-tooth gear, respectively. The shaft to which

the cam moving the second plate (the horizontal motion of the film cassette)
is attached is extended towards the yoke on which the setting of $\bar{\mu}$ is accomplished.
A small pin on this yoke engages a 24-tooth ratchet on the end of this
shaft so that the shaft is turned $\frac{1}{24}$ of a revolution for each precession
cycle.

By means of this arrangement the horizontal motion of the film
is advanced $\frac{1}{12}$ of its maximum displacement for each cycle of the
precession motion. When the horizontal motion has completed 12 steps,
the cam accomplishing the vertical translation advances $\frac{1}{12}$ of its
maximum displacement. The cams have been carefully machined so
that the displacements occur in equal increments. The maximum
displacement of the film is 1 mm. The integrated spot on the film
therefore consists of a collection of 12 × 12 spots. Since the normal
precession instrument precesses at a rate of one revolution per minute,
144 minutes are required for one cycle of the integrating motion. This
is the minimum exposure time which may be employed in preparing the
films. This property of the instrument should be taken into account
when the voltage and amperate settings for the experiments are decided
upon. These settings must be such that density of the strongest reflections
does not exceed the linareity range of the film in the time required to
complete one cycle. An alternative solution would be introduction of
attenuating foils, or change of the voltage or current when recording
intense reflections. This procedure, however, would require intro-
duction of an appropriate scale factor and would consequently appear
to be less desirable.

The cams which accomplish the translation of the film are
symmetric. That is, the shape of the cams is such that the film returns
to its original position by retracing its path, rather than by the abrupt
jump which might be accomplished if the cams were given a discontinuity.
Therefore care must be taken that the integrating cycle is started with
both the horizontal and vertical translations at either their maximum or
minimum displacements. If a 144-minute exposure were started, for

example, with the film at the mid-point of its cycle, a 6 × 12 array of reflections would be obtained in which each portion of the spot had been exposed twice instead of once.

As mentioned above, the spots on the film are displaced over an area of 1 × 1 mm. The "plateau" in the integrated spot will extend between the edges of the normal spot when it is in the two extreme positions. The size of the plateau is therefore $(1 - x)$ mm, where x is the diameter of the spot. It is therefore advantageous to minimize the size of normal spot by reducing the divergence of the incident x-ray beam, ie by employing a fine collimator. The size of the spot produced by a crystal of dimensions suitable for measurement of intensities will probably be of the order of .5 mm, so that a plateau may normally be expected over a region of at least .5 mm. Note that it is therefore desirable to employ a crystal of approximately spherical dimensions; prismatic crystals are not suitable. An example of a film prepared with the instrument is given in Fig. A3.1. This may be compared with a normal precession photograph taken with the same crystal which has been previously given in Fig. 4.1 Densitometer scans of typical spots are described below.

Precession photographs taken with MoKα radiation are capable of providing an amount of intensity data equivalent to that contained within the CuKα sphere. The low wavelength of MoKα radiation, however, causes the characteristic radiation to occur within the spectral distribution of the continuous radiation. This causes precession films to display a familiar white radiation streak passing radially through each diffraction spot. It is difficult to correct for this effect. Introduction of a Zr filter does not solve the problem, since this procedure merely eliminates the short wavelength end of the streak. The result is therefore a diffraction peak which is still superimposed on an appreciable white radiation streak, and the intensity of this streak may now be estimated on but one side of the spot. Unfiltered radiation was therefore used in this work. The plateau intensity was corrected

Figure A3. 1

Example of a photograph prepared with the integrating precession apparatus. (Pyrrhotite, pseudo-hexagonal b axis, zero level. Unfiltered Mo radiation, 39 kV, 15 ma, 20.25 hour exposure.) A normal precession photograph taken with the same crystal has been previously given in Fig. 4.1.
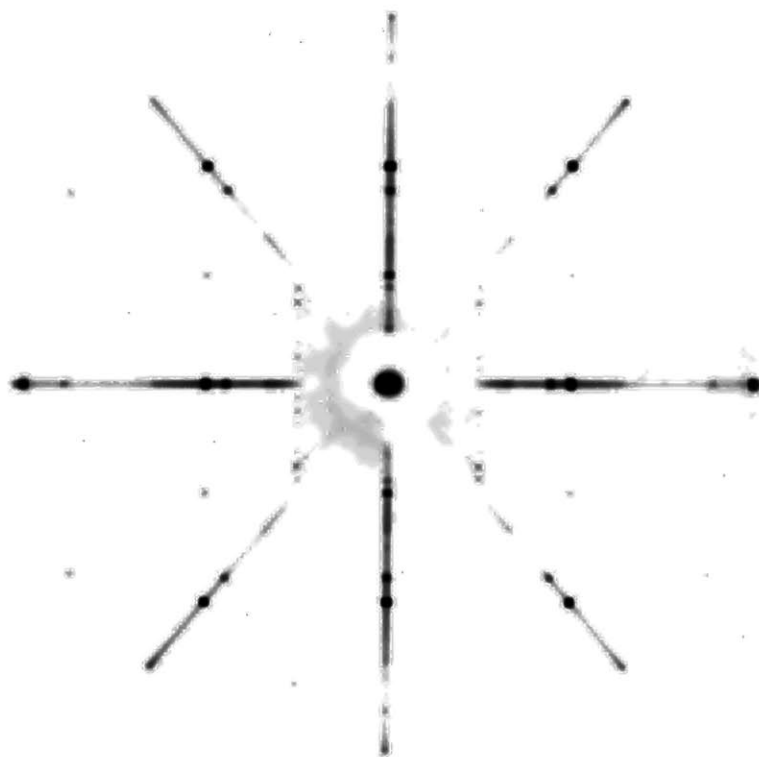
for background, but no correction was made for the white radiation streak. This approach is valid if the white radiation intensity at the peak is proportional to $\underline{F}^2$. This will be the case if the short-wave limit of the continuous radiation is adjusted so that there is no $\lambda/2$ component in the continuous spectrum. If this precaution is observed, the only problem caused by the white radiation is that the high wavelength end of a streak through a strong reflection may interfere with a neighboring spot. This was a rare occurrance in the films measured. Use of unfiltered radiation provides a further advantage. The exposure times required for the preparation of integrated films is greater than that required for a comparable normal precession film. This occurs because the spots on the integrated films are distributed over an area. As a result, the exposure time must be increased by a factor of at least five to obtain an intensity comparable to that obtained on a normal precession film. Exposure times of up to 90 hours were required to record the weaker intensities of pyrrhotite and chalcocite with unfiltered radiation. These exposure times would have been prohibitively long with filtered radiation. Finally, it should be noted that the appearance of the white radiation streak on a normal precession film suggests that the problem is worse than it actually is. The intensity of a spot on a quantitative film should be limited to an optical density of about 1.5. At this level of exposure the spot has a "dark grey" appearance. The "black" spots which display the familiar white radiation streaks in precession photographs have optical densities in excess of 3, and would nor ordinarily be encountered in quantitative work. In the present measurements the white radiation streak was usually indistinguishable from variations in the overall background when the peak intensity of the spot was below an optical density of about 0.5.

A3.3 Development of the Films

It is desirable that all films be developed simultaneously in order that they receive similar treatment. No scale factor is there-

fore required (other than the exposure time, which is well known) to put all the intensities on the same scale. The ordinary one gallon developing tank is not large enough to permit simultaneous development of more than four or five films. It was found that an inexpensive polyethylene wastebasket was available with just the correct dimensions to accommodate a row of 5-inch films. Three of these containers were obtained to serve as developing, rinse and fixing tanks respectively. Three gallons of solution in these tanks provides sufficient volume for developing the films. The tanks are about 3 feet deep. They could, perhaps, be cut down to more convenient dimensions, but it was felt that the additional depth provided rigidity and also protected against splashing of the developing solutions while processing the films.

The problem of a suitable film holder was not completely solved. A proper holder should ideally allow the developing solution to circulate freely between the films. This requires that the holder support the films at a minimum number of points. A special holder was constructed of polyvinyl chloride (which does not react with the developer) which is capable of holding 25 films of the standard 5-inch width. The films are supported in the center of three edges by means of slots in three thin slats which are permanently attached to rigid end pieces parallel to the film. The first and last slots of the series are ordinarily loaded with unexposed film so that the outermost exposed films will not receive special treatment. After the films have been loaded in the rack, they are secured in position by a fourth slotted slat which slides in a channel to secure the upper and fourth edge of the films. The channel is provided with stops so that the removable slat may be brought to rest at the height required to secure either a 5 × 7 inch Weissenberg film or a 5 × 5 inch precession film. The film holder fits neatly into the polyethelene tank with just enough play to permit agitation while the films are developed. A problem which was encountered with a film holder of this design is that the slots which hold the films must be extremely shallow. The reason for this is that the diffraction record of a precession pattern

extends almost to the edge of the film. The films must therefore fit extremely snugly into the slots if they are not to come loose as they buckle during agitation in the developing process. As a result it is difficult to load films into the slots and the process is quite time consuming. In the present work nearly thirty minutes were required for the task, and slight fogging of the films by the dark-room safe-lights was noted. The film used to record the intensities was Ilford "Industrial G" x-ray film. Films were developed for 12 minutes at 59.5° F. It was found convenient to use a wetting agent (Kodak Photo-flo) in the final rinse to insure uniform drying and to prevent spotting. As mentioned in the next section, it was found that, provided a high-quality densitometer is used, the limit placed on the accuracy of the intensity measurements was imposed by the graininess of the films and not the amount of background on the films. It is therefore recommended that future users of the method employ a slow-speed, fine-grained x-ray film and fully investigate the effect of developing procedure on the graininess of the films before obtaining their quantitative films.

A3.4 Measurement of Intensities

A3.4.1 Description of Densitometer. The instrument used to determine the density of the integrated spots was a Joyce-Loebl Company microdensitometer. The densitometer is located in the laboratory of Professor Alexander Rich, of the M.I.T. Department of Biology. The writer is deeply indebted to Professor Rich for his permission to use the device for an extended period of time.

The densitometer is of the double-beam type. A regulated source of light is used to provide a beam of light which is then split into two portions. One beam is directed through a specimen stage upon which the film to be measured has been placed. Both the length and breadth of this scanning beam may be adjusted. It may be varied from a long rectangular line, a few microns in width, to a square or pinpoint of light. The second portion of the beam passes through a

density-wedge standard. Its deflection on a piece of graph paper is thus proportional to the density encountered at the specimen stage.

A spot on the film is scanned by means of a variable-speed motor which drives a stage holding a sheet of ordinary paper. The recording stage is coupled to the specimen stage by means of a lever arm. This arm may be adjusted to provide ratios of specimen-travel to chart-travel which range from 1:2 to 40:1. When the recording stage has attained its maximum length of travel, the driving motor is automatically switched off. The operator then uncouples the motor and the specimen stage, and repositions the recording stage. A new sheet of graph paper is placed on the recording stage, and scanning of the film may be continued from the last position of the previous record. Alternatively, the recording stage may be returned to its original position without uncoupling the specimen stage. The film is then also returned to its original position, and the same region of the film may be rescanned.

A3.4.2 Intensity Scale and Linearity Range of the Film. The plateau density representing the integrated intensity was recorded directly by the densitometer. It therefore was not necessary to determine the characteristics of the film in detail, or to use an intensity scale as an aid in estimating intensities. It is still necessary, however, to prepare an intensity scale in order to determine the linearity range of the film.

The characteristics of a film may differ for x-radiation of different wave lengths. In Weissenberg photography an actual reflection of the crystal may be used to prepare an intensity scale. This procedure is difficult in precession photography since the apparatus has no provision for oscillating the crystal. Furthermore, if a crystal of dimensions suitable for collection of intensities is used, the density of a spot produced by a reflection displays a sharp peak. It is more desirable to have an intensity scale which is composed of broad spots which display regions of uniform intensity.

The direct beam was used to prepare the intensity scale in the present work. A lead plate which contained a 3/16 inch diameter hold was secured in position over the hole in the 10 mm diameter layer line screen. This protected the film from radiation scattered by air. After a spot had been exposed, the film cassette was partially withdrawn in its dove-tail track to expose a fresh area of film for the next spot. To approximate $MoK\alpha$ radiation, the x-ray tube was set at a voltage for which the short-wave limit was $0.65\,\mathring{A}$. The normal Zr filter and .007 inches of Fe foil were inserted in the path of the x-ray beam. This limited the transmitted radiation to a narrow "window" of radiation between .65 and about .75 $\mathring{A}$.[1] About 90% of the transmitted intensity occurs in the range .69 to .71 $\mathring{A}$ because of the discontinuity at the Zr absorption edge.

The intensity scale was prepared for times given by

$$a\,2^{\frac{n}{2}} \qquad n = 0, 1, 2, \ldots$$

where $\underline{a}$ is the time required to expose a barely detectable spot (Buerger, 1960). The thickness of the Fe foil was chosen so that $\underline{a}$ was 15 seconds. Figure A3.2 presents plots of optical density as determined with the densitometer, as a function of exposure time. The same intensity scale was measured twice, using both 0 to $1\underline{D}$ and 0 to $2\underline{D}$ wedges as standards. Figure A3.2 shows that deviations from linearity occur for both scans, but that the deviation occurs at a certain fraction of full-scale deflection of the wedge and not at the same optical density on the film. These deviations therefore represent non-linearity of the densitometer and not non-linearity of the film. (The manufacturer

---

[1] The transmission factor for this combination of filters was roughly 5×10^{-11} at .65 $\mathring{A}$, increased to 4×10^{-10} at the Zr absorption edge, and had sharply decreased to 5×10^{-17} at .75 $\mathring{A}$. The transmission factor continues to drop rapidly to as low as 10^{-102} until the Fe absorption edge is reached, when it increases to only 10^{-19}. The transmitted intensity therefore closely approximates the $MoK\alpha$ wavelength.

Figure A3. 2

Determination of the linearity range of the film. Plot of
relative optical density as a function of exposure time for MoKα
radiation. Scans of the intensity scale were made with both 0 to 1 and
0 to 2 optical-density wedges. The deviations from linearity occur at
same percentage of full-scale deflection for both wedges. The deviation
therefore represents non-linearity of the densitometer and not non-
linearity of the film.
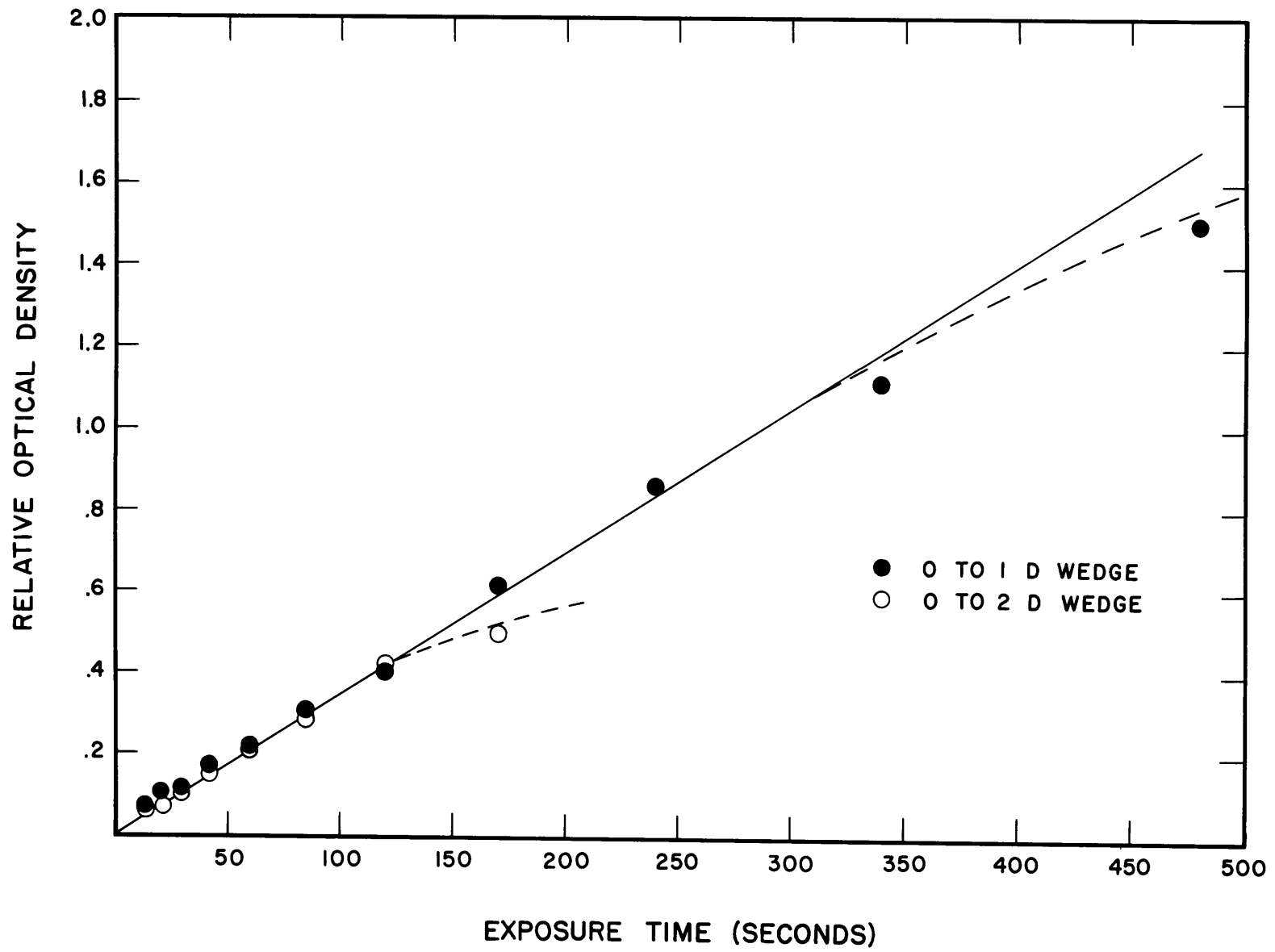
cautions against this effect in the instruction booklet for the instrument.)
The film therefore was linear to densities in excess of at least 1.7.
The maximum densities encountered in the measurements were of the
order of 1.8.

Nearly three months were required to record the three-dimen-
sional data for pyrrhotite. Since all films were to be developed
simultaneously, the exposed films were stored until the exposures
were completed. It was felt that the quality of the latent image in the
emulsion might deteriorate in this length of time. To check this effect,
intensity scales were prepared both before and after the films were
prepared. No difference in the properties of these two films was noted.

A3.4.3 Use of the densitometer. When the plateau is scanned
with the light beam, reduction of the apparent width of the plateau occurs.
The scanning beam has a finite width, and a plateau therefore appears
on the record only when the entire beam has entered the plateau region
of the spot. The apparent width of the plateau is therefore $(1 - x - y)$ mm,
where y is the width of the scanning beam and, as above, x is the
diameter of a normal diffraction spot from the crystal. It would there-
fore be desirable to use a scanning beam of the smallest possible size
in order to maximize the extent of the plateau in the record.

This was attempted, but it was found that the densitometer
produced a jagged record. The variations in the trace amounted to a
change of density of as much as .1. This caused the values of the
weak intensities (of the order of .1 to .2 D) to be extremely inaccurate.
This variation did not represent noise in the instrument. The densito-
meter scans are scrupulously reproducible. In fact, if the film and
recording stage are repositional, as described above, the recording
pen retraces the original line so precisely that the second trace cannot
be distinguished. (This represents a reproducibility of better than
1 part in 200 for full scale deflection.)

The cause of these abrupt jumps was found to be the graininess of the x-ray films. Since the "grey" background on the film actually consists of opaque grains in a transparent emulsion, the density recorded by the densitometer experiences an abrupt jump as a particularly large silver grain either enters or leaves the field of the scanning beam.

The problem was minimized by increasing the size of the scanning beam until the plateau was just resolvable. This technique has the disadvantage of producing a plateau of limited extent on the record, but in return, has the effect of smoothing out the traces. Samples of scans obtained for pyrrhotite intensities with the densito-meter are presented in Fig. A3.3. Figure A3.3a presents a selected trace which was obtained from a strong reflection with a 0 to 2 D wedge. Figure A3.3b presents a scan of a pyrrhotite superstructure reflection "triplet" obtained with a 0 to 1 D wedge. The latter scans are fairly typical of traces obtained for reflections of medium intensity.

Data was collected by scanning along a reciprocal lattice row. As a sheet of graph paper was filled with the record, the film was repositioned so that roughly 5 cm of overlap occurred with the succeeding trace. The strict reproducibility of the trace made it possible to piece together all the charts which had been obtained, and thus obtain a long, continuous record of an entire reciprocal lattice row. This procedure made it possible to make an accurate estimation of the variation in background intensity.

Several variations in the scanning procedure were tried. Some films were measured by scanning radially outwards through each individual spot so as to measure just the intensity above the white radiation streak. This technique proved to be unsatisfactory because of the extreme tediousness of repositioning the film for each reflection. Also, since the integrated reflections are square, the scanning beam entered a reflection from a different angle for each reflection and thus distorted the profile of the reflection. Another procedure which was
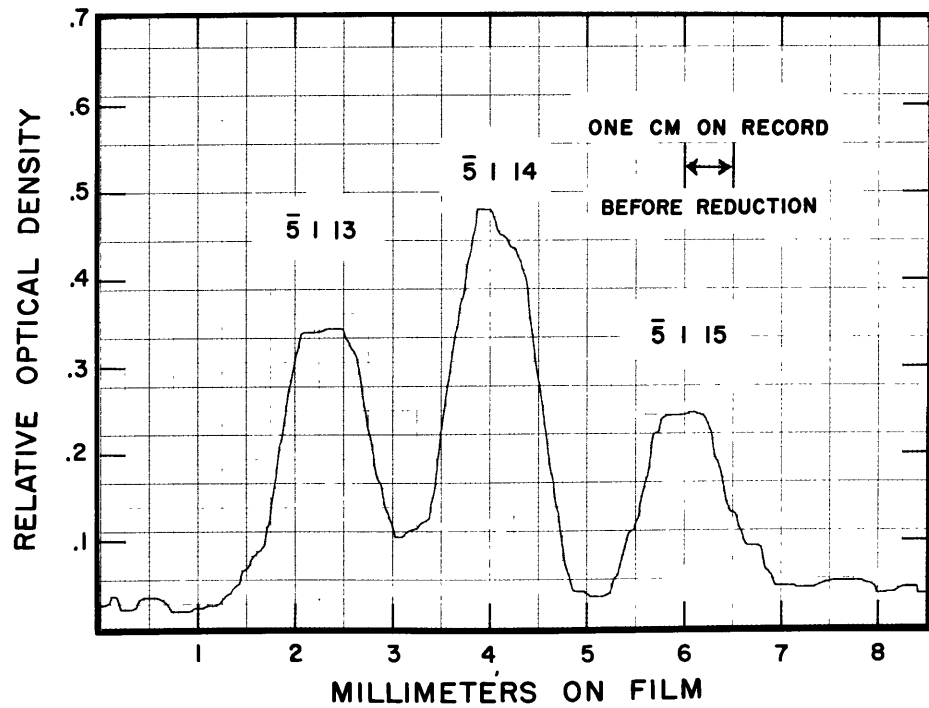
Figure A3. 3

Examples of scans of integrated precession spots produced by a recording microdensitometer:

(a) selected scan prepared with a 0-to-2$\underline{D}$ density wedge as standard.

(b) Scan prepared with a 0-to-1$\underline{D}$ density wedge as standard. These peaks are fairly typical of those obtained for peaks of medium intensity.
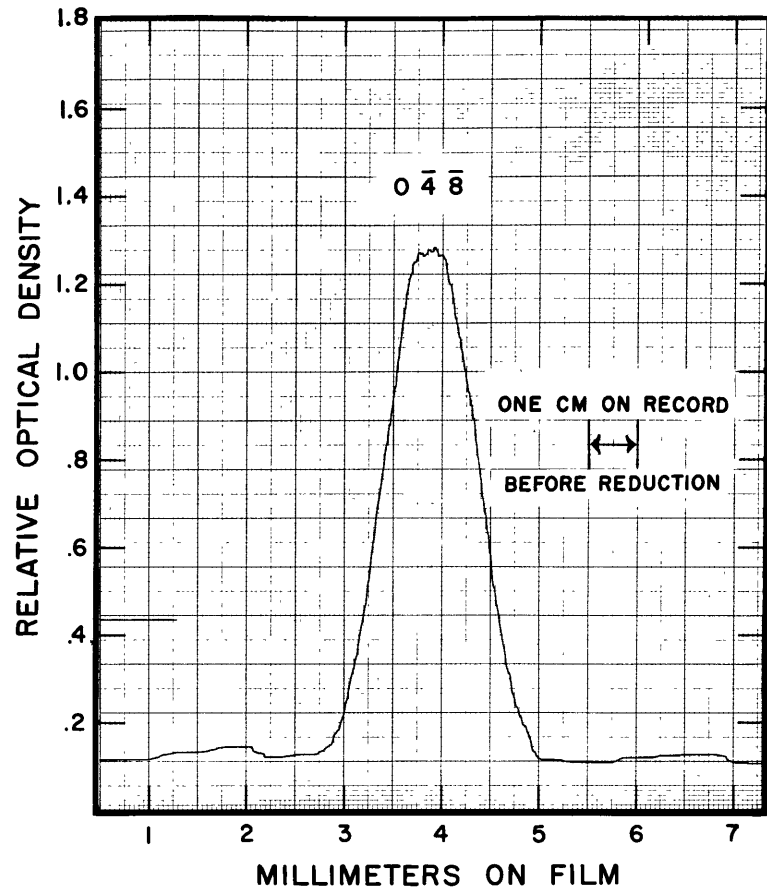
(a)

(b)

investigated was repetition of each reciprocal lattice row scan on either side of the spot. As has been noted above, this procedure proved unnecessary since the intensity of the streak was often less than the variation in background. Furthermore, such a correction is unnecessary if it is assumed that the white radiation intensity at the integrated spot is also proportional to $\underline{F}^2$.

The writer feels that if a high-quality densitometer is used to measure the films, and if steps are taken to reduce the graininess of the films, the integrating precession technique is capable of yielding a set of structure factors with a precision close to that provided by a counter diffractometer. Equivalent structure factors obtained for chalcocite had a rms deviation from the mean of about 10% even though the films obtained from this crystal displayed high background, graininess, and very weak reflections.

A3.5 References

Buerger, Martin J. (1960). Crystal-structure Analysis. (John Wiley and Sons, New York) 95-102.

Dawton, Ralph H.V.M., (1938). The integration of large numbers of x-ray crystal reflections. Proc.Phys.Soc. (London) 50, 919-925.

Nordman, Christer E.; Patterson, A.L.; Weldon, Alice S., and Supper, Charles E. (1955). Integrating mechanism for the Buerger precession camera. Rev.Sci.Instr. 26, 690-692.

Wiebenga, E.H. (1947). An integrating Weissenberg-apparatus for x-ray analysis. Rec.trav.chim. 66, 746-748.

Biography

Bernhardt John Wuensch was born on September 17, 1933, in Paterson, New Jersey. He is the elder of two sons of Bernhardt and Ruth Hannah Wuensch. He was educated in public schools in Paterson, and was graduated from Eastside High School in January, 1951.

He was admitted to the Department of Physics at M. I. T. in September, 1951, and was awarded the Degree of Bachelor of Science in physics in June, 1955. His thesis was concerned with the attenuation of ultrasound in fluids. Finding that he was more intrigued by piezo-electricity and the properties of crystals than by acoustics, he joined the M. I. T. Laboratory for Insulation Research. In completing the requirements for the Degree of Master of Science in the Department of Physics, he worked on the application of zone-melting techniques to the purification and growth of large single-crystals of alkali halides. He was awarded the S. M. Degree by M. I. T. in September, 1957.

Continuing interest in the structure and properties of crystals led him to decide upon x-ray crystal-structure determination as his main field of interest. In September, 1958, he was permitted to pursue an interdepartmental course of study leading to the Degree of Doctor of Philosophy in Crystallography. While a graduate student, he has held the position of Teaching Assistant in the Department of Physics, and positions of Teaching Assistant and Research Assistant in the Department of Geology and Geophysics. He was married in June, 1960, to the former Mary Jane Harriman of Swampscott, Massachusetts.

He is a member of the American Crystallographic Association, the Mineralogical Society of America, the American Ceramic Society, and the Society of the Sigma Xi.

Publications:

Ultrasonic absorption in castor oil: Deviations from Classical Behavior. (1956) J.Acoust.Soc.Am.28, 311-312. (with T.F.Hueter and M.S.Cohen).

The crystallography of mcgovernite, a complex arsenosilicate. (1960) Am.Mineral.45, 937-945.

Diffusion in refractory oxides. (1960) In Reactivity of Solids, Proc.4th Int.Symp.on the Reactivity of Solids, J.H.deBoer, ed. (Elsevier Pub.Co., Amsterdam) 57-64. (with T.Vasilos)

The Wells effect in precession photography. (1961) Z. Krist.115, 359-372.

Review of "An introduction to the methods of optical crystallography" by F.Donald Bloss.(1961) Z.Krist.116, 485-486.

Diffusion of transition metal ions in single-crystal MgO. (1962) J.Chem.Phys.36, 2917-2922. (with T.Vasilos)

Review of "Ore microscopy" by Eugene M. Cameron. (1962). Z.Krist.117, 476-478.

Grain-boundary diffusion in MgO. (1963) J.Am.Ceram.Soc. (in press). (with T.Vasilos)